CRANFIELD UNIVERSITY

Jan Theuer

Finite element modelling of the interaction between flexible tines and soil for mechanical weeding

School of Applied Sciences

MSc by Research

Academic Year: 2010 - 2011

Supervisor: Dr. Abdul Mounem Mouazen

October 2011

CRANFIELD UNIVERSITY

School of Applied Sciences

MSc by Research

Academic Year 2010 - 2011

Jan Theuer

Finite element modelling of the interaction between flexible tines and soil for mechanical weeding

Supervisor: Dr. Abdul Mounem Mouazen

October 2011

This thesis is submitted in partial fulfilment of the requirements for the degree of MSc by Research

ABSTRACT

This research was carried out to obtained information about the interaction of flexible tines and soil for mechanical weeding. Due to the fact that chemical weeding has negative effects on the environment, mechanical weeding is widely used today as an alternative and more sustainable solution. The complexity of soil-tine interaction, with flexible tines, makes it highly difficult to extract the needed information from experimental works only. Therefore, the aim of this study was to obtain extended knowledge about optimal design parameters (rake angle and tine geometry) and operational conditions (working depth and bulk density) for optimal soil disturbance and least energy consumption, by the use of numerical finite element computer simulation. To achieve this, a test bench was designed to study different tine designs and operational conditions of selected flexible tines, provided by Einböck, an Austrian manufacturer of weed harrows. The results of the test bench were mainly used to validate the established finite element model, which enabled a more informed analysis of the weeding process. Furthermore, soil parameters and soil-metal properties needed as input for the FEM simulation were determined by standard laboratory tests. Results showed that FEM is an acceptable and cost effective alternative to experiments. The simulation errors for draught and upward tine tip movement were generally smaller than 15 % and 10 %, respectively. Software associated limitations were experienced to model the entire working process satisfactorily, for instance no crack propagation in soils could be taken into account so far. Nevertheless, it was possible to simulate the first soil-tine interaction contact. This was sufficient to optimise tine design parameters and operational conditions, which was considered a cost effective method for the manufacturing of prototypes. From the FEM simulation and soil bin test, it could be concluded that a stiffer tine with a higher torsion spring constant and a small rake angle should be used when less variation in working depth and more aggressive weeding is required. Otherwise, trailing positions should be used, if a shallow working depth is desired, to achieve higher soil disturbance in the surface for smaller draught requirements.

ACKNOWLEDGEMENTS

I want to thank my supervisor Dr. Abdul Mounem Mouazen, who supported me with expertise and guidance during the entire project.

My further thanks to the Austrian company Einböck for their willingness to participate in the project and to promptly provide the needed flexible tines.

TABLE OF CONTENTS

LIST OF FIGURES

LIST OF TABLES

LIST OF SYMBOLS AND ABBREVIATIONS

List of Symbols

Latin letters

Symbol	Unit	Explanation
a	kPa	Adhesion
c	kPa	Cohesion (Mohr-Coulomb)
d	kPa	Cohesion (Drucker-Prager)
E	kPa	Young's modulus
G	$N\ m^{-2}$	Shear modulus
K	-	Flow stress ratio
M	kPa	Centre of Mohr's circle
m_{dry}	Kg	Dry soil mass
m_{wet}	Kg	Wet soil mass
p	kPa	Mean effective stress
p_a	kPa	Volumetric plastic strain (Drucker-Prager)
p_b	kPa	Hydrostatic compression yield stress (Drucker-Prager)
q	kPa	Mises equivalent stress
R	-	Material parameter (Drucker-Prager)
R_c	kPa	Radius of Mohr's circle
r	kPa	Third stress invariant
S	kPa	Stress deviator
t	kPa	Shear stress (Drucker-Prager)
V_b	m^3	Volume of the wet soil sample

Greek letters

Symbol	Unit	Explanation
α	-	Constant for transition yield surface (Drucker-Prager)
β	°	Internal friction angle (Drucker-Prager)
γ	-	Shear strain
δx	mm	Displacement in x-direction
ε	-	Strain
ε_{el}	%	Elastic strain
ε_{pl}	%	Plastic strain
ε_{1A}	mm	Initial length of soil specimen (before test)
ε_{2A}	mm	Length of soil specimen (after test)
ε_{1R}	mm	Initial thickness of soil specimen (before test)
ε_{2R}	mm	Thickness of soil specimen (after test)
ε_{vol}^{in}	%	Start point of volumetric plastic strain (Hydrostatic compression test)
ε_{vol}^{pl}	%	Volumetric plastic strain (Hydrostatic compression test)
θ_m	%	Gravimetric moisture content
ν	-	Poisson's ratio
ρ_s	kg m^{-3}	Soil bulk density
ρ_w	kg m^{-3}	Density of water
σ_1	kPa	Principle stress
σ_3	kPa	Confining pressure
σ_d	kPa	Deviatoric stress

σ_n	kPa	Normal stress
τ	kPa	Shear stress
ϕ	°	Internal friction angle (Mohr-Coulomb)
φ	°	External friction angle

List of Abbreviations

Abbreviation	Explanation
ATT	Attempt
BD	Bulk density
CFD	Computational fluid dynamics
DEM	Discrete/ distinct element method
DOF	Degrees of freedom
EORT	Extended octagonal ring transducer
FEM	Finite element method
FFT	Fast Fourier transform
IGES	Initial Graphics Exchange Specification
LED	Light-emitting diode
PC	Personal computer
RA	Rake angle
RAM	Random-access memory
SI-Units	International system of units
SSH	Secure Shell network protocol
USA	United States of America
USB	Universal Serial Bus
WD	Working depth

1 Introduction

Agriculture plays an important part in human life, because it produces a basic human need, food. Due to the growing world population, climate change and limited land resources, agriculture is confronted with big challenges and has to become more and more efficient at all production stages, including soil preparation, sowing, plant protection and harvesting. Plant protection is important to achieve a high yield and, although the development has made a big stride forward in the last century, weeds are still a problem. Weed control has played an important role in agriculture for many years, because one of the best conditions for proper plant growth will be with less competition from weeds. An efficient weed control system will lead to eliminating lack of water and nutrients consumed by weeds competing with the crop plants, which results in higher crop growth and yields. Weed control in agriculture is divided into chemical and mechanical. In the former process agrochemicals are applied in different forms to eliminate weeds, which is a non-environmental friendly method. The mechanical weed control is an environmental friendly method, where there is no need to use agrochemicals, and weeds are eliminated by mechanical actions. In this case the application of mechanical action into the cropping system, including weeds might result in undesirable damages to the crop, if inappropriate tools or mechanical weeding strategies are used. To be efficient and precise in the implementation of mechanical weed control, in depth understanding of the entire process is needed. Experimental work might be limited in providing the needed input for better understanding of the process, as field conditions are extremely variable, with the inherent variability in soil conditions. Theoretical simulations using numerical methods have proved efficient in limiting those external factors, leading to useful conclusions on the simulation of soil-tool interaction for general tillage processes. Therefore, this work was carried out to expand the use of numerical methods to gain in depth knowledge about soil-flexible tine interaction for sustainable mechanical weeding.

1.1 Literature review

Plant growth can be disturbed by weeds, since weeds abstract soil nutrients [13], which reduce crop growth. Today there are two methods to eliminate weeds. These are chemical and mechanical weeding methods. Van der Weide et al. [57] wrote that the former method uses herbicides, which are very inappropriate for the environment, in regard to ground and surface water contamination, human health risks, effects on flora and fauna etc. Browman [8] reported that mechanical weeding is less dangerous for the environment and cheaper to use. Furthermore, it has greater management flexibility, less trouble with herbicide-resistant weeds, reduced off-farm environmental impact and presents an alternative solution to deal with rising environmental standards. There are different mechanical weeders available on the market, namely, standard rotary hoe, flex tine weeder, finger weeder, torsion weeder and disk cultivators. All these weeders have the same task, which is to kill weeds mechanically in a most efficient manner possible without damaging the crop. Koch [32] found that covering weeds with soil is more effective than uprooting. Rasmussen [46] reported that high selectivity is an important precondition of successful weed control, which is defined as the ratio between weed control and crop soil cover. Many investigations were carried out to obtain more information about the behaviour of different weeders and how they are influenced by different working conditions, e.g. different types of harrow, harrowing time in regard to the weed growing stage, driving speed and number of harrowings and their influence on the crop [46] and [48]. Experimental works were carried out by Mouazen et al. [38] and Duerinckx's et al. [12] to understand the mechanical aspects of a flexible spring harrowing, indicated as the tine tip movement behaviour and reaction force between soil and tine tip, with regard to different soil types, tine settings and operational conditions. These studies aimed at obtaining information for the better understanding of the weeding process that can be used for the optimisation of the harrow design and the operational conditions including the optimal (appropriate) soil conditions, working depth and speed of the tine for efficient and good weeding results. However, these studies were conducted under laboratory conditions without

considering the presence of crop plants or weeds. Furthermore, this was pure experimental work without any in depth measurement of soil physical and mechanical properties to enable understanding of this complex process. Sogaard [52] reported a positive effect of a stable working depth on soil-covering during mechanical weeding with a finger weeder, under different soil structures, with a controlled tine rake angle. This behaviour is mainly influenced by the geometry of the tine, where a pre-evaluation technique during the design stage of the tine could help to reduce the use of expensive controller equipment. Under experimental working conditions, Kurstjens and Perdok [33] described the influence of different soil moisture contents, working speeds and working depths on covering selectivity. They reported that a change in working depth covered both tested plant species (ryegrass and garden cress), but did not significantly increase the burial depth. Furthermore they found that, with increasing working depth, the surface level upheaval increased, which is an important contribution for covering capacity. A higher working speed covered more plants but had no further effect on the burial depth, and an increasing working speed had hardly influences on surface level upward movement. The moisture content had also a significant influence on the weeding output, so that a drier soil showed better covering results than the wetter soil due to its fragile structure, although the soil upheaval was lower in dry soil where the leaf tip lowering increased. The outcome was that there were three aspects identified as the factors which had most influence on covering ability. Firstly, to push the subsurface parts of the plant forward and downward into the soil failure. Secondly, is the effect of placing soil on the top of the leaves and thirdly the ability to move the upper soil layer sufficiently in the plant direction. These final results are mainly influenced by the tine geometry, the soil structure and the interaction between both. This raises the problem of the experimental work, as it is difficult to change many parameters in an experiment, in a cost effective way. Furthermore, there is no satisfactorily method to study the soil-tine interaction, due to high working speed and complex contact conditions, which would help to understand the selectivity and covering process of plants. The same problem applies concerning the internal soil material behaviour. All these previous

investigations acknowledge the importance and complexity of the mechanical weeding process and the limitation of pure experimental work in providing sufficient results for a better understand of this problem, where the interaction between soil, plant and roots is very complicated. Therefore, it is necessary to use a method, which allows simulating this interaction particularly between soil and weeders, as this is essential for the design of an efficient harrowing system that eliminates weeds while preserving the crop plant intact. Furthermore, the efficiency in eliminating weeds has to be accompanied by least energy consumption achieved with the smallest draught, as draught is directly related to the fuel consumption of any soil engaged vehicle.

Literature shows that empirical, analytical or numerical methods are used to study the interaction between soil and tines during tillage operations. The first two methods are usually limited in their simple assumptions, that cannot meet the complexity of the studied problem with complex tool design or complex soil-tool interactions [50]. In this case numerical methods are recommended as they can simulate complex problems under controlled conditions assumed during the analysis, which include complex tool design and soil-flexible tine interaction. The finite element method (FEM), the discrete element method (DEM) and computational fluid dynamics (CFD) are among numerical methods, which have been used to model the interaction between soil and tillage tools, although FEM is the most commonly reported in the literature. Both the DEM and CFD are relatively new and less frequently used to model soil-tine interaction, for soil tillage problems, as compared to FEM. There are commercially available software packages that can be used for the simulation with reasonably accurate results, as reported by Shmulevich et al. [50], Tanaka et al. [55] and Hofstetter [24]. This depends on the correct assumptions and accurate determination of input parameters about soil, metal and the soil-tool interaction layer.

Both DEM and CFD are probably the best methods to simulate the interaction between soil and tillage tools, since they allow for crack propagation, which is a limitation of FEM. However, there are difficulties associated with the accurate determination of properties used as input, as the computational power are still

limited to simulate actual problems in practice that require a huge number of particles of different sizes for DEM. The inaccurate determination of material properties might result in undesirable errors between measured and simulated results. Some visual deviations in the soil-cracking behaviour between measured and DEM simulated results have been reported by Tanaka et al. [55], which were attributed to problems associated with the determination of soil parameters between the different particles and could only be solved with a trial-and-error method. Problems with soil parameter determination for DEM models, due to a lack of robust determining methods, were also reported by Asaf et al. [5]. He tried to obtain the soil parameters from a soil penetration test with different wedges and could only determine, satisfactorily soil parameters for a quasi-static, two dimensional, cohesionsless soil model, which would not be appropriate for the investigated simulation problem of the flexible tine. Hofstetter [24] encountered large errors in the vertical force simulation results in comparison to the corresponding results obtained from experiments, during modelling the interaction between a bulldozer blade and soil. Karmakar et al. [29, 30] used the CFD method for draught determination and soil disturbance on a flat and a narrow tine. They simulated the soil as a Bingham fluid and obtained acceptable draught results in comparison with the experiments for a shallow depth and lower working speed (difference around 23%). However, they also showed an unstable variation in draught for other working conditions (deviation between 1% until 42%). In my opinion the current stage of development of DEM and CFD requires further progress to enable accurate ground simulations of soil-tine interaction. Therefore, FEM was selected in this project.

The finite element method is a powerful numerical technique and is particularly useful for problems with nonlinear material and geometry behaviour, as well as where differential equations describing physical or biological phenomenon are nonlinear. In agriculture both nonlinearities in material and geometry can be encountered, especially when the problem under consideration is connected with soil, e.g. soil-tillage tool interaction or plant-soil interaction as reported by Upadhyaya et al. [56]. During the last decades FEM was increasingly used to

model the soil-tool interaction. Many researchers have reported finite modelling for different complex problems, because it is partly possible to overcome the limitations of analytical methods with respect to providing more information about the progressive failure zone, field of stress, displacement, velocity and acceleration of soil-tool interaction (Karmakar et al. [28]). Furthermore, different commercially available software packages, for example ABAQUS, COSMOS and ANSYS are provided with different inelastic material models and element libraries, including contact and interface elements, which make FEM even more attractive for these kinds of complex problems.

In the early nineties Chi and Kushwaha [9 and 10] developed a non-linear, three dimensional, finite element model of soil-simple tine interaction to acquire information about forces, soil stress, soil displacement etc. They concluded that the FEM has the capability of simulating different tool geometries, which was impossible with previous mathematical analytical methods, especially when the tools were curved. The geometry of the tool they used was simple (even blade) and could be modelled as a rigid body, where the motion is governed by a single node (rigid body reference node). The soil was modelled as a nonlinear stress-strain material, which was expressed as a function of minor and major principle stresses, based on the Mohr-Coulomb failure criterion. The interaction was accounted for with an interface element, that took also friction and adhesion between the blade and soil into account. The results of this analysis were evaluated by soil bin experiments and showed a good match for the draught from 0.8 % to 10.5 % at 45° and 90° rake angle, respectively. The vertical force was over-predicted for the inclined tool by an average of 20 % and under-predicted for the 90° rake angle. Nevertheless the draught force was the important force, because it could be directly related to the energy consumption of the tillage operation.

It was possible to study the dynamic effect on soil-tine interaction, as reported by Kushwaha and Shen [34], where they modelled a simple blade with 90° rake angle in interaction with clay at cutting speeds up to 55 km h^{-1}. In order to account for the geometric material nonlinearities of the soil, the updated

Lagrangian method and the Newton-Raphson method were used, respectively. They have reported over- and under-estimation of draught, based on the calculated draught at the peak or average peak of calculated draught, respectively. Zhang and Kushwaha [59] considered a tillage tool operating in soil as a cantilever beam, to study the response of the deflection, velocity and acceleration of the shank. The soil reaction force was assumed as a point load at the shank tip, so that only the tool behaviour could be determined. Nevertheless, the dynamic influence could be considered. It was found that the response of the shank was related to the natural system frequency and the applied soil cutting resistance. Furthermore, a proportional relation was found between length of the shank and the maximum values of acceleration, velocity and deflection and these values decreased with the tool stiffness. A more advanced model with respect to soil was presented by Rosa and Wulfsohn [47] where the rate dependent behaviour of a narrow rigid tillage tool, in interaction with soil, was simulated at a constant working depth and working speed. The soil was modelled as an isotropic and homogeneous continuum with a hypoelastic constitutive relationship where the Young's modulus and the Poisson's ratio were considered variable, which allowed to describe the dynamic soil-tool interaction. Although the model was capable of predicting trends of draught between the flat and triangular profile tool, specific average draught values for the triangular tine were overpredicted by 1 to 25 % as speed increased, which led to the conclusion that the correct representation of soil failure is of particular importance.

In the following years the FEM models were further developed to introduce applications with more complex tillage tools' geometries and sophisticated soil models. Gee-Clough et al. [18] developed a FE model to simulate the cutting of wet clay by a wide tine for two rake angles, namely 25° and 125°. The soil behaviour was expressed by a hyperbolic formula of stress-strain relationship. The soil-metal interaction was done with interface elements, which were updated during the simulation. Furthermore, soil-soil separation was considered below the tool tip, in front of the tool and upward. Soil slip effects were observed along the top part of the soil wedge. The working depth was 5 cm for both rake

angles. The simulation values and the measured values were similar for soil deformation and soil-tine forces, whereby the results for the 25° rake angle results were closer to the measurement, because the formed soil in front of the tine was more realistic. Fielke [14] used the FEM to simulate the interaction of a winged chisel plough share with soil, to understand and evaluate wear. The soil was modelled with the classical Mohr-Coulomb theory with elastic-plastic soil failure. Error between 10 and 20 % between FEM simulation and measured tool forces in the soil bin and in the field was reported. The soil movement results around the cutting edge also correlate well between the glass-sided soil bin and the FEM simulation. Plouffe et al. [45] developed a model for the interaction between a mouldboard plough and a clay soil. The plough had a complex curved cylindrical shape and was modelled as a rigid body. The interaction between the tool surface and the soil was not modelled with surface to surface contact elements. The critical state and the Mohr-Coulomb model were used to describe the soil and the soil-tool friction behaviour, respectively. The soil model did not consider the strain rate of the soil and soil cohesion. The results between the experimental data and the simulation showed a good match for draught with more than 1 m s^{-1} working speed. However, the vertical force was always significantly under-predicted in comparison with the experiments at two out of three working speeds, namely the highest and the lowest 0.25 m s^{-1} and 2 m s^{-1}. Further FEM simulation soil-mouldboard plough interaction was carried out by Formato et al. [15].The geometry of a curved plough, used for FEM, was determined with a micrometric slider at different points on the working surface. These spatial coordinates were used to obtain the plough shape with spline curves based on these points. To obtain the stress distribution, forces and moments acting on the working surface; a computational code, based on resolving mass balanced disturbance and energy, in a control volume around the plough was adopted. Two substances are utilised, namely air (external fluid) and soil as non-Newtonian material. The numerical results for the normal stress distribution on the working surface was in good agreement with the experimental results when minimum and maximum viscosity was equal (error less than 10 %). Abu-Hamdeh and Reeder [3] also reported a nonlinear three

dimensional analysis of the soil forces acting on a disc plough in clay and sandy loam soils. The stress-strain relationship of the soil material was modelled with a hyperbolic model. The results from the field experiments, in comparison with the simulations, showed good correlations for draught (error ranged from 0.9 to 9 %), vertical upward force (error ranged from 1.5 to 8 %) and side force (error ranged from 2 to 8.5 %). Mouazen and Nemenyi [39] simulated the interaction between a rigid subsoiler and a sandy loam soil based on the Drucker-Prager material model. In comparison to the previously used material models by other researchers, the Drucker-Prager model was more appropriate to model the behaviour of light soils. This model uses an elastic-perfectly plastic material law, which considers yield criterion and an associated flow rule. Furthermore, it describes the influence of hydrostatic pressure on soil failure. The tool was also modelled as a rigid body, by assigning much larger values of the Young's modulus than that of the soil elements. The interaction between the soil and tool surface was accounted for with 2-node rigid connector elements, and showed an appropriate use of this connection method for even more complex geometries. The deviation between measured and simulated draught in a soil bin was between 11.76 to 20.04 %. Moreover, Mouazen et al. [41] reported a good approximation between upward and forward soil failure length, which proved the FEM was not limited determining tool forces but could be used for parameters related to soil loosening. Furthermore, FEM can also be used to optimise tine geometries. Mouazen and Nemenyi [41] optimised the subsoiler geometry for least draught and maximum soil loosensing. Another geometry optimisation of a complex tillage tool was investigated by Jafari et al. [26] for a bent leg plough. The main difference in this case was the assumption that the tool is a deformable body, which was necessary due to the bending behaviour. The working depth of 250 mm was kept constant. The soil-tool interaction was modelled with contact surfaces without predefining the failure surface. As soil material law, the Drucker-Prager elastic perfectly plastic model was used. The optimized plow geometry achieved in this work from the FEM simulation provided a better soil disturbance. However, no validation with experimental work was reported. The previous mentioned soil-tine interaction cases were

modelled under quasi-static conditions, where a time dependent behaviour of the working process does not occur. Further simulation possibilities of complex properties with FEM were shown by Araya and Gao [4]. They developed a non-linear three-dimensional model to simulate subsoiler cutting with pressurised air injection. To model the soil, the Drucker-Prager strain hardening model was used and all parameters for this test were obtained from the triaxial compression test. Due to the air injection problem the mesh had to be designed in a specific way. The air load was applied from the nozzle port to the soil and it was assumed that at the nozzle port is an empty element without soil. Large errors of 10 to 30 % and 15 to 60 % were reported between measured and simulated values of sideward rupture distance and vertical soil movement, respectively. The simulated draught was always 1.6 times higher than in the soil bin test. Nevertheless, the FEM and the experiments showed a 20 % draught reduction when air injection is used. Abo-Elnor et al. [1 and 2] established a dynamic FEM analysis between a bulldozer blade and a sandy soil to investigate the relation between cutting speed and rake angle on draught, over large blade displacements. The blade was again modelled as a rigid body. A user defined, hypoplastic, behaviour based material model was used to account for nonlinearity between soil shear and normal pressure at high shear rates. The interaction between both parts were modelled in the same way as mentioned before by Plouffe et al. [45] with a master-slave contact surface concept where they disclaim to use connector elements. They have assigned predefined soil failure surfaces with partitions on the soil block. The working depth of the blade was 200 mm. No experimental validation was reported. It was concluded that the predefined failure surface was a proper solution for modelling the interaction between tool and soil. They have also concluded that the cutting speed had no significant effect on the cutting forces and that the cutting acceleration had an observable affect on cutting forces. All the above discussed FE simulations of soil-tine interaction proved that the FEM can be used successfully, with an acceptable range of error, particularly for draught. However, this also proves that there are some research gaps in this particular research domain. Most of the tools considered were modelled as rigid bodies.

To my knowledge there is no work on the use of FEM to model flexible tines, particularly when different parts of a tool are flexible to move relative to each other. Furthermore, this flexible behaviour will lead to changing in working depth, due to variable soil resistance and inertia forces. Furthermore, no FEM simulation of soil-tine interaction at shallow working depths of ≤ 30 mm, similar to that encountered during mechanical weeding with flexible tools can be found in the literature, particularly for narrow cross-section tines of less than 10 mm.

As described above that the complexity of mechanical weeding process necessitates the need of advanced knowledge about soil-flexible tine interaction to enable optimising the tine and harrow design for optimal harrowing operational conditions, that ensure efficient weeding (best selectivity at low energy requirement). So far no published work can be found in the literature about the use of the FEM to accomplish this simulation. Due to tine flexibility with a moveable tine tip the interaction becomes further complex, particularly under different mechanical tine settings and soil properties. Therefore, investigations will be made in this work to provide a better understanding of the interaction between different flexible tines and soil.

1.2 Aim and objectives

The following aim and objectives are proposed as a framework for this project, based on the gaps of research identified in the above mentioned literature review.

Aim

This project will implement the FEM to simulate the interaction between flexible tines and soil, aiming at finding optimal design parameters and operational conditions for optimal soil disturbance for mechanical weeding. Simulation of flexible tines' movement during the interaction with soil will be studied taking into account tine design parameters (rake angle and tine geometry), operational parameters (working depth and bulk density) and their influence on the draught and soil disturbance.

Specific objectives

The following specific objectives were considered to achieve the aim proposed in this study:

1) To design of a test bench for the experiments
2) To establish FEM model of the interaction between soil and flexible tines using an Abaqus 6.9 commercially available software.
3) To validate the results obtained from the FEM model with experimental data obtained in the soil bin of Cranfield University.
4) To determine the optimal operational conditions (e.g. working depth and bulk density) and design parameters (rake angle and tine geometry) that result in the least draught and optimal soil disturbance. This will be achieved based on the output of FEM simulation in a sandy loam soil.

1.3 Limitations of the project

Due to limitation of the project duration and the complexity and novelty of the investigated problem, specific limitations have been identified. Due to the dynamic behaviour of flexible tines at high speed, it is obvious that the problem investigated is highly dynamic. Furthermore, in regards to the real field situation, during mechanical weeding, a complex system of crop plants, clods, roots, and mixed terrain (soil mixed with stones etc) makes the simulation of this complex process even more complicated. It is nearly impossible to account for all these influencing factors in addition to the dynamic effect. That is the reason why controlled conditions have to be proposed during the simulation and soil bin test, which results in a simplification of the real problem, where the sole interaction of soil and a flexible tine was studied under static conditions. Karmakar et al. [28] also confirms the FEM limitation for the dynamic effect for the simulation of soil-tool interaction.

Furthermore, one task of the tine during mechanical weeding is to cover the weeds with soil, which necessitates cracking the soil. Nordell [44] reported that the FEM model requires the fabric to be continuous in nature, not allowing for separation, rotation, large scale deformation and displacement. The crack propagation in soils is not developed so far in the Abaqus 6.9 package, which explains why a further investigation about crack propagation is needed as this was not achievable in this study.

Cracks extremely influence the tine behaviour, especially at a maximum working depth of 3 cm. The inertia and the resistance of the soil are much smaller in shallow than in deeper working depths. The gaps that occur, due to the crack propagation, influence the tine tip dynamically. The advantage is that, after the first crack, a stable mean draught and working depth will occur, as also reported by Duerinckx et al. [12]. Due to these conditions, this work will be focused on the first contact between the flexible tine and soil to determine the maximum draught and tine upwards movement of the flexible tine until the first crack occurs, which means the dynamic aspects of soil cracking and their influence on the tine behaviour are not considered in this project.

2 Test bench

This chapter describes the test bench, the requirements of the test bench and the final design. Before the design process could start, a provider for the flexible tines were sought. Einböck[1] an Austrian company that produces tine harrows were contacted. They were interested in the project and agreed to provide six different tines in duplicate, with information about the tine material and commonly used rake angles and working depths.

2.1 Requirements of the design of test bench

The test bench was necessary to carry out the required experiments to validate the accuracy of the FEM simulation. Before the test bench was designed a list of requirements (Table 2.1) was created. In this list each bullet point was estimate as a hard or soft requirement. Bullet points, which are marked with an H are requirements that have to be fulfilled as specified and points with an S are those that can be modified according to the availability and feasibility under specific circumstances.

Table 2.1: List of requirements for the desing and manufacturing of the test bench

Thesis J. Theuer		**List of requirements** for the design of a test bench to investigate a flexible tine	01/11/2010
Changes	**H S**	**Requirements**	
	H	**Loading:** • Forces from 0 to 300 N	
	H	• Usage of available load cells	

[1] Further information's about the company are available under www.einboeck.at.
[2] The size of the wet soil bin is 6000 mm by 1000 mm by 1000 mm.

	H	• Central point of force application
		Sensors and measurement kits:
	S	• Sensor for draught until 300 N
	S	• Sensor for vertical force until 300 N
	S	• Sensor for tine tip movement in upward and sideward direction up to 5 cm
	H	• Measurement kit for bulk density
	H	• Measurement kit for moisture content
		Traction engine
	H	• Engine with constant speed (Maximum: 12 km h^{-1})
		Soil bin
	H	• Length: minimum of 200 cm
	H	• Width: minimum of 20 cm
	H	• Depth: minimum of 10 cm
	S	• Fast and easy to refill
	H	• Adjustable in height by a single person
		Flexible tine
	H	• Adjustable in height and rake angle position by a single person
	H	• Replaceable by a single person
	H	• Tine constrained as on the real frame
	H	• Global movement only in travel direction
		• Two different working depths (2 cm and 3 cm)
		Soil
	H	• Sandy loam soil
	H	• Homogenous structure
	H	• Two different bulk densities of 1450 kg m^{-3} and 1600 kg m^{-3}
	H	• One moisture content of 11.5 %

The measured values during the experiment were draught, vertical force, tine tip movement in upward and sideward directions, bulk density and moisture content of the soil. The maximum tine forces during the experiment were calculated using the narrow tine theory of soil cutting [20] to get a preliminary estimation of the expected draught and vertical force. This was then used to choose the best load cell, to record tine forces, during the soil bin test. The point of force application should be in the central position of the load cell to avoid unwanted bending moments, and provide a straight power flow. The traction engine should be able to provide a constant speed to avoid variations during the measurement. The soil bin has to have a minimum size as mentioned in Table 2.1, otherwise the preparation time will increase dramatically. Due to the different rake angles and working depths, the soil bin and the flexible tine have to be adjustable in height to achieve the desired settings. The test bench should be moveable upwards and downwards to set the required working depth. The soil bin experiment was proposed to be carried out by a single person, hence this adjustment had to be easily done. The tine should be constrained as this was used on the actual frame, mimicking the actual working conditions during the experiments, otherwise a difference in tine mounting could influence the interaction behaviour with soil. Furthermore, the tine should only be pulled in the travel direction, so that no relative movement in other directions is possible.

The soil is the other part of the test bench. In the test ground a sandy loam soil was available. The prepared soil structure was homogeneous in the same test and between different tests with same proposed conditions, to exclude the effect of variable influencing parameters that complicate understanding of the experimental output. The soil was compacted to two different bulk densities of 1450 kg m^{-3} and 1600 kg m^{-3} and one moisture content of 11.5 %.

2.2 Design of the test bench

The test bench can be divided into different parts, namely: a soil bin, a frame (cradle), a traction engine, an octagonal load cell, to measure draught and vertical force, displacement sensors to measure the movement of tine tip, a

data logger, a computer as record and storage device and an adapter between cradle and flexible tine. Figure 2.1 shows an overview of the whole test bench with the different parts.

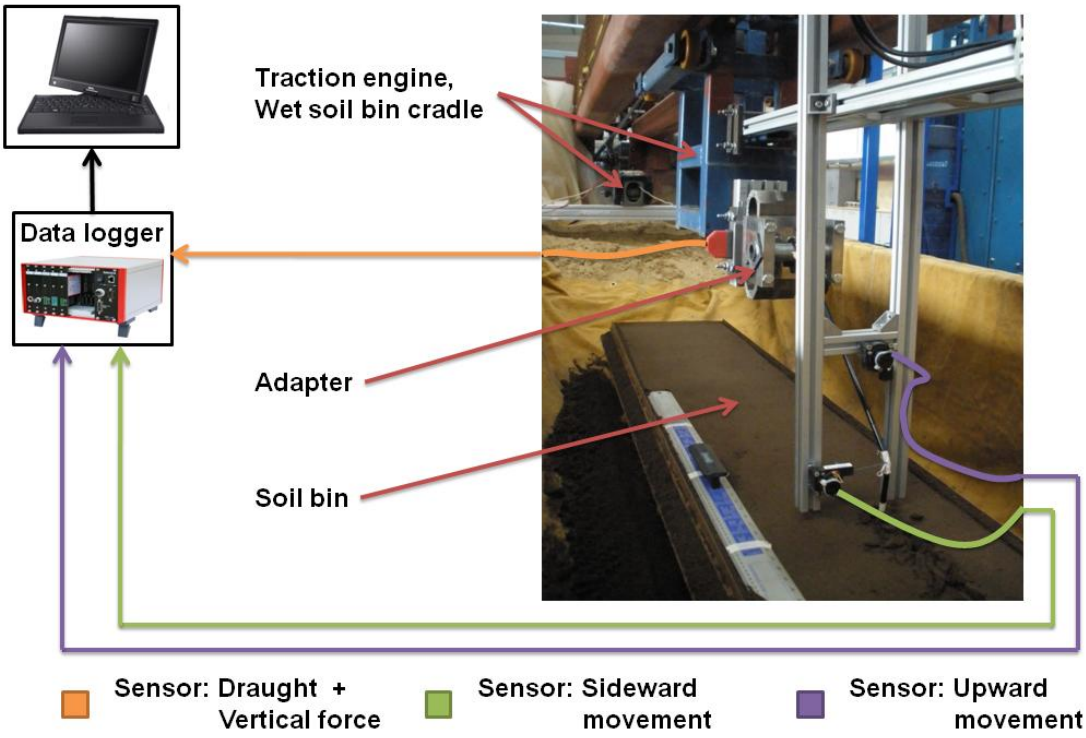

Figure 2.1: Overview of the test set-up

2.2.1 Traction engine and soil bin

The wet soil bin[2] normally used for drainage projects is one of the soil bins available at Cranfield University. In Figure 2.1 the wet soil bin not completely filled with sand and connected to a system of water pipes to flood the entire bin is covered with a yellow tarpaulin. For this experiment the wet soil bin was used as foundation for a smaller soil bin (Section 2.2.4), which is marked in Figure 2.1. With the sand existing in the wet soil bin, the position of the smaller soil bin above the sand could be well monitored. Before the test, the sand was wetted, excavated, levelled and compacted to the right depth for each rake angle. Next

[2] The size of the wet soil bin is 6000 mm by 1000 mm by 1000 mm.

the sand was covered with five millimetre aluminium plates and a tarpaulin to avoid soil mixture between the sand of the wet soil bin and the sandy loam soil used in the current experiment. A further advantage of using the wet soil bin is the cradle designed over the wet soil bin, which can be only moved in one direction and can be linked with different sensors and adapters. As traction engine, a commercial available cable winch[3] was used (Figure 2.2).

Figure 2.2: Cable winch mounted on aluminium profiles to provide traction to pull the flexible tines

The winch was mounted on two aluminium profiles[4], which were fixed with clamps on the wet soil bin. It was powered by a 12 V tractor battery and provided a constant working speed, which depends on the acting traction force. During the experiments an average working speed of 0.037m s^{-1} was achieved.

[3] Manufactured by Shinn FU Europe, Holland
[4] The size of the aluminium profiles for the cable winch is 80mm by 80mm by 1150mm.

2.2.2 Adapter and tine

A new adapter was designed and manufactured for this project at Cranfield University. This was necessary to link the flexible tine with the cradle. Figure 2.3 shows the entire adapter illustrating different individual parts.

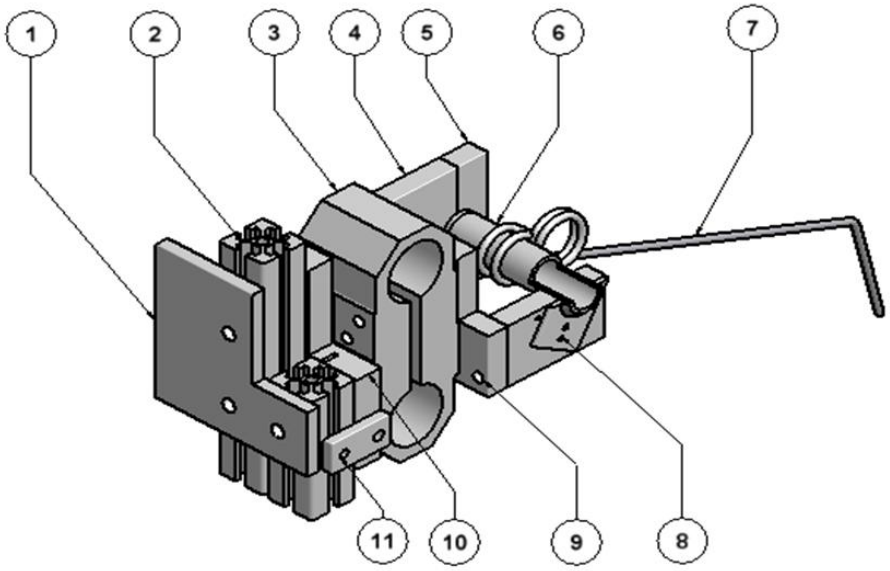

Figure 2.3: The adapter with different parts (**1**-Cradle, **2**-Aluminium profiles, **3**-Load cell (EORT), **4**-Side plate, **5**-Lid, **6**-Axis, **7**-Flexible tine, **8**-Small plate, **9**-Back plate, **10**-Adapter plate, **11**- Fixing plate).

The adapter was designed for a single flexible tine (7) (Figure 2.4). Further information about the different tine dimensions are provided in the appendix A.1. The main parts of the tine are the tine tip, which is in interaction with the soil. A torsion spring is to exert continues downward forces on the tine tip, to overcome the soil reaction force and thus pushes the tine back into contact with the soil. The mounting part is to connect the tine with the general frame besides the other tines. The tine is usually painted in black, which usually disappears after a few operations in the field. Therefore, the paint on the tine tip was

removed before the experiments, to ensure external friction between soil and metal is similar to actual field conditions.

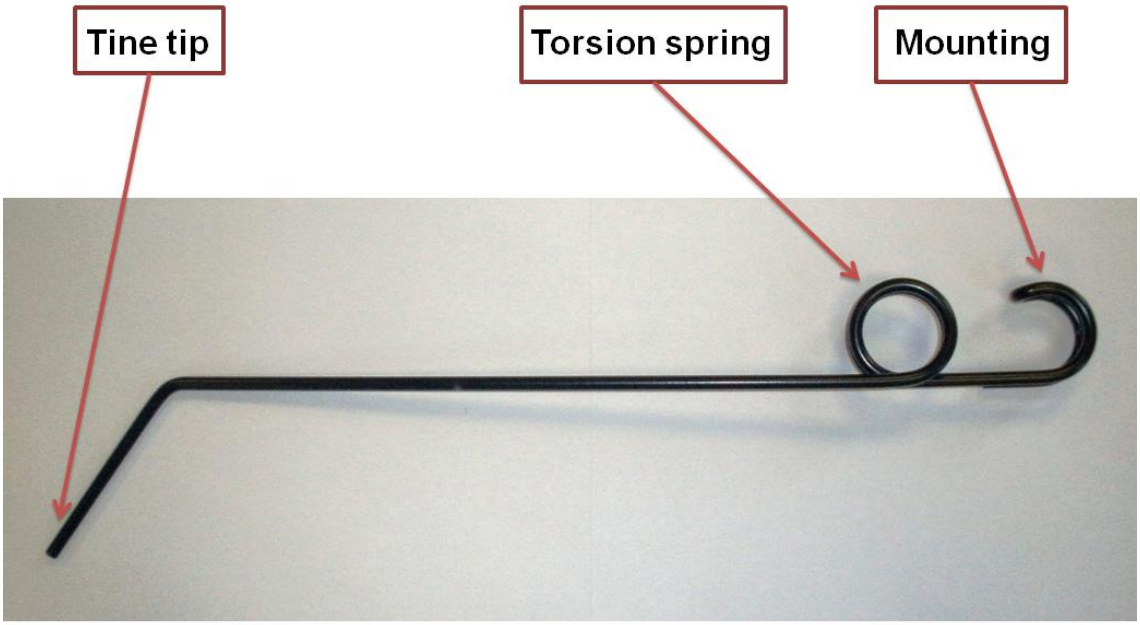

Figure 2.4: Flexible tine 15-129 provided by the Austrian manufacturer Einböck

The tine is screwed in the middle of the axis (6) (Figure 2.3) to achieve a symmetrical power flow to the load cell (3). The axis was a standard pipe and is designed in the same way as it is used by the manufacturer, to achieve similar conditions during the experiment. On this axis there was a small plate with two boreholes (8). This plate was welded with the axis and was used to change the rake angle of the tine. It was possible to choose among five different rake angles (Figure 2.5), namely, 56°, 68°, 80°, 92° and 104°. The axis was set between two side plates (4) and two lids (5). The side plates and lids were screwed together and tightened around the axis, so that no radial movement can occur. The small plate (8) was screwed with one of the side plates (4) to avoid axial movement of the axis. The side plates were linked with the back plate (9) and this back plate was directly connected with the load cell (3). The

load cell was fixed on an adapter plate (10), which was screwed with four fixing plates (11) to standard aluminium profiles[5] (2).

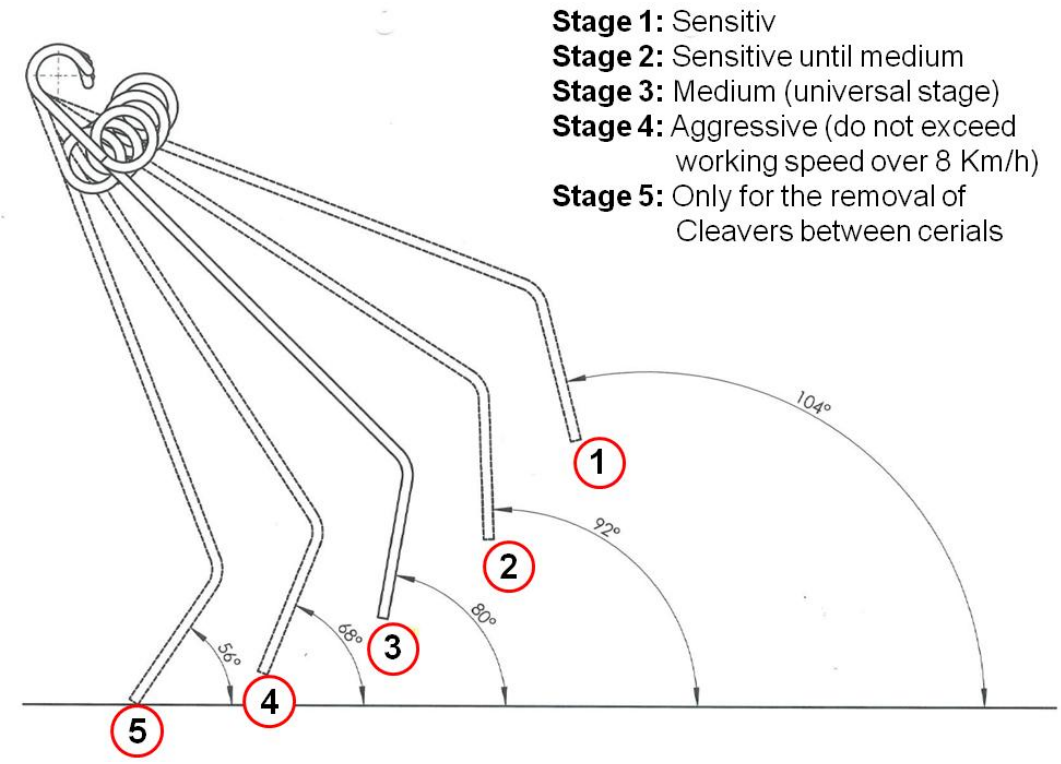

Figure 2.5: Common rake angles for the flexible tine provided by Einböck

At the end, the aluminium profiles are connected with the cradle[6] (1). In regard to the list of requirements (Section 2.1), all requirements could be fulfilled. The rake angle and the height of the tine were adjustable. The aluminium profiles enabled the adjustment of height, so that, it was possible to set different working depths and all these were manageable with a single person. Drafts drawings for the individual parts of the adapter can be found in the appendix A.2.

[5] The size of these aluminium profiles is 45mm by 45mm by 225mm.
[6] Figure 2.3 is only showing the linkage plate of the cradle, which is one part of the entire cradle.

Force flow from the tine tip to the load cell

This subsection describes force flow from the tine tip to the load cell, as shown in Figure 2.6.

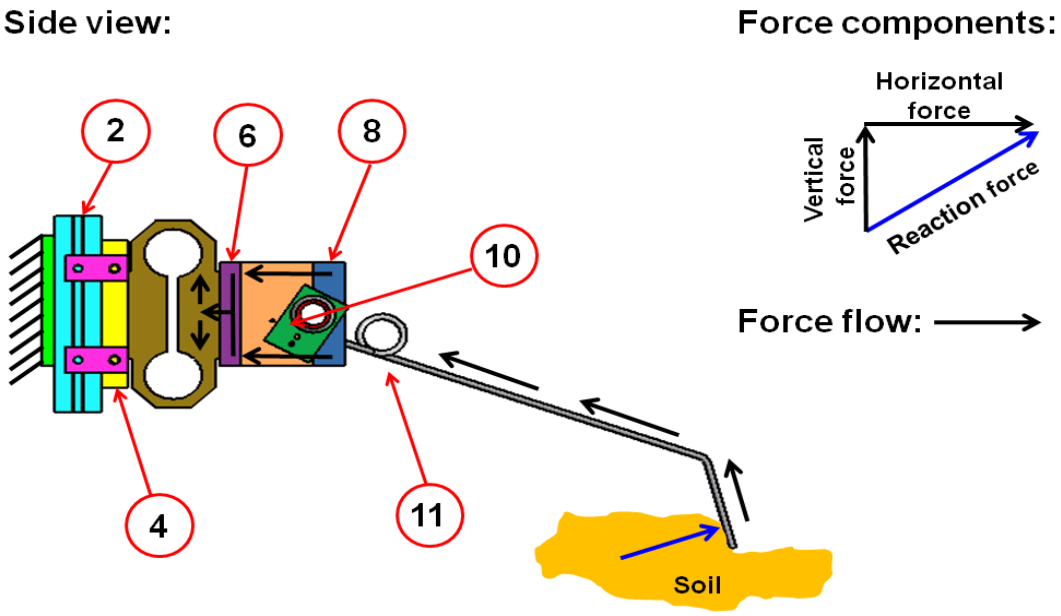

(a)

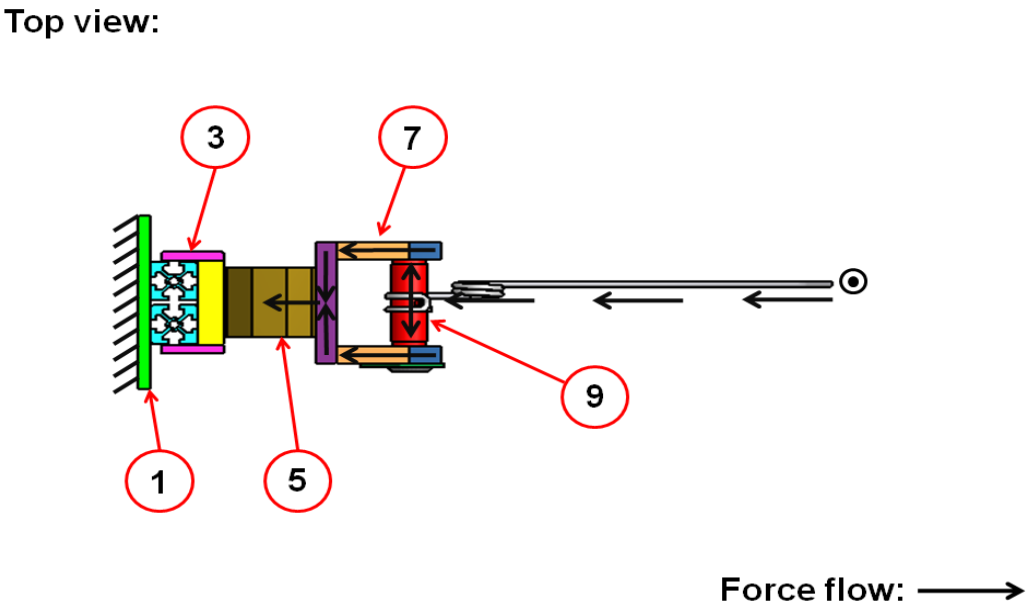

(b)

Figure 2.6: Force flow through the adapter and force components acting on the tine tip (**(a)** Side view: **2**-Alu profile, **4**-Adapter plate, **6**-Back plate, **8**-Lids, **10**-Small plate, **11**-Flexible tine and **(b)** Top view: **1**-Cradle, **3**-Fixing plates, **5**-Load cell (EORT), **7**- Side plates, **9**-Axis)

If the tine is pulled through the soil a reaction force (blue arrow), due to soil resistance to penetration occurs between the tine tip and the soil. The resultant force can be divided into two components, namely, a vertical force and a horizontal force (draught). The ratio of division between these two forces depends on the rake angle [12]. Figure 2.7 shows the force distribution at two rake angles. A rake angle larger than 90° (Figure 2.7a) means the vertical force component (5) acts as to push the tine upwards out of the soil and creates (due to the tine leg bending) a positive vertical force (2) on the load cell. With a rake angle under 90° (Figure 2.7b) the vertical force component (2) on the tine tip points downwards, which causes positive vertical force on the load cell. This downwards vertical force means the tine is pushed into the soil. The draught on the load cell (1) acts always in an opposite direction to the horizontal force on the tine tip. The difference in the overall acting force direction is in-line with previous research [10, 18 and 39]. The resultant force flows further up through the tine (11), through the torsion spring, where a torsion moment reacts against the resultant force to push the tine tip back into the soil, until they reach the linking axis (9). The resultant force acts as a pulling force on the axis and, due to the symmetric arrangement of the flexible tine on the axis, this force flows equally over the two lids (8) and the side plates (7) into the back plate (6), which is fixed (screwed) to the load cell (5). The particular design of the load cell as explained in Section 2.2.3 allows both flanges to move relative to each other and this relative movement is measured with strain gauges[7]. The relative movement occurs because one flange side of the load cell is not constrained and the other one represents a fixed restraint with the cradle (1).

[7] Strain gauges are based on the principle of resistance change in a conductive wire or metal foil caused by deformation, namely, transversal contraction.

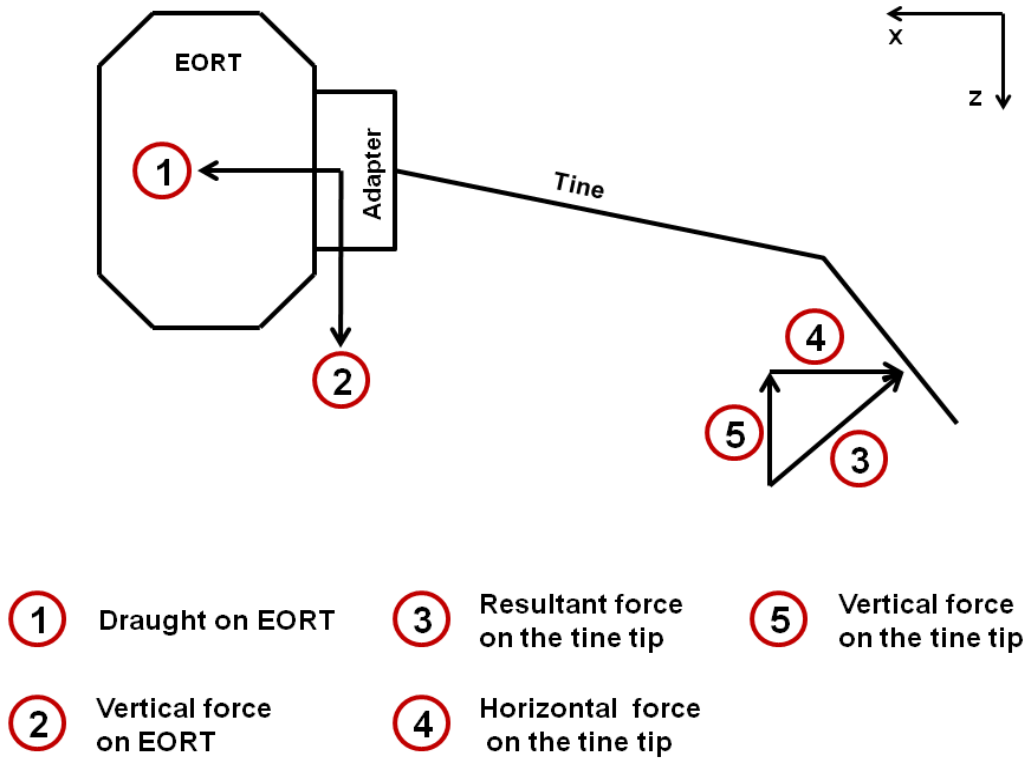

(a)

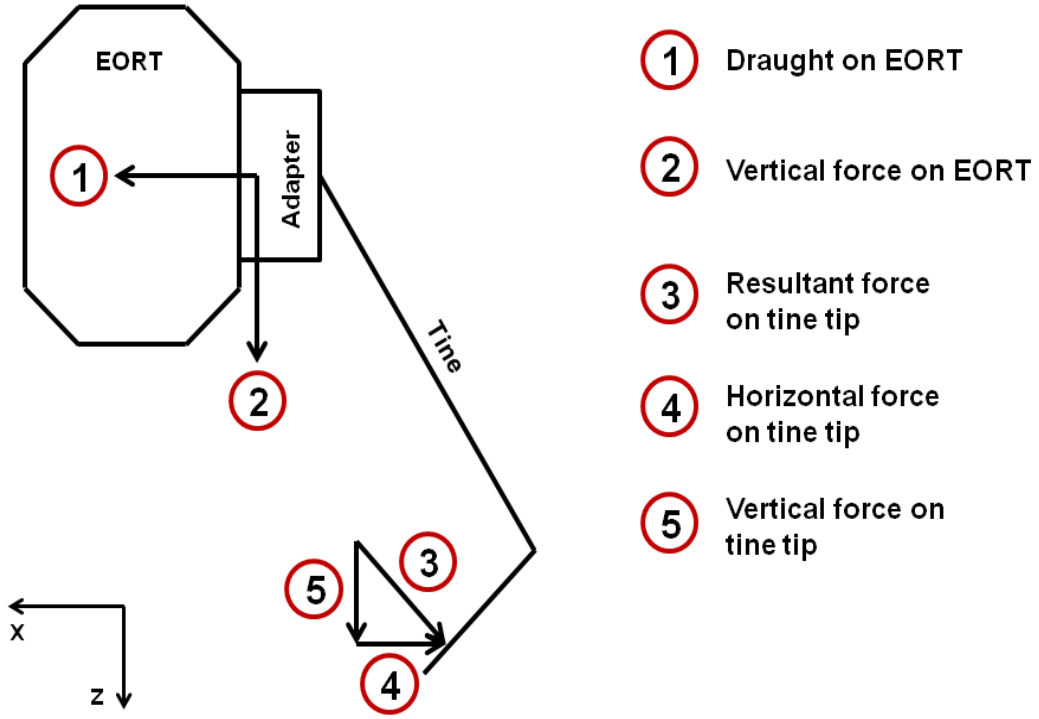

(b)

Figure 2.7: Illustration of force components and directions acting on the tine tip and the load cell for **(a)** a rake angle > 90° and **(b)** a rake angle < 90°

2.2.3 Measurement kit

This section provides an overview of the used sensors and measurement kits in the test bench to measured draught, vertical force, upward and sideward movements of the tine tip, soil moisture content and bulk density. Therefore, the next subsections will explain the different sensors, their function and their arrangement in the test set-up.

2.2.3.1 Sensor for draught and vertical force

For the measurement of draught and vertical force, an extended octagonal ring transducer[8] (EORT) was used. The EORT was made of a metal block of steel, with the design shown in Figure 2.8. At specific areas of the EORT strain gauges are glued. These areas are called strain nodes, where there is no influence of strain from the other force component. The strain gauges are connected as a bridge circuit, named, Wheatstone bridge, which has the advantage of a small measurement error due to a higher sensitivity. This load cell is not commercially available and was designed and manufactured at Cranfield University [19].

[8] It is possible to measure the resulting moment caused by the horizontal force with the EORT [19] but this function was not used in this work.

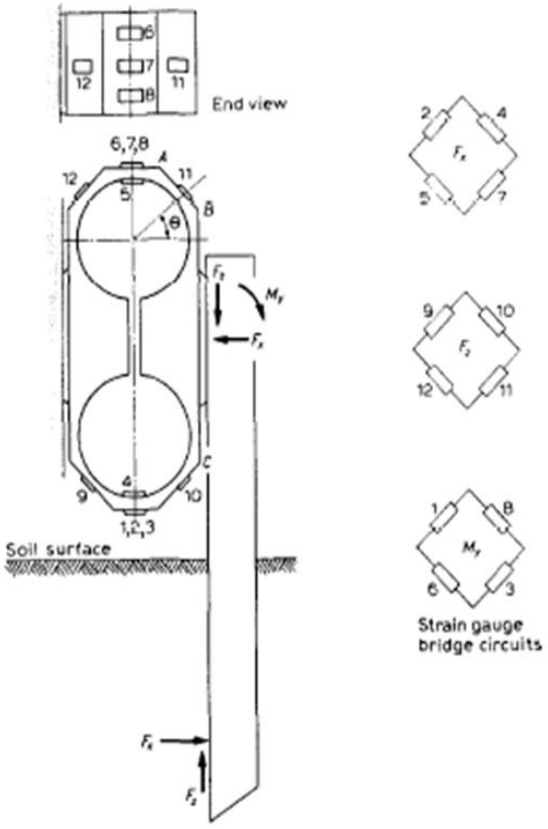

Figure 2.8: Extended octagonal ring transducer (EORT) with acting forces and moments and the position of the strain gauges (After Godwin) [19]

The capacity of EORT adopted in this study was of a maximum force of 20 kN with 1 N resolution. The load cell was directly connected with the data logger, as shown in Figure 2.1 and was arranged in a row with the adapter and the cradle as illustrated in Figure 2.3. The positive draught was recorded in the travel direction and the positive vertical force was in the downward direction, pushing the tine in or out of the soil depending on the rake angle. The calibration data for both forces can be found in the appendix A.3.

2.2.3.2 Sensors for upward and sideward tine movement

String potentiometers[9] (Figure 2.9) were used to measure the upward and sideward movements of the tine tip. The function of the draw string potentiometer is quite simple (Figure 2.10).

Figure 2.9: String potentiometer from UniMeasure used to measure the tine tip movement in upward and sidway directions

There is a torsion spring (3) in the housing of the sensor (5). On one side, the spring is coupled with a spool where the string is wound (4), whereas on the other side of the spring there is a potentiometer (2). The function of the torsion spring is to bring the string back into the housing. Every time when the string is pulled out, the spring is turned and at the same time this movement changes the resistance of the potentiometer which causes a change in voltage (1), which is directly recorded. This means that every length of the string has a specific voltage. The string potentiometers (Figure 2.9) used was with a total string

[9] These string potentiometers (Model LX PA 15) were manufactured by UniMeasure, USA.

length of 390 mm and a sensitivity rating of 2.5 $\frac{mV}{\frac{V}{mm}}$. The sensors were mounted on a frame made of aluminium profiles[10] and the strings were knotted and taped around the bent part of the tine leg (Figure 2.11).

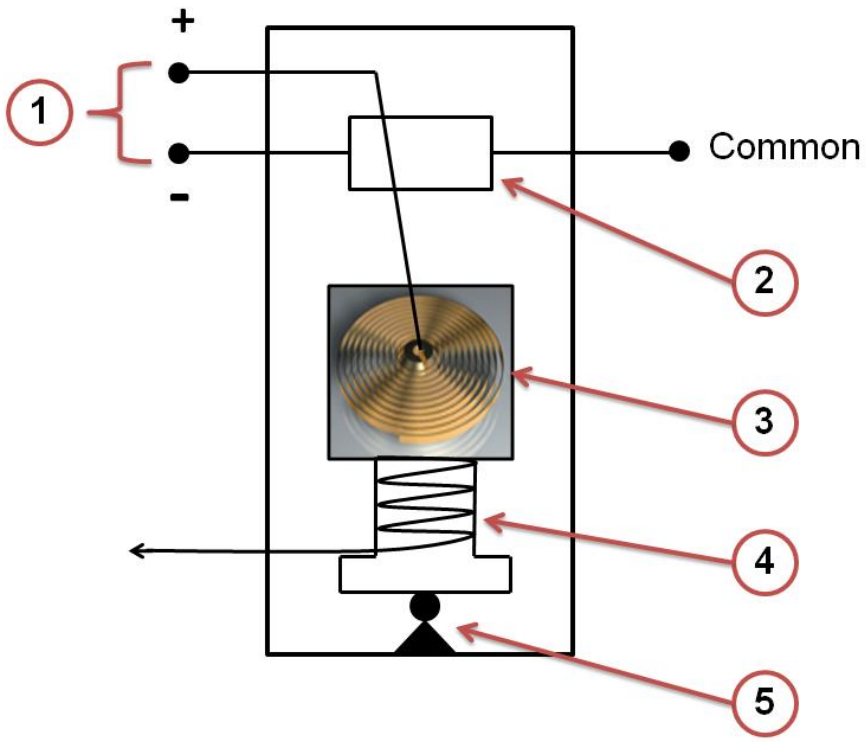

Figure 2.10: Illustrates the schematic drawing of a string potentiometer sensor (**1**-Measurement of signal in Volt, **2**-Potentiometer, **3**-Torsion spring, **4**-Spool with string, **5**-Bearing with housing)

The use of two string potentiometer sensors was based on the assumption that when the flexible tine is fixed on the adapter axis, the tine tip cannot relatively move in the direction of travel. The upward and sideward movement in regard to the total length of the tine are so small, to the extent that these movements can be assumed to be linear. This means that the two string potentiometers can measure the maximum tine tip displacement in the y-z plane. Furthermore, the furrow dimension was measured with a calliper to confirm the tine tip movement

[10] The size of these profiles is 30mm by 30mm by 1000mm.

after each run. The calibration data for both sensors can be found in the appendix A.3.2.

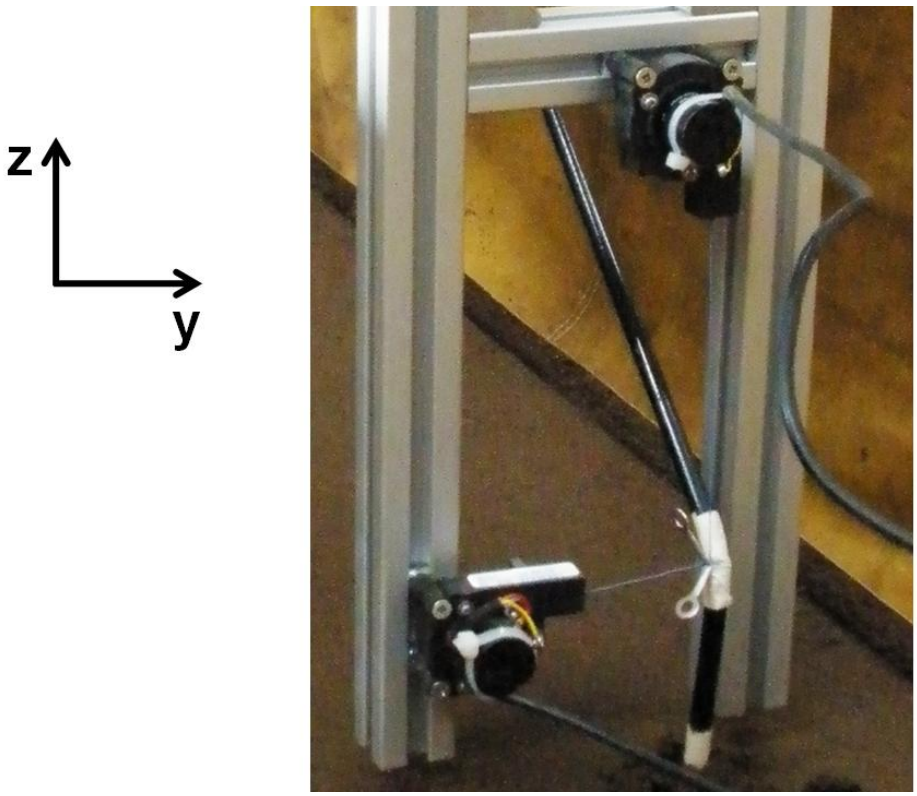

Figure 2.11: Positioning of two string potentiometers on the aluminium frame to measure movement of flexible tine tip

2.2.3.3 Measurement soil moisture content and bulk density in the soil bin

Soil samples were collected in the soil bin as shown in Figure 2.12. They were used to measure soil moisture content and bulk density. Three samples were collected for a run, which were distributed along the length of the soil bin and collected as close as possible to the furrow of the flexible tine (Figure 2.12) to ensure that the right moisture content and bulk density are measured. The gravimetric moisture content was considered in this project. The soil sample has to be weighed directly after it was collected to avoid water evaporation. After weighing, the soil sample was dried in an oven at 105°C for 24 hours, after

which the sample was weighed again. The ratio between wet and dry soil weight is then the gravimetric moisture content as presented by Warrick [58]:

$$\theta_m = \left(\frac{m_{wet} - m_{dry}}{m_{dry}}\right) \times 100 \qquad (2.1)$$

Where θ_m is the gravimetric moisture content [%], m_{wet} is the soil sample mass before oven drying [kg] and m_{dry} is the soil sample mass after oven drying [kg]. In this study a Kopecki ring method was used for the measurement of soil bulk density.

After drying, soil bulk density was calculated as the weight of wet soil per volume of the cylinder. The soil bulk density was measured randomly during the day, because previous tests[11] showed that the soil preparation procedure adopted in this project was very accurate. The deviation of moisture content and bulk density was less than 4 and 3%, respectively. This result was also confirmed during the experiments.

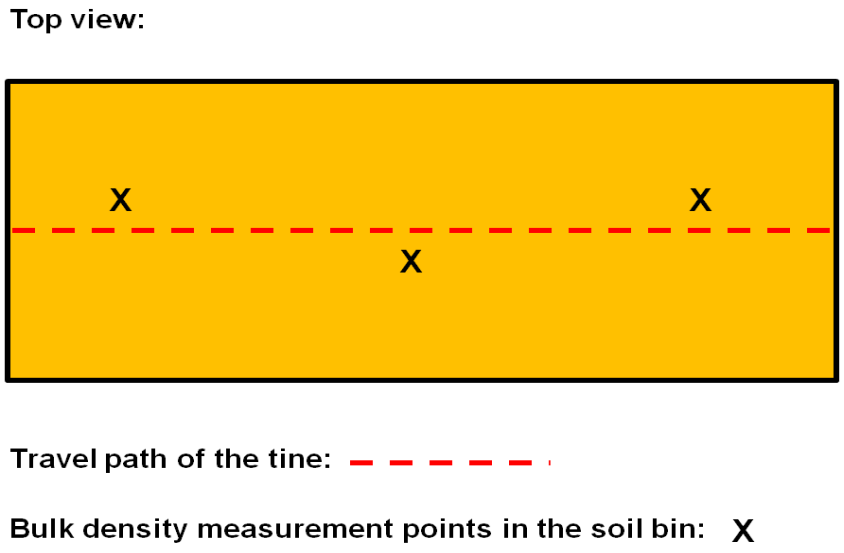

Figure 2.12: Illustration of measurement points in the soil bin for bulk density and moisture content

[11] Previous tests for the development of a procedure for the soil preparation were investigated and verified with bulk density and moisture content measurements.

2.2.3.4 Data logger and computer

The measured signals from the different sensors have been collected, prepared and stored. For this task an data logger and a laptop were used.

Data logger

The data logger is a device which is used to filter, linearise, amplify and standardise measured signals. For the experiments a bridge transducer and strain gauge amplifier (Figure 2.13) with four channels was used. The bridge transducer was designed as a Eurocard subrack[12] and the housing was equipped with two of these cards, with two channels per card. The cards with the green and red light-emitting diodes (LED) are necessary for the power supply and the auto zero of the measurement cards, respectively. For each channel it was possible to set up a gain-factor to achieve a suitable measurement range for each measured signal. The sampling rate of the bridge transducer is 10 kHz[13]. The data logger was connected to a laptop with a Universal Serial Bus (USB) for the data exchange.

Figure 2.13: Data logger with front panel (left) and back panel (right)

[12] Standardise Eurocard format after DIN 41494
[13] Data from the technical user manual, available in the soil bin.

Computer and software

A standard laptop was used to collect and store the measured data. For this purpose a new measurement programme, named, "*Flex tine 1.0*" was designed with DasyLab[14] version 8 software to visualise and save the measured data. DasyLab consists of two levels. The first level is the user interface, called, layout (Figure 2.14) and the second level is the source code, designated as worksheet (Figure 2.15). The worksheet contains the function modules and the data flow logic. Each module input and output has to be connected with a wire to realise data flow. The whole programme works on the basis of drag and drop. In the function menu (11) the desired function has to be chosen and then dragged with the left mouse button and dropped on the worksheet. In this way all the function modules were pasted into the worksheet and then connected with the wires in the desired arrangement.

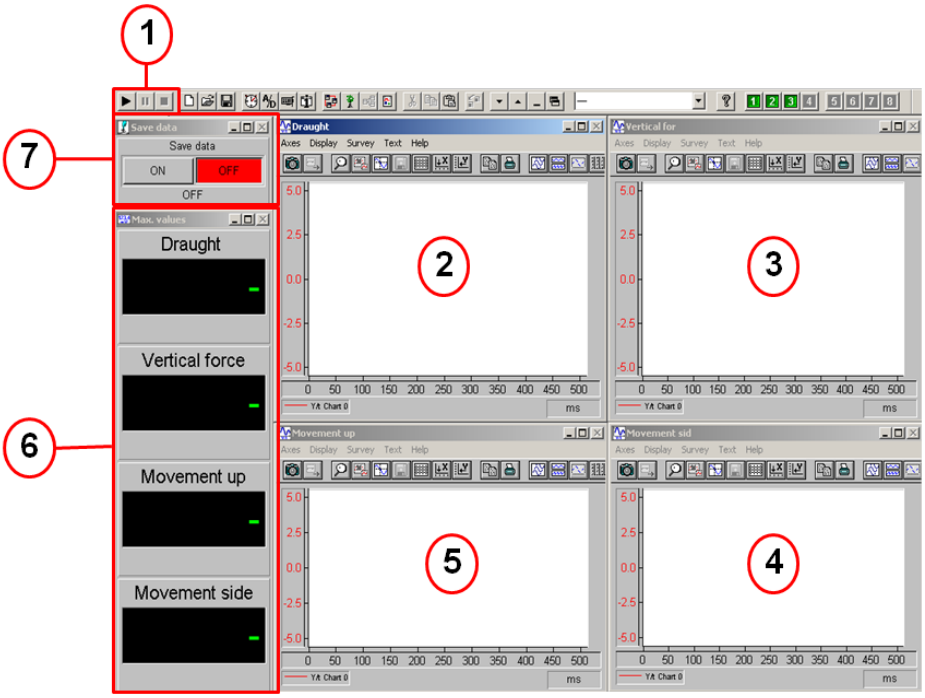

Figure 2.14: DasyLab user interface (Layout) of the measurement programme

[14] Measurement software is designed and provided by National Instruments.

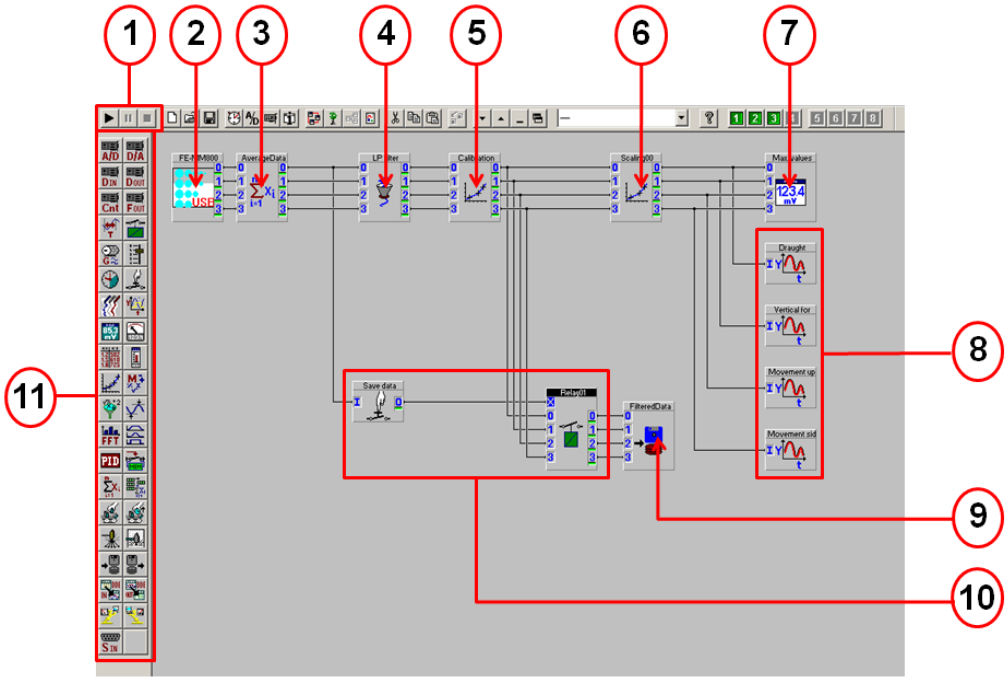

Figure 2.15: DasyLab back panel (Worksheet) of the measurement programme with source code

In the actual worksheet of the programme thirteen function modules were used. With the buttons in frame (1) the programme can be started and stopped. Then the data will be transferred from the data logger into the laptop. To ensure communication between both devices, a USB module was inserted (1). With a double click on a function module a further interface appears where different settings for the respective module can be made. In the USB module, the number of channels, the name of the communication port and the sample rate could be specified. A sampling rate of 50 kHz was chosen during the experiment. The next function module is an average function (3), which was designed to average the incoming data for every 100 samples, to reduce the sample rate to 500 Hz. Before this sample rate was chosen, data were recorded with 50 kHz and analysed with a fast Fourier transform (FFT) to ensure no aliasing effect had occurred. Then the data will be filtered (4) with a Butterworth filter at a cutting frequency of 50 Hz to avoid noise on the measured signal from

the mains voltage. After that the data reach the calibration module (5), where the linear equation of the regression line from the calibration data (Appendix A.3) can be filled in. The voltage value could than be translated into the appropriate unit of the measured signal. These data were transferred to the write data module (9), which includes data saving and visualisation modules (7 and 8). The write data module was not activated at all time (can be switched on and off with modules in frame 10). The folder, the file name, the file extension and settings of the data arrangement in the file were made with a double click on the write data module, which was done for every single measurement. Before the data reaches the visualisation modules they have to go through a scaling module (6) to remove the signal offset. Then they are visualized in four digital meters (7), where the mean value of each block and the whole developing of the values (four graphs (8)) are shown. The entire function modules mentioned above are available in frame (11).

There is another panel in the programme, called the layout, which is the real user interface (Figure 2.14). The graphs, buttons etc. are all linked with the worksheet and appear when a function module is been created in the worksheet. The parts in the layout are placed in different windows and can be enhanced, reduced and moved. Frame 1 is again to mark the start, break and stop button of the programme. These buttons have to be pressed to start the programme. On the right hand side of the programme there are the graphs, which show the entire development of the values during the measurement. Graphs (2), (3), (4) and (5) show respectively the draught, vertical force, sideward and upward movements of the tine tip. In frame (6) the digital meters for each channel is found, which show the mean trend value of the respective graph and in frame (7) is the switch to start (“ON”, shines green) or stop (“OFF”, shines red) the data saving.

2.2.4 Soil bin

The soil bin (Figure 2.1) was a metal box made of two millimetre thick steel with dimensions of 2000 mm by 400 mm by 200 mm, which allows sufficient space in travel direction for few measurements and replicates under the same measurement conditions without the need for preparing a new soil for every single measurement. The width was not crucial in this case because the cradle was not moveable in a lateral direction. It was important to ensure that the tine had enough space in a sideways direction, so that the soil disturbance is not affected by the side walls of the soil bin. A minimum depth was necessary for a good soil preparation (Section 3.1.1). As explained in section 2.2.1, a small soil bin was placed into a bigger wet soil bin and in this one the soil was levelled to an appropriate height to accommodate tines with different rake angles and tine lengths. This was one of the challenges to find a suitable way to change the height of the bin, to accommodate different rake angles ranging from 56° to 104° and different tine lengths from 490 mm to 600 mm, which required adapting the height of the soil bin by more than half a meter. The advantage of the small soil bin was that the preparation of homogenous soil conditions could be easily done, which save time and effort as compared to the use of the big soil bin available at Cranfield University. Further information about the soil preparation can be found in section 3.1.1.

3 Experimental procedures

Experiments are helpful resources to understand complex phenomena under real conditions. The requirements of an experiment are to provide measurable results, be comprehensible, repeatable and objective. Experiments were done to measure the interactive behaviour of flexible tines and soil during mechanical weeding and to obtain material properties, related to soil material parameters, and soil-metal interaction properties needed for the FEM simulation. Therefore, this chapter will present all experiments done during this project and will explain how the experiments were performed.

3.1 Soil bin experiment

The soil bin facility is available at Cranfield University. A modern building opened in 2008 contains three different soil bins, a soil lane and other testing kits and facilities for design and manufacturing purposes (Figure 3.1).

Figure 3.1: View to the test ground at Cranfield University. The blue cradle is working on the big soil bin and next to it is the wet soil bin

All the six different tines were examined during the soil bin test. Table 3.1 shows the measurement matrix with different parameters for tine 15-129, shown as an example. These tests were carried out under two bulk densities (1450 kg m^{-3} and 1600 kg m^{-3}), two working depths (20 mm and 30 mm) and three different rake angles (56°, 80° and 104°). Due to time limitation three out of five rake angles proposed by the manufacturer were chosen (Section 2.2.2 and Figure 3.2). One moisture content level of 11.5 % was chosen for all tests. These different experimental conditions have resulted in 36 different runs to be performed in three replications for each set-up.

Soil is a complex and highly non-homogeneous material, which requires narrowing down its variability to enable useful information about soil-tine interaction to be extracted. However, the preparation of a homogeneous soil structure that is identical for different measurements, to allow repeatability for different replications, is a complex task and will be discussed in the next section.

Table 3.1: Overview of the different experiment settings for tine 15-129, shown as an example

	Tine 15-129											
	1. Bulk density (1450 Kg m^{-3})						**2. Bulk density** (1600 Kg m^{-3})					
	Working depth (2 cm)			**Working depth** (3 cm)			**Working depth** (2 cm)			**Working depth** (3 cm)		
	1. ATT	2. ATT	3. ATT	1. ATT	2. ATT	3. ATT	1. ATT	2. ATT	3. ATT	1. ATT	2. ATT	3. ATT
Angle 56°												
Angle 80°												
Angle 104°												

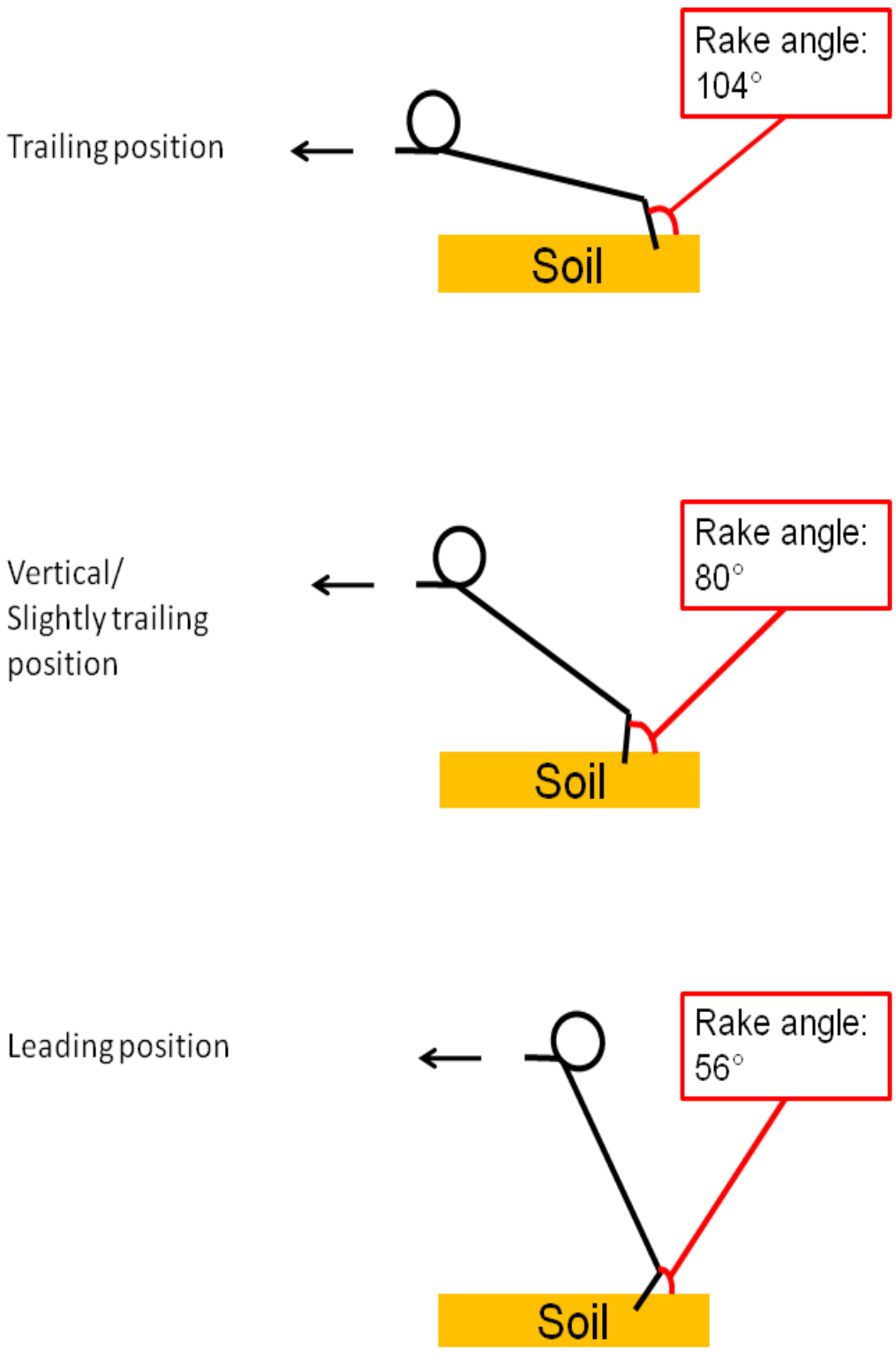

Figure 3.2: Tine orientation for the three chosen rake angles for the same tine

3.1.1 Soil preparation

The main aim of soil preparation was to develop a procedure to achieve two different bulk densities of 1450 kg m^{-3} and 1600 kg m^{-3} for identical moisture content. The soil used was a sandy loam with the following soil texture fractions of 65.73 % sand, 17.18 % silt and 17.09 % clay. The soil was excavated from local fields around Silsoe[15]. This soil is commonly used for experiments in the soil bin. The unprepared soil was completely dry and contained big clods and stones. Therefore, the soil was sieved with a 6 mm sieve. After sieving, a specific amount of water was added (10 % of the soil weight), after which the soil was mixed carefully with an electric soil mixer to achieve homogeneous wet soil material. The resulted moisture content of the soil was 11.5 % d.b. This particular moisture content determined with a proctor test[16] was necessary to achieve the specific bulk density of 1600 kg m^{-3}. The soil was freshly prepared every day to ensure constant and identical conditions during the entire experiment. Tests showed that moisture content decreases slightly after a day.

When soil moisture content was set to the desired level, soil has to be compacted in the soil bin. Therefore, the soil has to be prepared in several layers, as shown in Figure 3.3. Due to the maximum working depth chosen for different tines of 3 cm, in an overall depth of the wet soil bin of 20 cm, it was suggested that a base layer of 14 cm, above which six layers of 1 cm thick each, were prepared.

[15] Silsoe is placed in the Central Bedfordshire, United Kingdom.
[16] Further information about this test can be found in the standard ASTM D698-07e1.

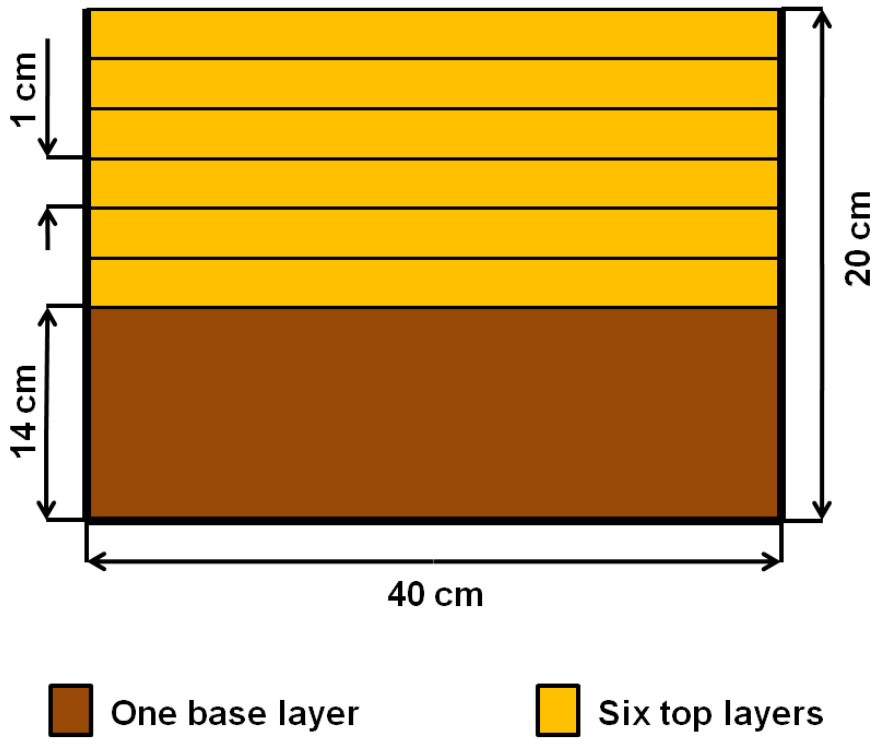

Figure 3.3: Soil profile as prepared for the soil bin tests

The base soil layer was hard compacted to provide a good foundation for the six upper layers, which were compacted to the desired bulk density. Previous experiments confirmed that such a thick base layer is needed as a stable foundation for the upper layers. The amount of soil for each layer was poured into the bin and levelled with a wooden leveller, as drawn in Figure 3.4. The wooden leveller was designed to fit the top edges of the soil bin as fixed marks, so that it slides over the edges to prepare an even layer surface, ensuring equal depth over the entire travel distance. For every top layer a different leveller was manufactured and used.

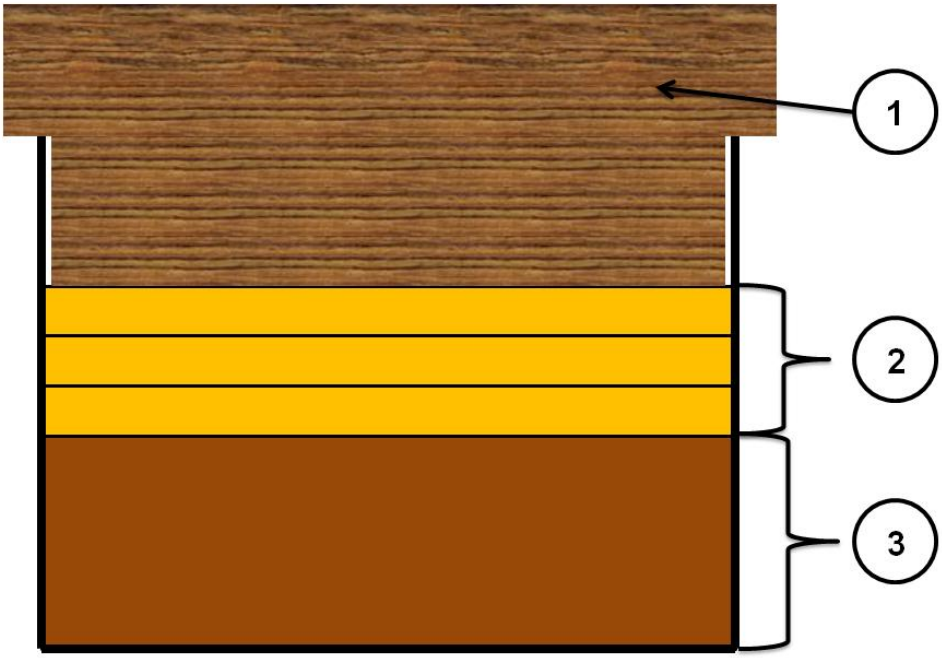

Figure 3.4: Soil profile in the soil bin including base layer (3) and top layers (2), with surface of top layer (2) levelled with wooden leveller (1).

After levelling the surface of a layer, this was compacted with a steel roller (17.6 kg) shown in Figure 3.5, which was hand rolled, due to the small size of the bin. For the smaller bulk density of 1450 kg m^{-3}, two rolls per layer were considered, whereas four rollers were applied for the higher bulk density of 1600 kg m^{-3}. After a run is completed the first six layers have to be removed and prepared again for the next run.

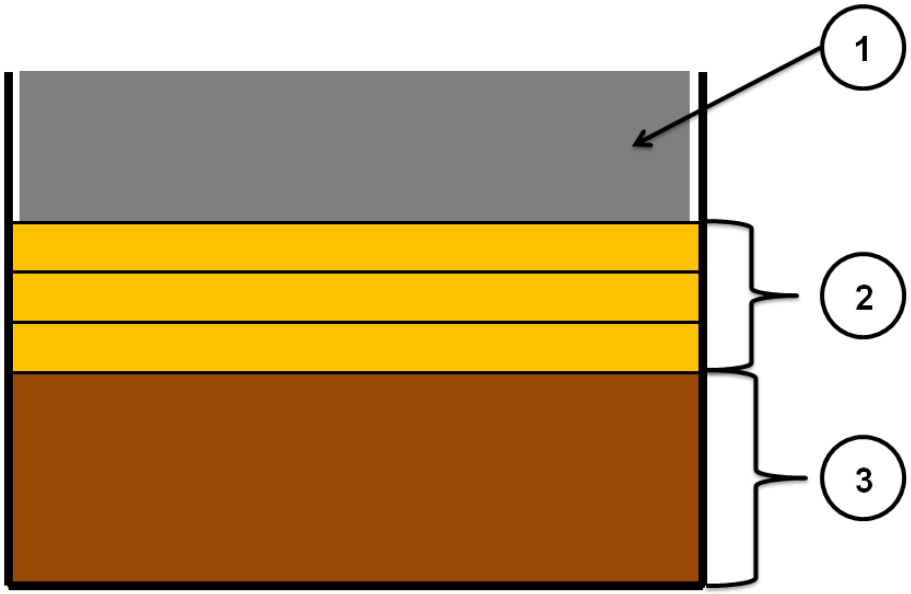

Figure 3.5: Soil profile in the soil bin including base layer (**3**), three top layers (**2**), subjected to vertical weight by a steel roller (**1**)

3.1.2 Measurement cycle

After soil in the soil bin was prepared to the desired height, the flexible tine (8) (Figure 3.6) was mounted on the axis (7) and screwed firmly to avoid the tine movement along this axis which might affect the measured forces. When this is done, the axis (7) was placed into the side plates (3 and 5), so that the small plate (4) could be screwed with side plate (3) to set-up the desired rake angle. The small plate has to be in contact with the side plate to position the flexible tine exactly in the middle. After that the lids (6) were screwed with the side plates (3 and 5). A hole was excavated in the soil bin, to avoid excessive soil disturbance, when placing the cradle over the soil bin. This also allowed for easier set up of the tine, to the desired working depth. The wall of the hole where the tine tip penetrates the soil was shaped as vertically as possible to ensure identical conditions to that with the FEM simulation.

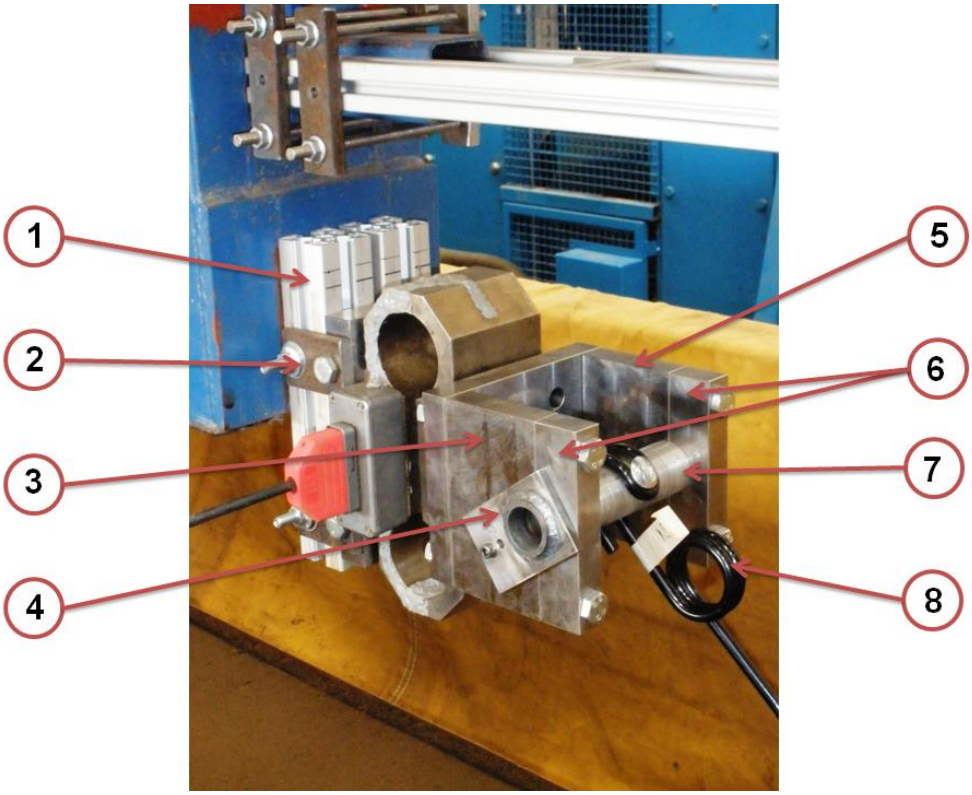

Figure 3.6: Adapter with different parts (**1**-Aluminium profile, **2**-Fixing plate, **3**/ **5**-Side plates, **4**-Small plate to adjust the working angle, **6**-Lid, **7**-Axis and **8**-Flexible tine)

The next step was the alignment of the string potentiometer aluminium frame to fix the strings (knotted and taped) with the tine, so that no movement on the tine was possible. Once the string potentiometers were connected with the tine the frame and the sensors could be aligned precisely, so that both strings created a right angle, as shown in Figure 3.7. After that, the hook of the cable winch had to be connected with the blue cradle of the wet soil bin. A ruler should be placed on the top of the soil bin to check the tine displacement[17] (around 20 cm) in the soil bin.

[17] The tine displacement was also checked with markers on the cable of the winch.

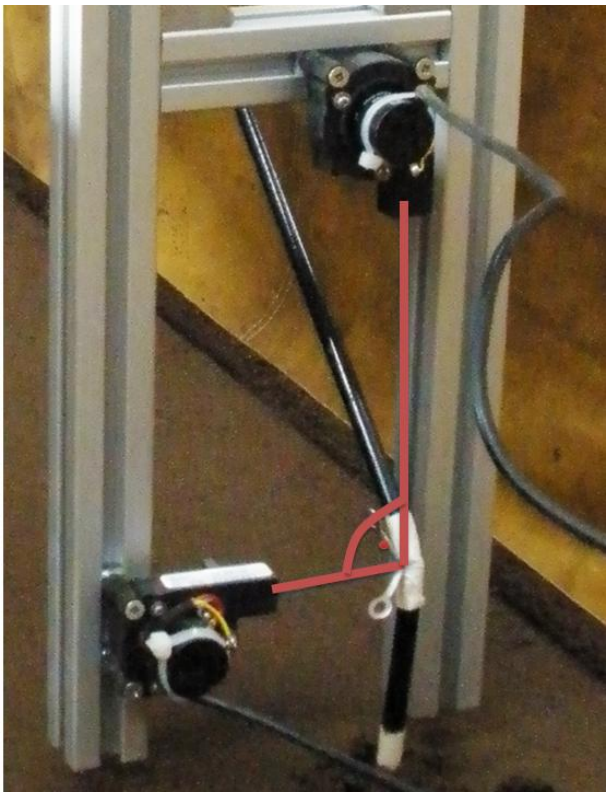

Figure 3.7: Arrangement of the string potentiometer on the flexible tine

After the desired settings were assigned in DasyLab, measurement was carried out. When a measurement cycle was completed, all the above-mentioned working steps had to be done in the reverse order until the flexible tine was removed, after which the first six soil layers had to be removed and re-prepared to start the next run.

3.2 Measurement of model parameters

The model material parameters needed as input for the FEM simulation were soil material parameters and soil-metal interaction properties. The soil material parameters were measured with a standard triaxial compression apparatus, whereas soil-metal interaction properties were measured with a modified direct

shear box. The material parameters for the flexible tine were obtained from the standard DIN EN 10270-1-SM[18] (Appendix A.1).

3.2.1 Triaxial compression test

The triaxial compression test[19] was used to measure the soil parameters, namely, Young's modulus, Poisson's ratio, cohesion, internal friction and the compression plasticity behaviour of the soil.

3.2.1.1 Theory

In the triaxial compression test a cylindrical soil specimen is loaded with a constant confining pressure (σ_3) in the radial direction, while in the axial direction the specimen is displaced for a distance equal to 25% of the specimen height, which causes principle stress (σ_1) in axial direction (Figure 3.8). Due to this stress combination, soil starts to fail, due to the increasing shear stress (τ) in the samples. This test is repeated for three chosen confining pressures (Figure 3.8). The output of this test is a graph of deviatoric stress (σ_1-σ_3) versus strain (ε). From this graph the Young's modulus can be calculated as the slope of the linear elastic part of the graph using the following equation, reported by Grote and Feldhusen [21]:

$$E = \frac{100 \times \Delta(\sigma_1 - \sigma_3)}{\Delta\varepsilon} \tag{3.1}$$

Where E is the Young's modulus [kPa], $\Delta(\sigma_1$-$\sigma_3)$ is the change in deviatoric pressure [kPa] and $\Delta\varepsilon$ is the change in elastic strain.

[18] This standard is the replacement of the old standard DIN 17223 B.
[19] The triaxial compression test is based on standard BS 1377-7: 1990.

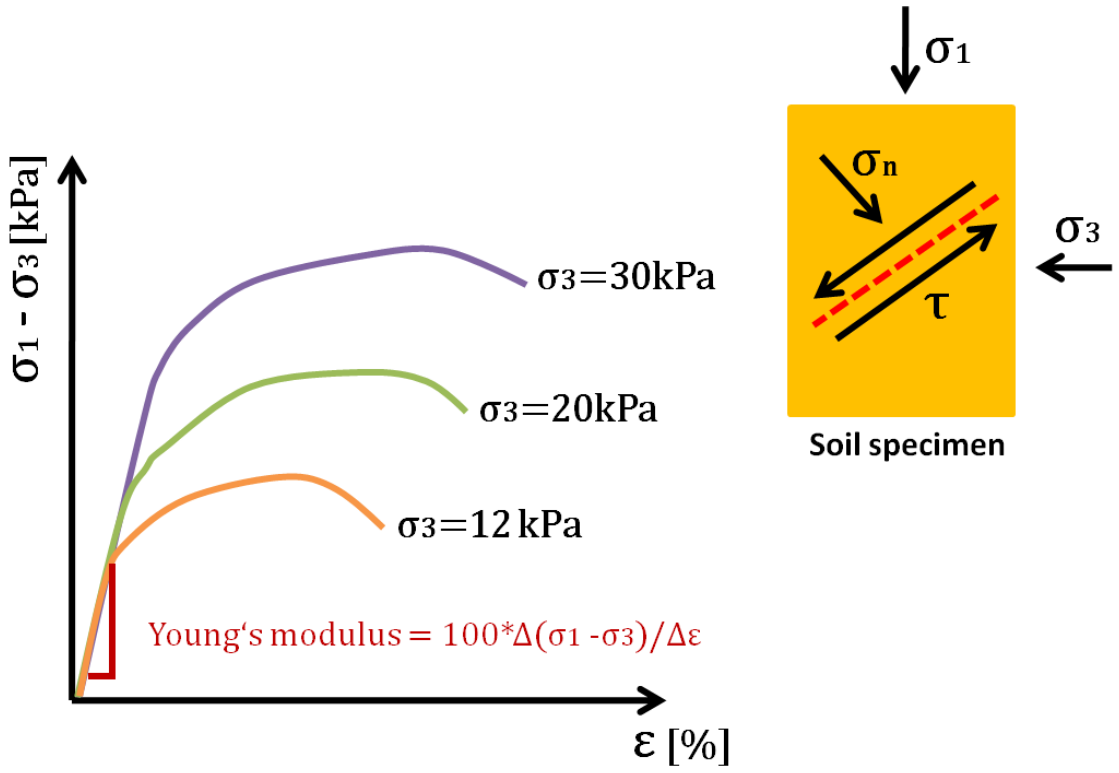

Figure 3.8: Schematic illustration of triaxial compression test results for three different confining pressures

The Poisson's ratio was calculated using the following equation (Grote et al. [21]):

$$\nu = \frac{\varepsilon_{1R} - \varepsilon_{2R}}{\varepsilon_{1A} - \varepsilon_{2A}} \tag{3.2}$$

Where ε_{1R} is the initial thickness of the specimen before the test (diameter of the specimen) [mm], ε_{2R} is the thickness after the test [mm], ε_{1A} is the initial length of the specimen before the test [mm] and ε_{2A} is the length after the test [mm]. The change in axial and radial strain is measured during the test, so that ε_{2R} and ε_{2A} can be determined. To draw the Mohr's circles the values of two principle stresses were needed to calculate the radius and the centre of the circles. In order to do this, the maximum deviatoric stress of each confining pressure was considered. The confining pressure σ_3 is the first point of the

circle close to y axis, whereas the second point (major principle stress σ_1 can be obtained when the confining pressure is added to the maximum deviatoric stress σ_d. The following equations explain the relation between Mohr's circle dimensions and the principle stresses (Fratta et al. [16]):

$$\sigma_1 = \sigma_d + \sigma_3 \tag{3.3}$$

The radius can be calculated as follows:

$$R_C = \frac{(\sigma_1 - \sigma_3)}{2} \tag{3.4}$$

and the centre of the circle is then:

$$M = \frac{(\sigma_1 + \sigma_3)}{2} \tag{3.5}$$

The circles for the different confining pressures are shown in Figure 3.9.

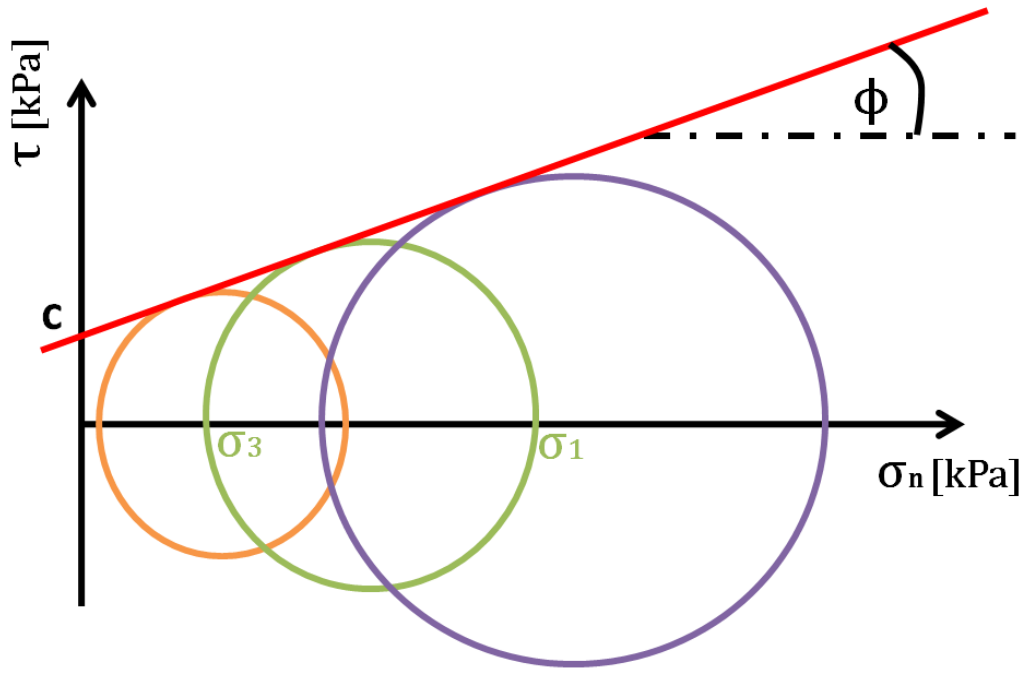

Figure 3.9: Tangent line of the Mohr's stress circles used to calculate the soil friction angle and cohesion

The tangent of Mohr's circle can be expressed by the Coulomb's equation (Fratta et al.[16]),

$$\tau = \sigma_n \times \tan\phi + c \tag{3.6}$$

Where c is soil cohesion [kPa], the interception point with the shear axis τ [kPa], σ_n is the normal stress [kPa] and tan(ϕ) is the friction coefficient, which represents the slope of the red tangent line.

Another soil behaviour, which can be measured with this test, is the plastic soil deformation under constant pressure, as mentioned in the Abaqus user manual [51]. In this case, the specimen in the triaxial compression test is loaded with increasing confining pressure. The resulted graph is similar to that shown in Figure 3.10, whereby the elastic part (ε_{el}) is usually much smaller. The data at the plastic part (ε_{pl}) are important for the material law (hardening) in the FEM simulation.

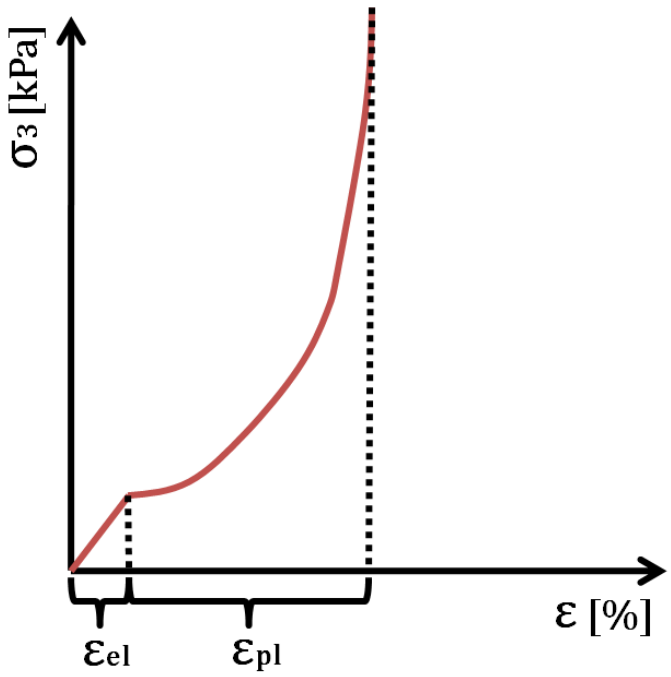

Figure 3.10: Schematic graph of a triaxial compression test with increasing confining pressure

3.2.1.2 Test set-up and test implementation

Error! Reference source not found. shows the test set-up of the triaxial compression test in the soil laboratory at Cranfield University. The test set-up consists of three parts; a computer (1), a pressure pump (2) and the triaxial compression chamber (3).

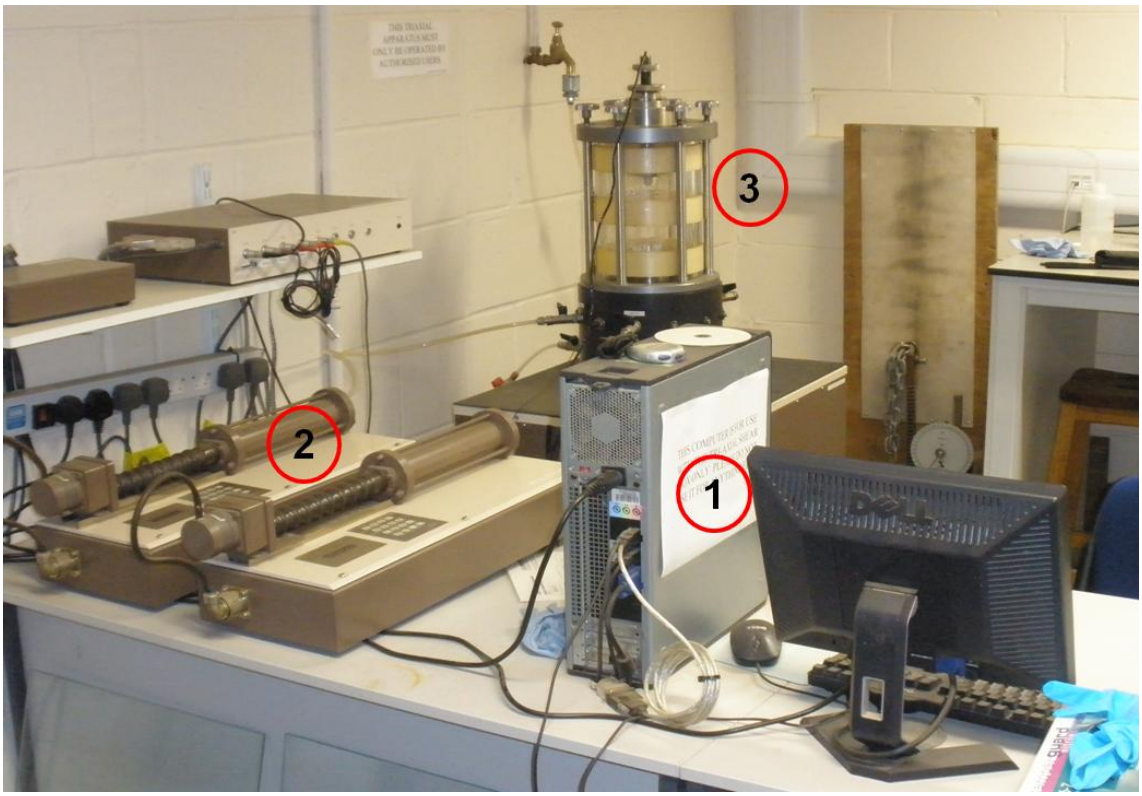

Figure 3.11: Overview of the triaxial compression test set-up (1-Computer, 2-Pressure pump and 3-Triaxial compression chamber)

The chamber represents the main part and can be seen in Figure 3.12. The soil specimen (yellow) is placed in the centre of the chamber. The soil specimen is a cylinder with 70 mm in diameter and 145 mm height, which is surrounded by a rubber membrane.

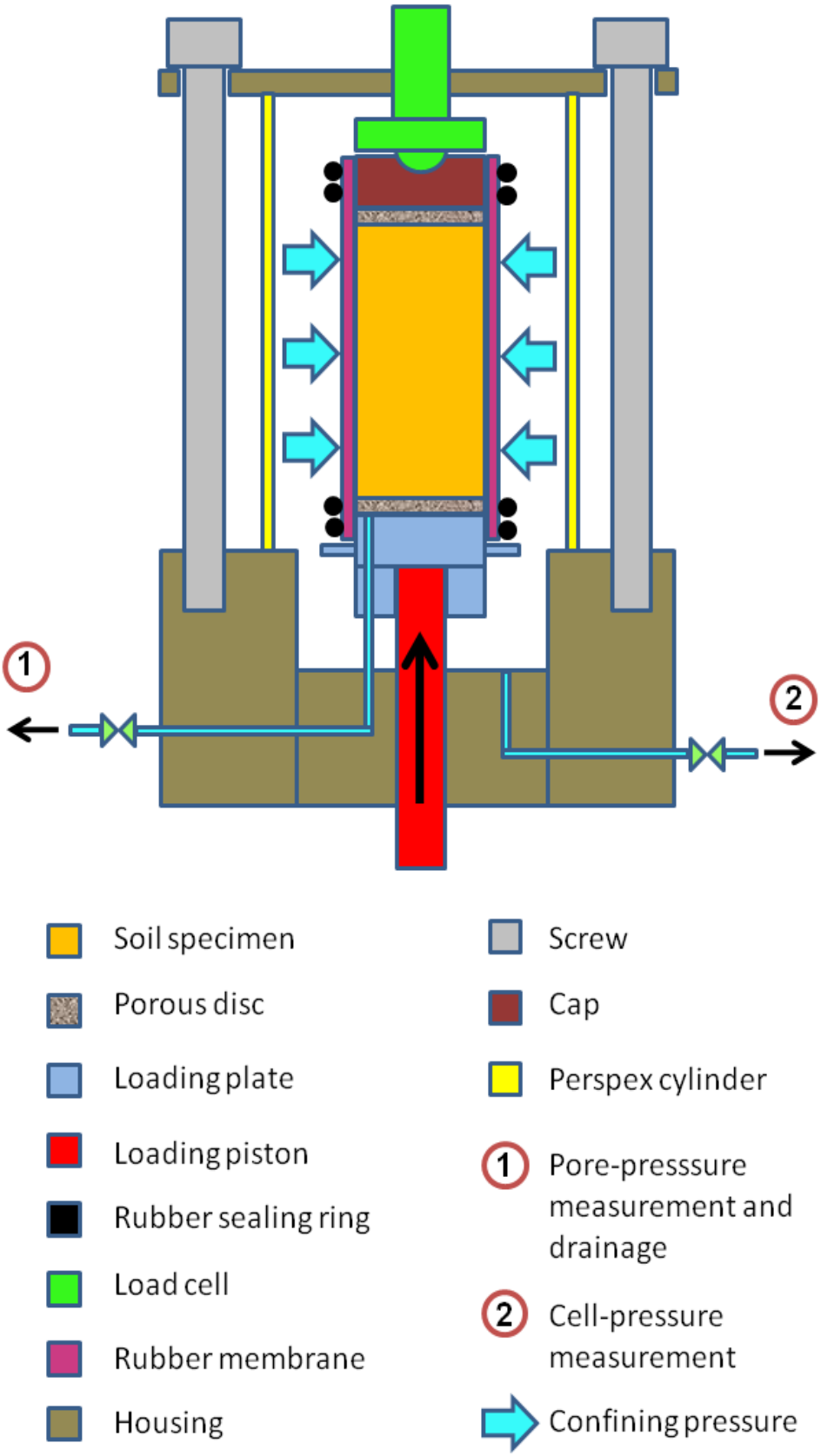

Figure 3.12: Schematic illustration of the triaxial compression chamber

In the rubber membrane, five layers of a thickness of 2.9 cm each, were prepared to ease filling and compaction. Each specimen was prepared to the same bulk density and moisture content, similar to those encountered during the soil bin tests. This was necessary to obtain actual soil parameters representative of the soil physical characteristics during the soil bin experiment. If this was not taken into account, soil mechanical properties measured with the triaxial compression will lead to undesired simulation error. Next, the chamber can be flooded with water. When this is done specific settings as dimension of the specimen, confining pressure, speed of the piston etc. have to be typed into the measurement programme and then the measurement could be started. Measurement with the triaxial compression test was divided into two stages, namely, first and second stage.

First test stage

The first stage is a static test stage, where the pump is building up the confining pressure (blue arrow) without moving the piston. Since mechanical weeding concerns the top soil layer, low confining pressures of 12, 20 and 30 kPa were adopted in this study (Figure 3.8). These values should be in the range encountered during the soil bin experiment. It was not possible to consider lower confining pressure than those adopted in this study, due to the limits of the triaxial compression apparatus[20].

To simulate the plastic behaviour of the soil, the first stage test was considered but with an increasing confining pressure up to 300 kPa. The required values, namely radial pressure and volumetric strain, were recorded by a computer with a specific software package for the triaxial compression test.

Second test stage

In the second test stage, the pump holds the confining pressure constant as set during the first test stage, while the piston is pressing the soil specimen with a speed of 1mm min^{-1}. After a piston displacement of 25% of the specimen height

[20] With a confining pressure less than 12kPa the measured data become instable.

has reached (36.25 mm), the second test stage is completed and so the sample is measured. Typical measured parameters in the second stage are the load, deviatoric stress, axial strain and radial strain history.

3.2.2 Modified direct shear box

The direct shear box test[21] was adopted to measure the interaction properties of soil-metal including the external friction between the flexible tine (metal) and the soil.

3.2.2.1 Theory

With the direct shear box test it is possible to measure the soil internal friction and cohesion, as well as the external friction, and the adhesion between different materials due to the set up flexibility of the test rig, shown by Swick et al. [54]. Furthermore, the values of constants for the Coulomb's equation can be directly measured and have not to be transformed into the van Mises stress plane, because in this case the normal stress σ_n and the shear stress τ respectively act vertically and horizontally in respect to the shear plane (Figure 3.13).

[21] The direct shear box test is based on standard BS 1377-7: 1990.

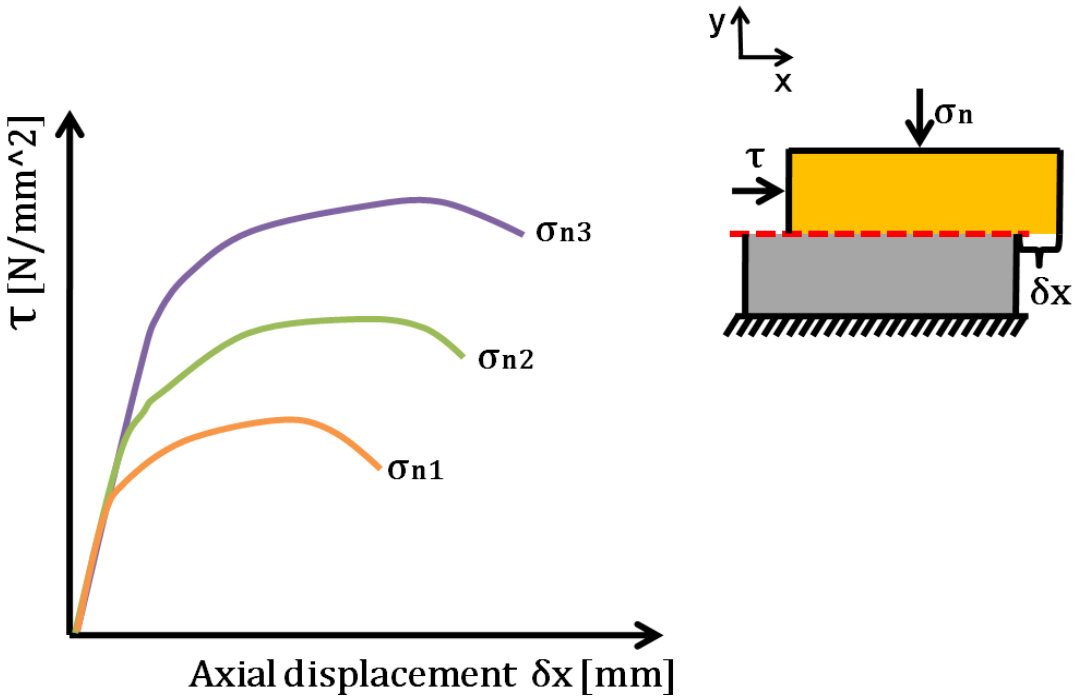

Figure 3.13: Direct shear box experiment and resulting graphs at three normal loads

The maximum shear stresses (τ) at three normal loads are recorded against the respective normal stresses (σ_n) plotted, as shown in Figure 3.14. The three data points are fitted with a linear regression line to allow the calculation of the adhesion and the external friction angle, as reported by Swick and Perumpral [54]. The equation for the regression line is the Coulomb's equation (3.6). The only difference to the triaxial compression test is that the interception point with the shear stress axis is now adhesion and the friction is now the external friction between metal and soil with friction angle φ.

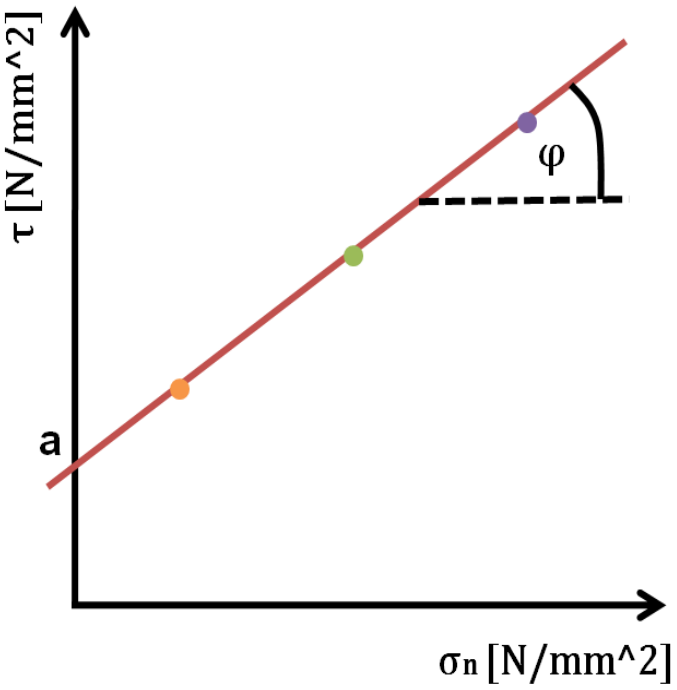

Figure 3.14: Regression line through three data points of maximum shear stress obtained from the direct shear box test

3.2.2.2 Test set-up and test implementation

Figure 3.15 shows the direct shear box test apparatus with shear box (1), gear box (2), normal load (3), dial indicators (4), computer (5), data logger (6) and load cell (7).

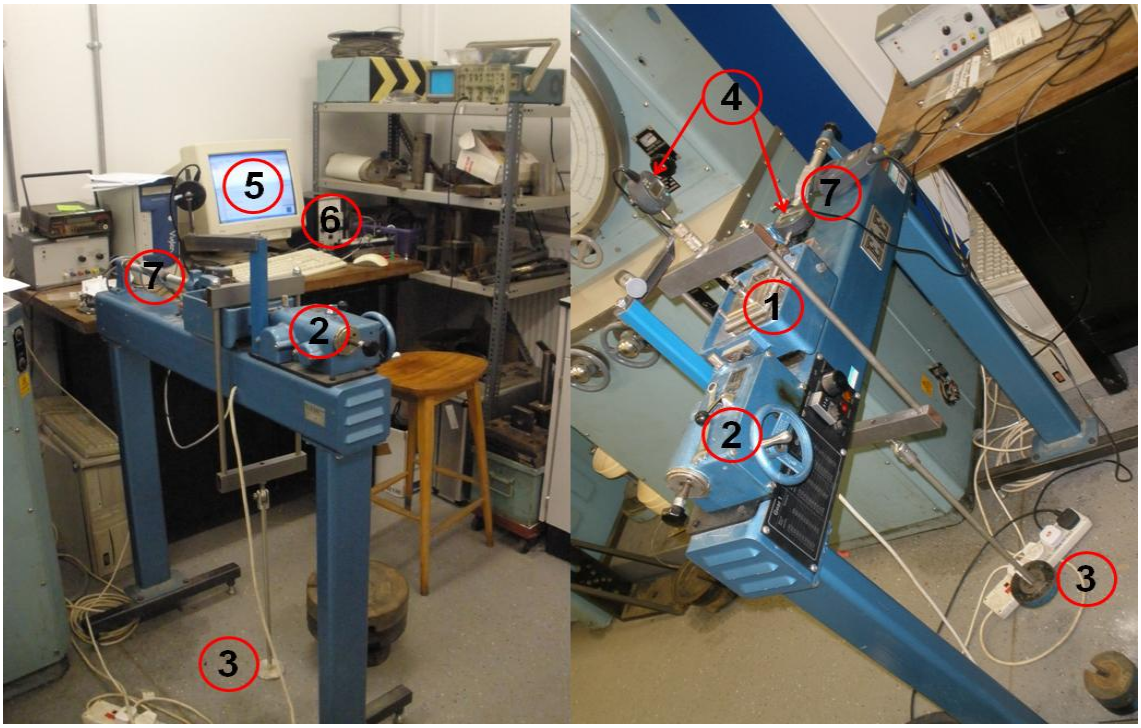

Figure 3.15: Overview of the direct shear box test set-up (**1**-Direct shear box, **2**-Gear box, **3**-Normal load, **4**-Digital dial indicators, **5**-Computer, **6**-Data logger, **7**-Load cell)

The shear box consists of two rigs of 60 mm by 60 mm by 15 mm dimension (Figure 3.16). The bottom rig has to be filled first with the metal plate (grey) instead of soil when soil-soil properties are used. Then the upper rig (yellow) is filled with soil. The same soil physical characteristics as those measured during the soil bin experiment were adopted for the soil in the upper rig, for the same reason as described for the triaxial compression test. For the preparation of the soil block in the upper rig, two layers of soil with a thickness of 5 mm each were separately added. This had the advantage that soil levelling and compaction can be easily monitored. Now the bottom rig had to be screwed with the housing (black) so that it is fixed in position. After that, both rigs were unscrewed and the top rig has to be lifted up for 1 mm to allow the soil block to slide over the metal plate. The next step is to place the normal loading on top of

the lid. Three different weights were used, namely, 4.50 kg, 7.31 kg and 11.01 kg, which are equal to the confining pressure in the triaxial compression test:

$$\sigma_n = \frac{11.01Kg \times 9.81\frac{m}{s^2}}{60mm \times 60mm} \tag{3.7}$$

$$\sigma_n = 30\frac{kN}{mm^2}$$

The numerator represents the normal load N acting on the shear plan (red dotted line in Figure 3.16) [16].

The 4.50 Kg was predetermined by the weight of load hanger and was thereby the lowest possible weight with the direct shear box test. Before the test, the vertical and horizontal displacements have to be set to zero. With the horizontal dial indicator the displacement δx of the upper rig is measured. During the test, the programme shows the shear force S [N] (measured by a load cell) versus the horizontal displacement δx. After a certain δx, a maximum peak in shear force will occur. This maximum is the point where both materials start to slide over each other. After this peak, the force decreases and the experiment can be terminated, as the maximum force recorded will be used to calculate the soil metal external friction.

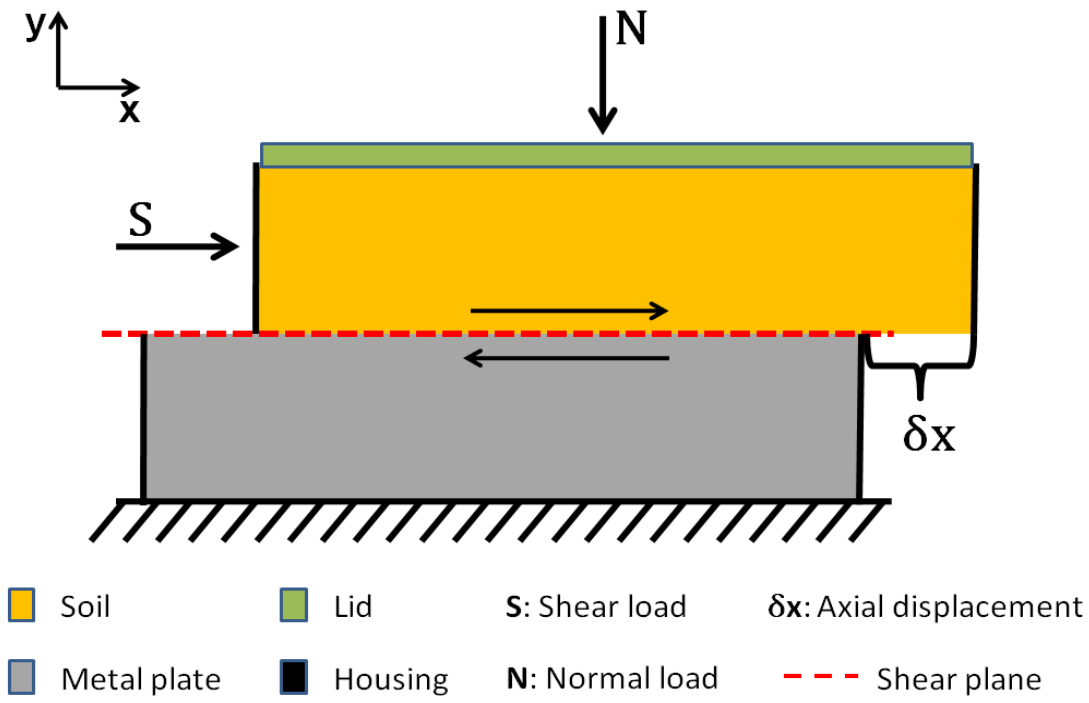

Figure 3.16: Basic parts assembly of the direct shear box and the acting forces

4 Finite element simulation

The finite element method (FEM) was used to simulate the soil-flexible tine interaction and to obtain detailed information about the tine and soil behaviour during the initial contact of mechanical weeding. The FEM is a computational technique used to obtain approximate solutions of boundary value problems, in which one or more dependent variables must satisfied a differential equation (Hutton [25]). The procedure for that, as explained by Zienkiewicz and Taylor [60], is the separation of the continuum into a number of elements. These elements are interconnected at a discrete number of nodal points situated on their boundaries. The displacement of the nodes, caused by external influences like forces, pressures etc., is the basic unknown parameter and will be calculated by a set of functions for each element node. These nodal displacement functions providing the strain at the elements, with regard of the material properties the state of stress on the elements and boundaries can be determined.

4.1 Simulation software

The used simulation software was Abaqus 6.9[22]. Many previous projects referred to this software for a wide area of applications, where soil is involved. There are two different ways to design a model in Abaqus. The first one is to write the programme code directly in an editor to create a text file, depending on the solver (implicit or explicit). The second possibility is to use an interface called Abaqus CAE, as shown in Figure 4.1. This user interface is similar to other commercial software and is more or less self-explanatory. In some cases different functions are not available in the CAE version but they can be inserted in the text file after it is generated by Abaqus CAE.

[22] This finite element software is provided by SIMULIA, USA further information at www.simulia.com.

For the current project, the CAE user interface was used to create the model. The main modules are the parts module, the material module, the section module, the assembly module, the step module, the interaction module and the constrains, load and boundary module. Description of different modules can be found in [51]. After the design of the model, a job file has to be created. This job file contains the whole programme code of the created model and can be sent to a computer. The model was created for an explicit solver as recommended in the Abaqus manual [51] for large deformations, which actually occurs in the soil during cutting with tines during the simulation. Furthermore, Abo-Elnor et al. [2] has also adopted large element distortion as a solution to achieve convergence when simulating the interaction between soil and a tine. At Cranfield University a cluster grid with 37 64bit Linux (4 quad Intel Xeon/ AMD Opteron processors) compute server was provided, each with 64 GB shared RAM. The job file was sent to the grid via a "*Secure Shell*" (SSH) client. The calculation time of the model was around three hours.

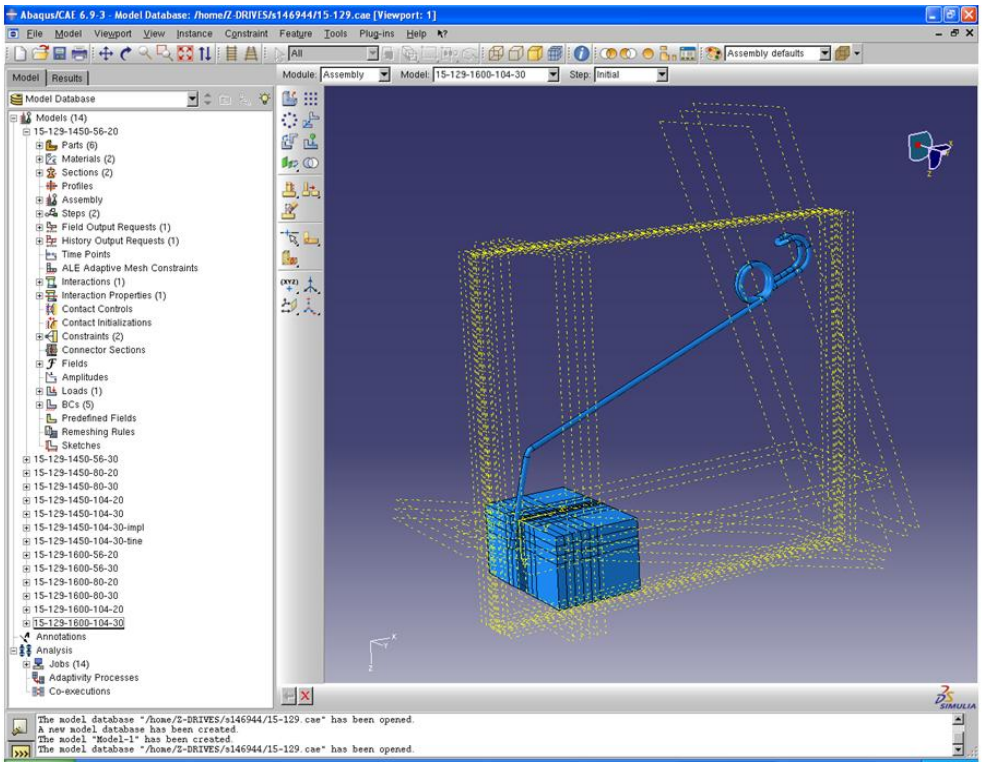

Figure 4.1: Abaqus CAE 6.9 user interface, showing the soil-tine 3-dimensional FEM model

4.2 Model description of the flexible tine

Three out of six different tines were simulated during this project, namely, 15-129, 15-228 and 15-054[23]. This selection was made due to time limitation of the project, in addition to small differences of the other tines, in comparison with those selected for simulation. The following procedures were generally identical for the three tines, hence these will be explained for one tine.

The tine was drawn in Autodesk Inventor Professional 2010[24] and later imported into Abaqus CAE as an IGES-file[25]. The tine model consists of five different parts, namely, tine leg (red), torsion spring (blue), wire 1 (yellow), loop (green) and wire 2 (purple) as shown in Figure 4.2.

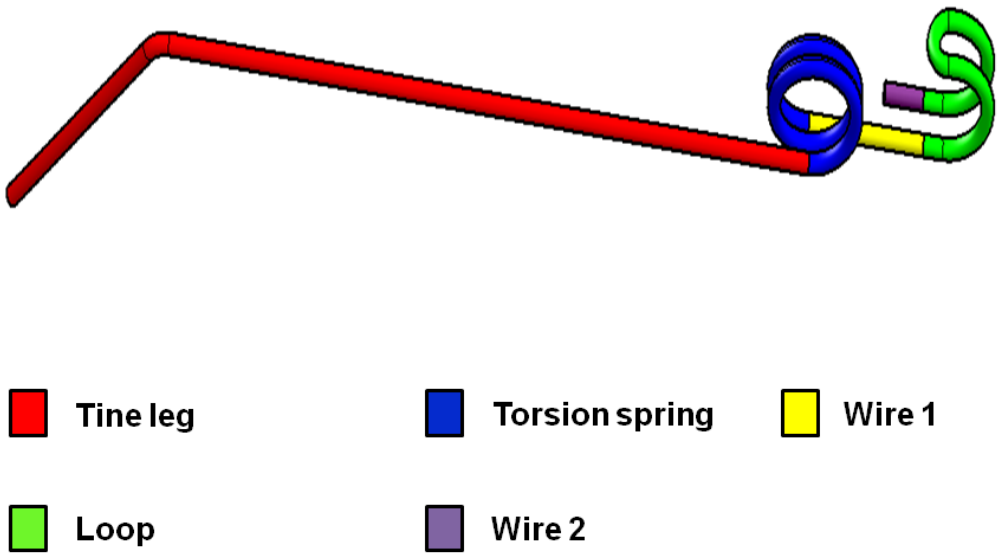

Figure 4.2: Parts of the flexible tine used for the FEM simulation

[23] Further information about these and the other tines are in section 2.2.2 and appendix A.1.
[24] Autodesk Inventor is a commercial available computer-aided design software provided by Autodesk Inc.
[25] One of the file extensions which were recommended in the Abaqus user manual [51]

4.2.1 Tine geometry

This section provides information about the different dimensions of the tines and working steps considered to create appropriate tine geometry for the FEM model. Table 4.1[26] summarises dimensions of the three tested tines. The respective legends for the dimensions are presented in Figure 4.3 and Figure 4.4.

Table 4.1: Dimensions of the three tines selected for FEM simulation

Dimension	Tine 15-129	Tine 15-228	Tine 15-054
A [mm]	490	490	600
B [mm]	36	36	36
C [mm]	49	56	50
D [mm]	20.2	30.1	21.1
E [mm]	100	120	115
F [°]	55	55	55
G [mm]	335	330	475
H [mm]	6.5	10	7
I [mm]	15	20	20
J [mm]	60	70	65
K [mm]	20	20	20
L [mm]	17	17	17
M [°]	10	10	10
N [mm]	10	10	10
O [mm]	22	29	23

[26] Further information about the tine geometry can be found in appendix A.1.

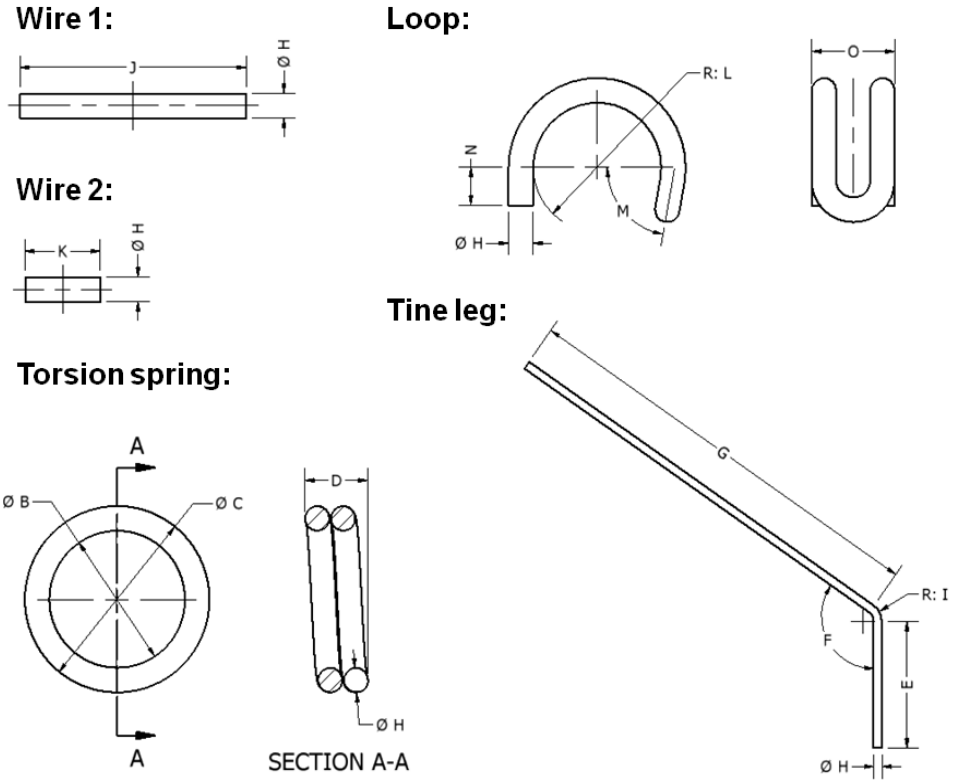

Figure 4.3: Dimensions of the five parts of simulated tines

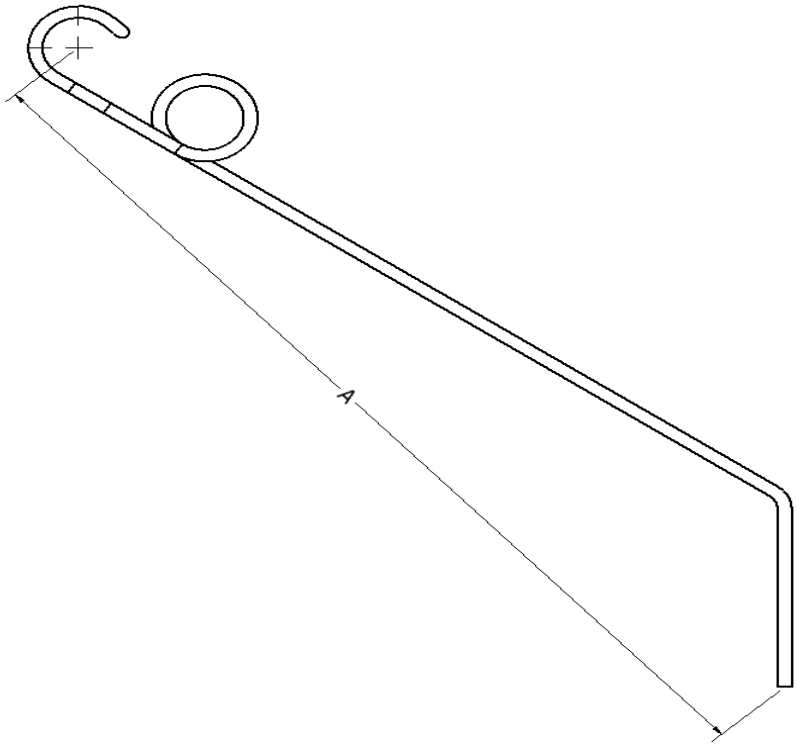

Figure 4.4: Overall length of the flexible tine

The dimensions of tine parts were assigned as SI-units. Since Abaqus software does not recognise units, the user has to choose appropriate units representing the actual tine dimensions, which has to be kept the same in all modules. All different tine components are placed in the parts module and can be separately selected from the model tree. Due to the bent shape of different components, especially the torsion spring and the loop, the tine parts had to be partitioned to ensure a good geometry that can be meshed properly during the meshing procedure. The different parts were assembled together using the assembly module to obtain the entire tine geometry. Therefore, the parts were aligned and connected with tie elements, to ensure the nodes at the contact surfaces cannot move relatively to each other, which might result in the tine behaving as solid body. To ensure the bending behaviour between the real tine and the modelled tine is identical, static bending tests were investigated. For that the tine was mounted on the adapter, so that different loads could be placed on the tine tip in vertical and lateral directions. The deflection of the tine tip was then measured with a calliper and string potentiometer. The angle of deflection was also measured with an angle meter. Both bending directions showed a very good correlation with simulation.

4.2.2 Tine material

The flexible tine consists of spring steel based on the standard DIN EN 10270–1–SM[27], so that the material properties could be found in material tables [35]. Table 4.2 summarises the material parameters, which were used for the FEM simulation.

[27] This standard is the replacement of standard DIN 17223 B.

Table 4.2: Material parameters of the flexible tine used for the FEM simulation

Flexible tine material parameters	
Density ρ [Kg m^{-3}]	7850
Young's modulus E [N m^{-2}]	208.5 x10^{9}
Poisson's ratio ν [-]	0.297

Due to the material and its characteristic a linear elastic isotropic material law was used for the flexible tines in the FEM model, which is based on Hooke's law of linear relationship between stress and strain. The linearity factor is given by the Young's modulus of elasticity (Figure 4.5), representing the stiffness of the material. This assumption is accurate for small strains so that the material will only be elastically deformed and retain the initial structure after loading (Becker and Gross [7]). Due to this theory it is possible to describe the material of the tine with the following equation according to Hook's law [21]:

$$\sigma = E \times \varepsilon \tag{4.1}$$

Where σ is the normal stress [N mm^{-2}] in an uniaxial tension test, E is the Young's modulus [N mm^{-2}] and ε the axial strain [-]. Equation (4.1) shows the relation for a uniaxial tension test (Figure 4.5) under specific symmetry assumptions, which have to be made due to the complex determination of 81 elasticity moduli in a general elasticity material model. The variables σ, ε and E can be expressed in the three dimensional space with the following equation [51]:

$$\begin{pmatrix}\sigma_{11}\\ \sigma_{22}\\ \sigma_{33}\\ \sigma_{23}\\ \sigma_{31}\\ \sigma_{12}\end{pmatrix} = \begin{bmatrix} E_{11} & \frac{-E_{22}}{\nu_{21}} & \frac{-E_{33}}{\nu_{31}} & & & \\ \frac{-E_{11}}{\nu_{12}} & E_{22} & \frac{-E_{33}}{\nu_{32}} & 0\ 0\ 0 & & \\ \frac{-E_{11}}{\nu_{13}} & \frac{-E_{22}}{\nu_{23}} & E_{33} & 0\ 0\ 0 & & \\ & 0\ 0\ 0 & & & G_{23}\ 0\ 0 & \\ & 0\ 0\ 0 & & & 0\ G_{31}\ 0 & \\ & 0\ 0\ 0 & & & 0\ 0\ G_{12} \end{bmatrix} \times \begin{pmatrix}\varepsilon_{11}\\ \varepsilon_{22}\\ \varepsilon_{33}\\ \gamma_{23}\\ \gamma_{31}\\ \gamma_{12}\end{pmatrix} \tag{4.2}$$

The Poisson's ratio is represented by the variable ν_{ij} [-] and is the ratio of length change in all three directions relative to the initial length of a body. This change in length is causes by transverse contraction of a tension loaded body. Variable G_{ij} represents the shear modulus [N mm^{-2}] and can be expressed by the Young's modulus E [N mm^{-2}] and Poisson's ratio ν [-] with the following equation [21]:

$$G = \frac{E}{2 \times (1 + \nu)} \tag{4.3}$$

The variable γ_{ij} is the shear strain [-] and is linked with the shear modulus. The tine material was assumed to be isotropic, which means that the behaviour of the material is equal in all directions and is direction independent. With inserting equation (4.3) and transposing equation (4.2) the final material law can be written as [51]:

$$\begin{pmatrix}\varepsilon_{11}\\ \varepsilon_{22}\\ \varepsilon_{33}\\ \gamma_{23}\\ \gamma_{31}\\ \gamma_{12}\end{pmatrix} = \begin{bmatrix} \frac{1}{E} & \frac{-\nu}{E} & \frac{-\nu}{E} & & & \\ \frac{-\nu}{E} & \frac{1}{E} & \frac{-\nu}{E} & 0\ 0\ 0 & & \\ \frac{-\nu}{E} & \frac{-\nu}{E} & \frac{1}{E} & 0\ 0\ 0 & & \\ & 0\ 0\ 0 & & \frac{2 \times (1+\nu)E}{E} & 0 & 0 \\ & 0\ 0\ 0 & & 0 & \frac{2 \times (1+\nu)}{E} & 0 \\ & 0\ 0\ 0 & & 0 & 0 & \frac{2 \times (1+\nu)}{E} \end{bmatrix} \times \begin{pmatrix}\sigma_{11}\\ \sigma_{22}\\ \sigma_{33}\\ \sigma_{23}\\ \sigma_{31}\\ \sigma_{12}\end{pmatrix} \tag{4.4}$$

Equation (4.4) represents the law for an isotropic linear elastic material and it depends only on the engineering material parameters, namely, E and ν, which can be easily determined with a tensile test as shown in Figure 4.5.

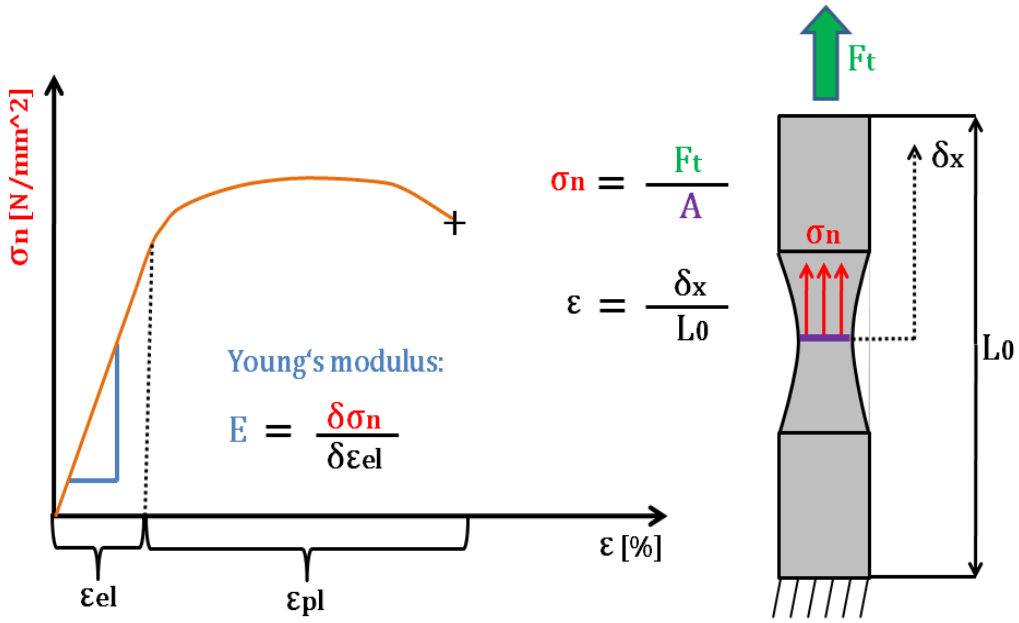

σn: Normal stress | **Ft:** Tension | **A:** Cross-section area
ε: Axial strain | **εel:** Elastic strain | **εpl:** Plastic strain
L0: Initial specimen length | **δx:** Displacement | **+:** Failure

Figure 4.5: Uniaxial tension test and graph with the linear relation between normal stress and strain (Hooke's law)

4.2.3 Mesh of tine

The tine was modelled as a three dimensional solid body, so that linear hexahedral elements of C3D8R[28] type were used for mesh generation. This element type is a stress/ displacement element, and can be used for nonlinear mechanical analysis that involves contact, plasticity and / or large deformations [51]. It has three degrees of freedom (translational DOFs), allowing displacement in three directions without rotation, which was necessary to

[28] Three-dimensional solid element as 8-node brick with reduced integration and hourglass control.

simulate tine movement in all three directions and to model the nonlinear soil metal contact. Due to the torsion spring, the tine could not be modelled as a rigid body, because the elements and nodes in different parts can move relative to each other, so that their relative position was not constant throughout the entire simulation. A further advantage of this element type is less discretisation errors than tetrahedral elements, due to linear strain variation with displacement and the reaction to application of body loads, reflects better real world conditions. Due to higher order elements, it is with a better accuracy with negligible increase in computational costs [6]. Due to the reduced integration, the calculation is fast, where shear and volume blocking can be avoided. The hourglass control ensures a stable element structure [43].

Draught and the tine tip movement in all three directions are the expected output of FEM modelling in this project, for which the C3D8R elements were found appropriate. Due to the shape of the tine, the mesh was manually designed to create a good transition region between the parts. Pre-calculations were done to achieve the best mesh set-up in relation to computational costs and accuracy of the results. The number of elements and nodes are presented in Table 4.3.

Table 4.3: Number of nodes and elements used for the three tines

Mesh compilation of the flexible tines						
	Tine 15-129		**Tine 15-228**		**Tine 15-054**	
Parts	**Elements**	**Nodes**	**Elements**	**Nodes**	**Elements**	**Nodes**
Tine leg	1568	2075	1472	1952	1888	2485

Torsion spring	8128	10480	8320	10726	7680	9906
Wire 1	1792	2362	1920	2526	1792	2362
Loop	4544	5888	3328	4330	4320	5601
Wire 2	819	1146	960	1296	576	804
Total	16851	21951	1600	20494	16256	21158

4.3 Model description of the soil

Soil is a very complex medium. In comparison with other engineering materials the soil structure is highly inhomogeneous and consists of different components, namely solid, water and air. That makes accounting for different phases during soil modelling and calculations largely complicated. The next sections explain how this complex material was modelled in Abaqus CAE.

4.3.1 Geometry of soil model

The soil was designed as a prismatic block, which was partitioned as shown in Figure 4.6. Therefore, five layers were inserted in x-direction, three layers in z-direction and eleven layers in y-direction. The partition planes in y-direction were determined as a multiple of each tine wire diameter. The geometry data of the soil and the position values for each layer are summarised in Table 4.4.

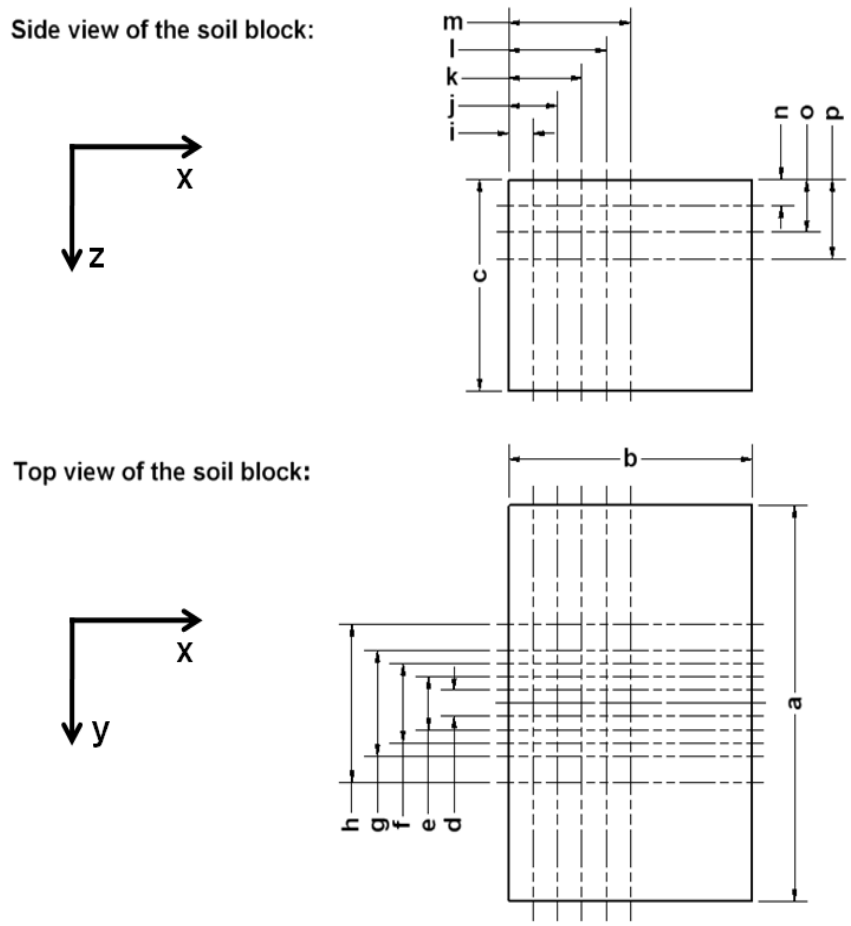

Figure 4.6: Soil block size and position of the partitition planes

Table 4.4: Dimension of the soil block and position data of the partition planes

Soil block geometry and partition data			
Length [mm]	**Soil block: Tine 15-129**	**Soil block: Tine 15-228**	**Soil block: Tine 15-054**
A	150	150	150
B	100	100	100
C	80	80	80
D	6.5	10	7

E	13	20	14
F	20	30	28
G	40	40	42
H	60	60	60
I	10	10	10
J	20	20	20
K	30	30	30
L	40	40	40
M	50	50	50
N	10	10	10
O	20	20	20
P	30	30	30

4.3.2 Soil material

Abaqus software provides several material models, which are suitable for cohesive geological materials that exhibit pressure dependent yield, such as soils. In this work, the modified Drucker-Prager/ Cap model was used. The advantage to the standard Drucker-Prager plasticity model is that the modified material law takes soil softening and hardening into account. Furthermore, this model considers the effect of stress history, stress path, dilatancy and the effect of the intermediate principle stress [22]. Figure 4.7 shows the different parts of this material model and the relation between each other.

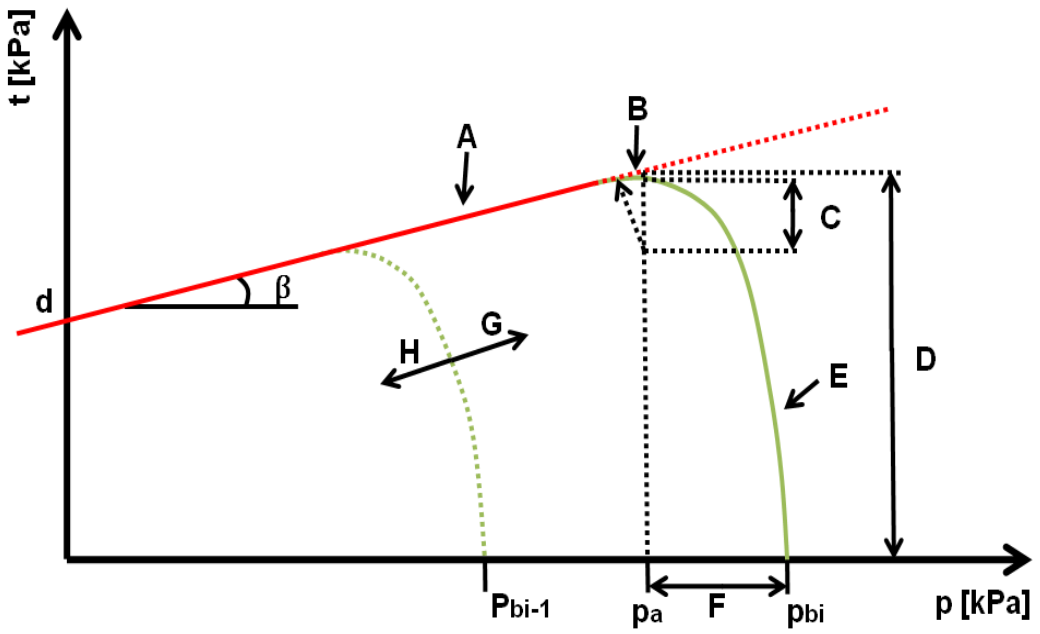

A: Shear failure, Fs **B:** Transmition surface, Ft **C:** α*(d+pa*tan(β)) **D:** d+pa*tan(β)
E: Cap, Fc **F:** R* (d+pa*tan(β)) **G:** Hardening **H:** Softening
β: Friction angle **d:** Cohesion

Figure 4.7: Schematic overview of the modified Drucker-Prager material model

The modified Drucker-Prager material model is arranged in the p-t plane and can be described by the following equations as described in the Abaqus user manual [51].

$$p = \frac{(\sigma_{11} + \sigma_{22} + \sigma_{33})}{3} \tag{4.5}$$

Where p is the mean effective stress [kPa] and σ_{11}, σ_{22} and σ_{33} are the principle stresses [kPa]. The following equation describes the shear stress t [kPa],

$$t = \frac{q}{2} \times \left[1 + \frac{1}{K} - \left(1 - \frac{1}{K}\right) \times \left(\frac{r}{q}\right)^3\right] \tag{4.6}$$

Where the variable q is the Mises equivalent stress [kPa],

$$q = \sqrt{\frac{3}{2} \times (S{:}S)} \tag{4.7}$$

r represents the third invariant of deviatoric stress [kPa],

$$r = \left(\frac{9}{2} \times S \cdot S{:}S\right)^{\frac{1}{3}} \tag{4.8}$$

where S is the stress deviator [kPa] and K is the ratio of the yield stress [-] in triaxial tension to the yield stress in triaxial compression. For a more detailed explanation about the stress plane and related mathematical equations, the following book by Helmany [22] and the Abaqus online documentation [51] are suggested. The material model is divided into three parts, namely, the Drucker-Prager shear failure surface Fs (A), a smooth transition surface Ft (B) and the elliptical cap surface Fc (E), which intersects the p-axis at a right angle. The linear elastic behaviour is also based on the Hooke's law explained in section 4.2.2 by equation (4.1). It is worth mentioning that the linear elastic phase in soil is relatively small, especially in comparison with materials like steel.

The shear failure can be written according to Coulomb's law as:

$$F_s = t = p \times \tan(\beta) - \mathrm{d} \tag{4.9}$$

Where t is the shear stress [kPa] and p is the mean effective stress [kPa]. The tangent and intercept of this linear function with the shear stress axis, represent the soil cohesion d [kPa] and friction angle β [°], respectively, as described in section 3.2.1. Both parameters have to be converted from the Mohr-Coulomb failure criterion into the Drucker-Prager failure criterion with the following equations, respectively:

$$\beta = \tan^{-1}\left(\frac{6 \times \sin\phi}{3 - \sin\phi}\right) \tag{4.10}$$

$$d = \frac{18 \times c \times \cos\phi}{3 - \sin\phi} \tag{4.11}$$

Whereby, ϕ [°] and c [kPa] are the soil friction angle and cohesion in the Mohr-Coulomb failure criterion.

The next part is the Cap yield surface (E), which can be described by the following equation:

$$F_c = \sqrt{(p - p_a)^2 + \left(\frac{R \times t}{1 - \alpha - \frac{\alpha}{\cos\beta}}\right)^2} - R \times (d + p_a \times \tan\beta) = 0 \quad (4.12)$$

Where α is a number [-], typically between 0.1 and 0.5, to define the transition yield surface and p_a is an evolution parameter [kPa] and can be calculated as:

$$p_a = \frac{p_b - R \times d}{(1 + R \times \tan\beta)} \quad (4.13)$$

The variable p_b is the hydrostatic compression yield stress [kPa] and R is a material parameter [-], which controls the shape of the cap and has to be between 0.0001 and 1000. Due to its wide range, R must be approximately but carefully determined as it can influence the simulation results significantly. To do this a hydrostatic compression test for both bulk densities was done to obtain the plastic strain curve, which is shown schematically in Figure 4.8 and the results are summarised in Table A.4.1.

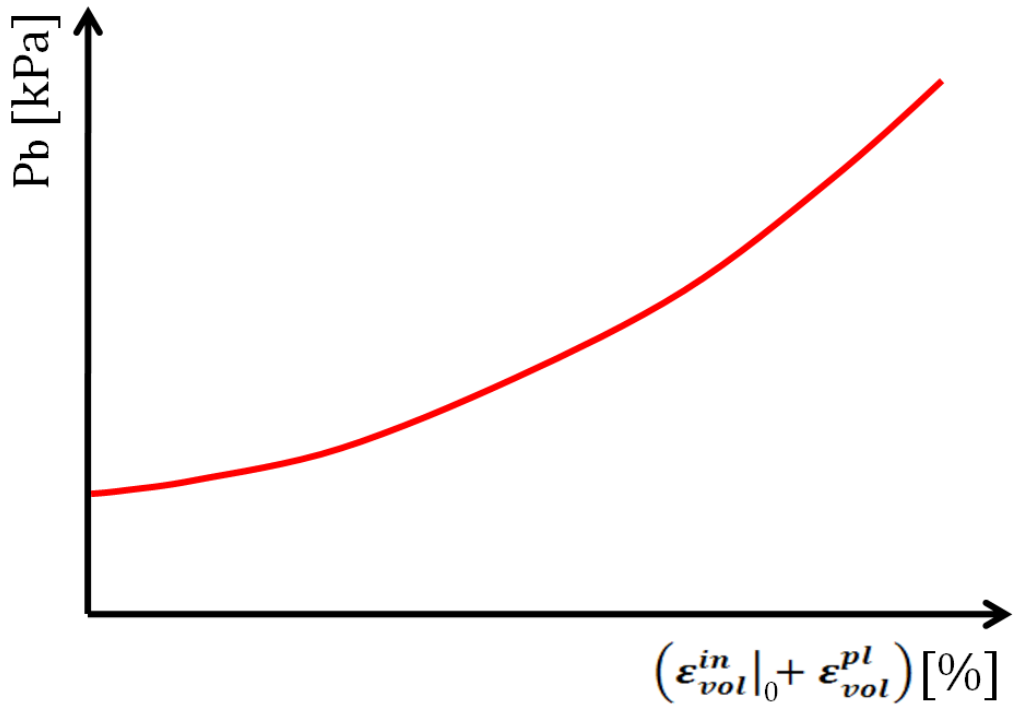

Figure 4.8: Schematic illustration of the plastic soil behaviour during hydrostatic compression test

The plotted strain is the plastic volumetric strain where ε_{vol}^{in} is the initial point of plastic strain [%] (represents the initial yield surface position in the material model) and ε_{vol}^{pl} are the volumetric plastic strain [%]. The hydrostatic compression results were obtained with the triaxial compression test in the first stage where the soil specimen is loaded with an increasing confining pressure as explained in section 3.2.1. R is a material parameter of a constant value for a specific material. If equation (4.13) is substituted into equation (4.12) the following formula can be obtained:

$$F_c = \sqrt{\left(p - \frac{p_b - R \times d}{(1 + R \times \tan\beta)}\right)^2 + \left(\frac{R \times t}{1 - \alpha - \frac{\alpha}{\cos\beta}}\right)^2} - R \times \left(d + \frac{p_b - R \times d}{(1 + R \times \tan\beta)} \times \tan\beta\right) = 0 \quad (4.14)$$

The value p_b is the intersection point of the cap yield surface with the effective mean stress axis as shown in Figure 4.7, which means at this point no shear stress occurs (t=0 due to hydrostatic compression). The cap surface can move along the horizontal stress axis. The direction of moving depends on the stress state. When the stress state causes yielding on the cap surface, compaction occurs, which results in the surface expanding (hardening). But, when the stress state causes yielding on the Drucker-Prager shear failure surface, dilation occurs, which results in the cap surface to shrink (softening). With this knowledge equation (4.14) can be simplified to:

$$F_c = \left(p_b - \frac{p_b - R \times d}{(1 + R \times \tan\beta)}\right) - R \times \left(d + \frac{p_b - R \times d}{(1 + R \times \tan\beta)} \times \tan\beta\right) = 0 \quad (4.15)$$

In this equation the only unknown parameter is R depending on p_b. To solve this eqution an approximate calculation was done. The best value for R must come as close as possible to zero for every p_b to fullfil equation (4.15) as presented by Hofer et al. [23].

The third part is the transition yield surface (B), which should provide a smooth connection between the Drucker-Prager shear failure surface and the cap yielding surface. In Table 4.5 the soil material parameters used for the FEM simulation model are summarised.

Table 4.5: Soil material parameters used for the FEM simulation model

Soil material parameters		
	Soil I	**Soil II**
Density ρ [Kg m^{-3}]	1450	1600
Young's modulus E [N m^{-2}]	2212000	3701000
Poisson's ratio ν [-]	0.299	0.299
Cohesion d [Pa]	12995	19686
Internal friction angle β [°]	13.78	25.49
Cap eccentricity R [-]	0.58	0.03
Initial yield surface position ε_{vol}^{in} [-]	0	0
Alpha α [°]	0.02	0.02
Flow stress ratio K [-]	1	1

4.3.3 Mesh of soil body

The soil was also considered as a solid body and modelled with the same elements (C3D8R) as the flexible tine (Section 4.2.3). Soil disturbance in x-,y- and z-direction was the desired output. Due to the three degrees of translational freedom (DOF) of this element type it was possible to simulate the soil displacement in all three directions. For the soil block, an automatic mesh creator was used in the Abaqus part module. Pre-calculations were done to achieve the best mesh set-up in relation to the computational costs and accuracy of the results. Table 4.6 provides an overview of the number of elements and nodes used for the three soil blocks in front of the three flexible tines simulated in this study.

Table 4.6: Number of nodes and elements for the three soil blocks

Mesh compilation of the soil blocks						
	Soil block: Tine 15-129		Soil block: Tine 15-228		Soil block: Tine 15-054	
Part	**Elements**	**Nodes**	**Elements**	**Nodes**	**Elements**	**Nodes**
Soil	10240	11781	9600	11067	9600	11067

4.4 Boundary conditions and loading

The soil was constrained on different outer sides of the block and the tine was loaded and constrained on the loop, as shown in Figure 4.9.

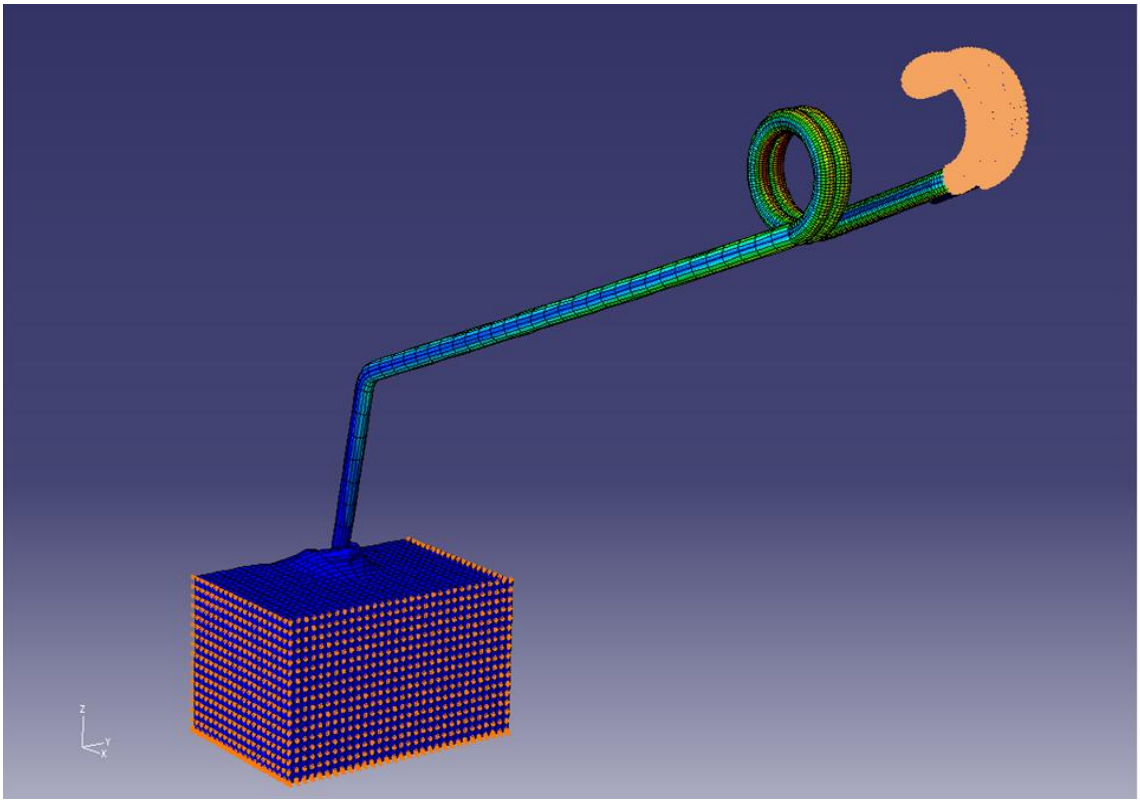

Figure 4.9: Boundary conditions of the soil block and the flexible tine

The nodes in the side planes AEHD and BFGC were constrained in y-direction, the backplane EFGH was fixed in x-direction and the bottom plane CGHD was constrained in all directions (see Figure 4.10). These constraints were assigned to simulate the reality, where the soil block is surrounded by soil, so that the soil particles in these planes could not move in the constrained directions. The top plane ABFE was left free without any constraints because on the top surface the soil particles can move in all directions. The ABCD front plan was also not constrained to move and to allow for soil deformation. These assumptions were made by Mouazen [39], who studied the interaction between soil and a medium deep subsoiler using the FEM.

The tine was loaded with a velocity applied on the loop. Due to the fact that the tine is usually screwed on an axis where it cannot move vertically (z-direction) and laterally (y-direction), the speed was only in the direction of travel (x-direction), which was constrained for y-, and z-directions. A working speed of 0.5 m s^{-1} and a simulation time 0.1 s were implemented, which resulted in an overall tine displacement of 5 cm. In comparison with the soil bin test, the speed was marginally higher in FEM simulation. Calculations with a lower working speed were investigated, and results proved that these marginal speed differences have not affected the results. Simulation with a higher speed led to significant reduction in the computational time. The gravitational force was also applied on both the soil and tine.

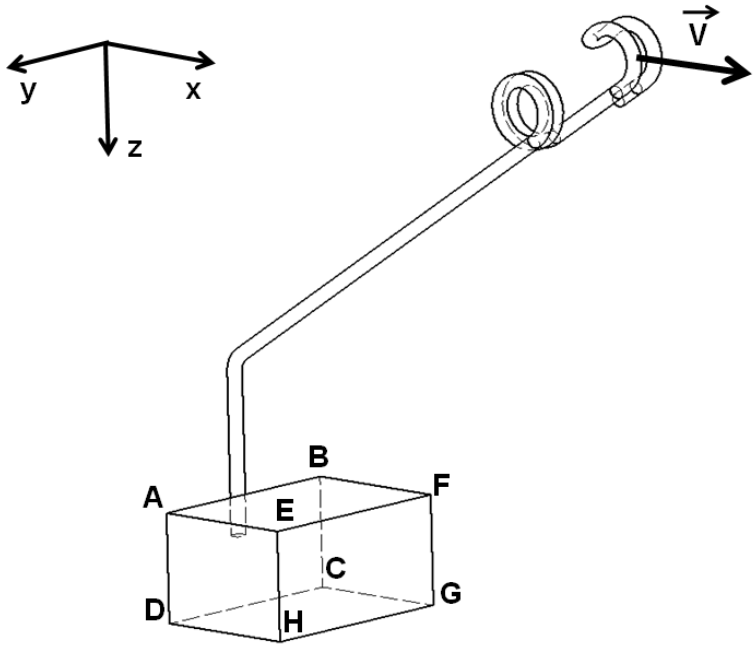

Figure 4.10: Schematic illustration of the outer planes of a soil block and the tine loading in the travel direction

4.5 Soil-metal interaction

The interaction layer between the tine and soil presents another important part in the model, and has to be taken into account. There are two different ways described in the literature to connect the metal part of the tine with the soil. Mouazen et al. [39], Gee-Clough et al. [18] and Chi et al. [9, 10] used 2-D rigid connector elements to connect opposite nodes of the tool and the soil block. When these elements were used in the current study, problems associated with the completely free movement of the tine tip arose, so that the connected nodes were pulled out of the soil due to the upward movement of the tine tip, which does not represent the reality, and introduced large errors. That is the reason why a second method proposed by Abo-Elnor et al. [1], Plouffe et al. [45] and Jafari et al. [26] was used. In this method, contact surfaces (a master and slave surfaces) could be created, which is a feature supported by Abaqus. Therefore

a master surface (tine leg, red) and a slave surface (soil block, pink) were defined as shown in Figure 4.11.

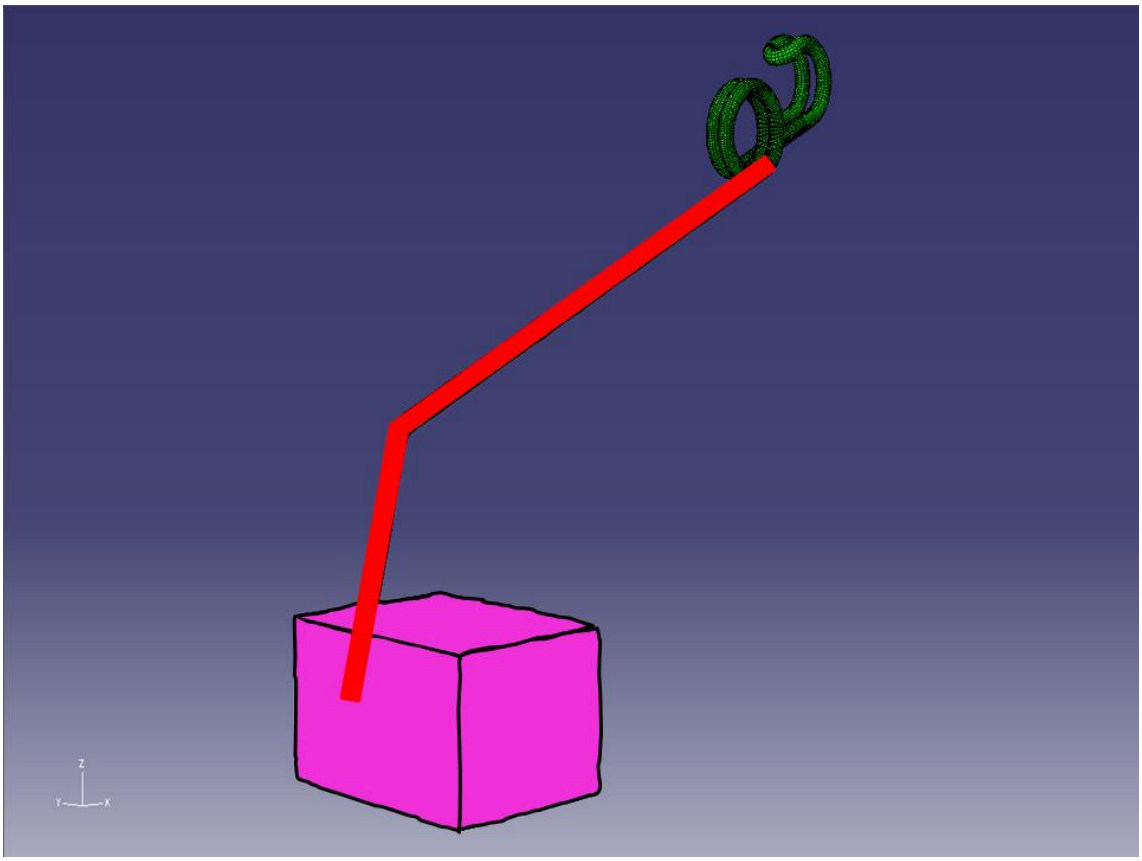

Figure 4.11: Contact surfaces for the soil tine interaction

The contact was modelled as a general surface to surface contact. The parameter for the soil-metal contact (Table 4.7) was the external friction coefficient, which could be assigned via the interaction properties module. Since no adhesion was recorded during the modified direct shear box test for the sandy loam soil studies at the assigned bulk density and moisture content, this was not accounted for in the FEM model (see Section 5.1).

Table 4.7: Parameters for the soil-metal interaction at two studied bulk densities

Soil metal interaction parameters		
	Soil I (1450 Kg m^{-3})	**Soil II (1600 Kg m^{-3})**
External friction coefficient μ [-]	0.60	0.47

5 Results and discussion

This chapter will present and discuss the results obtained from the finite element simulation and from the two experiments.

5.1 Determination of material parameters

5.1.1 Soil-metal interaction properties

As described in section 3.2.2 the maximum shear stress was obtained from the direct shear box test and plotted against the normal stress, as shown in Figure 5.1. A linear regression line is fitted through the data points to get the linear equation to calculate the soil-metal external friction coefficient (slope of the linear line) and the adhesion (intercept of linear line with the shear stress axis). Due to the fact that the intercept was of negative value for both soil bulk densities, adhesion was assumed to be zero, which is in line with findings reported in the literature for a sandy loam soil (Mouazen and Nemenyi [39]). It was found that the external friction coefficient was slightly higher with the lower bulk density of 1450 kg m^{-3} than with the higher bulk density 1600 kg m^{-3}. This might be attributed to a rougher contact soil surface (at micro scale) when the soil is less compacted as compared with a more highly compacted soil. It was possible that the micro structure of the top soil surface was more irregular and uneven at the smaller bulk density than for the higher bulk density. Therefore, the resistance due to the relative movement between the soil and the metal surfaces was higher with a lower bulk density and this causes higher friction represented by a higher friction coefficient.

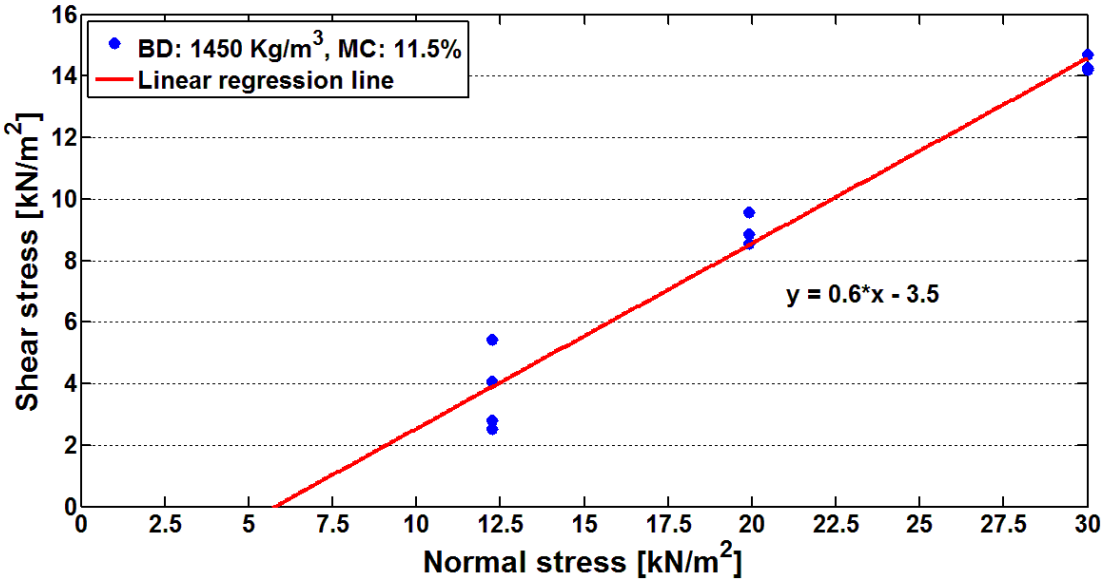

(a)

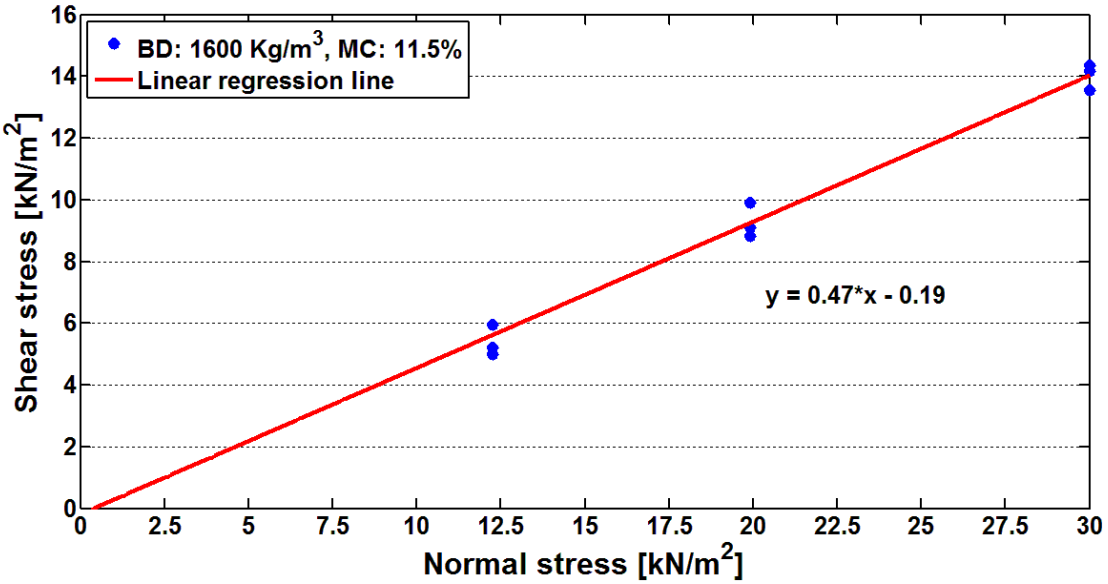

(b)

Figure 5.1: Direct shear box test results for a sandy loam soil measured at a moisture content of 11.5 % with two bulk densities of **(a)** 1450 kg m^{-3} and **(b)** 1600 kg m^{-3}

5.1.2 Soil material properties

Figure 5.2 shows the stress-strain history resulted from the triaxial compression test for the three selected confining pressures of 12, 20 and 30 kPa. As

mentioned in the theory in section 3.2.1, the first part of each curve represents the linear elastic area and is used to calculate the Young's modulus for the soil. The general trend is that with a higher confining pressure the deviatoric stress is higher, due to the fact that a higher confining pressure leads to microcrack closure and the soil specimen stiffening within the rubber membrane, which increases the shear resistance. An increased shear resistance leads to the need for a longer displacement of the piston (axial strain) for the shear failure to take place (Lockner et al. [36]). This effect is reinforced by a higher bulk density, because the soil aggregates are packed closer together leading to a stronger structure as compared with that with a lower bulk density of 1450 kg m^{-3}. With the maximum deviatoric stress, the Mohr's circles can be drawn as shown in Figure 5.3.

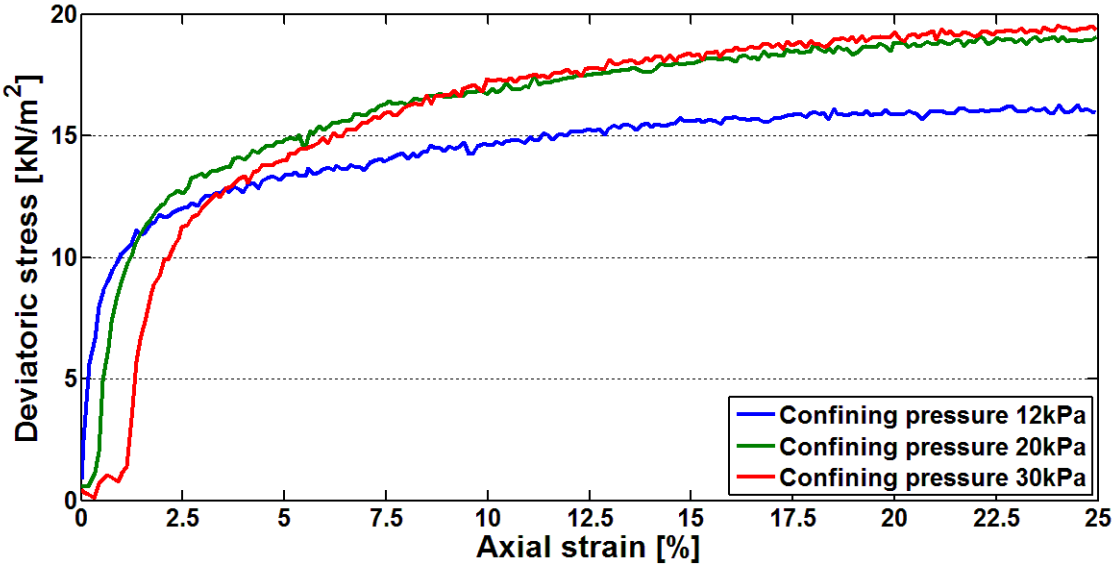

(a)

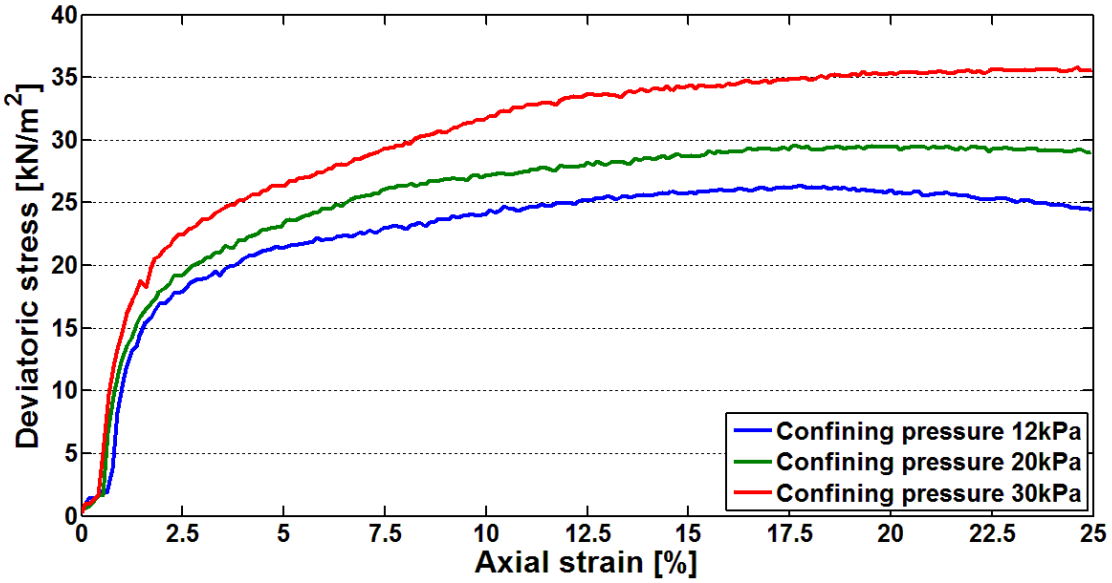

(b)

Figure 5.2: Triaxial compression test results for a sandy loam soil at a moisture content of 11.5 % with two bulk densities of **(a)** 1450 kg m^{-3} and **(b)** 1600 kg m^{-3}

Every Mohr circle represents one confining pressure. Due to the fact that the maximum deviatoric stress increases with bulk density and confining pressure, the circles are different in diameter (Johnson and Bailey [27]). This affects the slope of the circle tangent line and the intercept point with the shear stress axis, which can be observed in Figure 5.3a and b. The increase in friction and cohesion values, with bulk density, is caused by the fact that, when the soil particle density increases and the water content decreases, interlocking and long range forces between the soil particles increases. That leads also to an increase in strength parameters, especially cohesion as reported by McKyes [37].

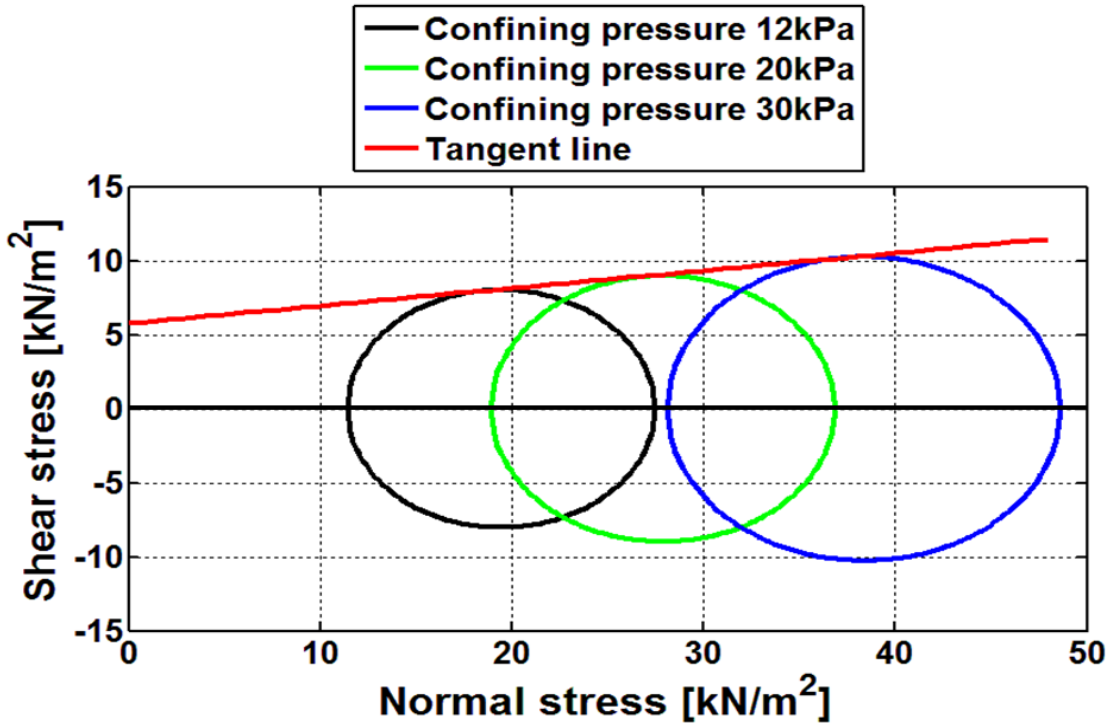

(a)

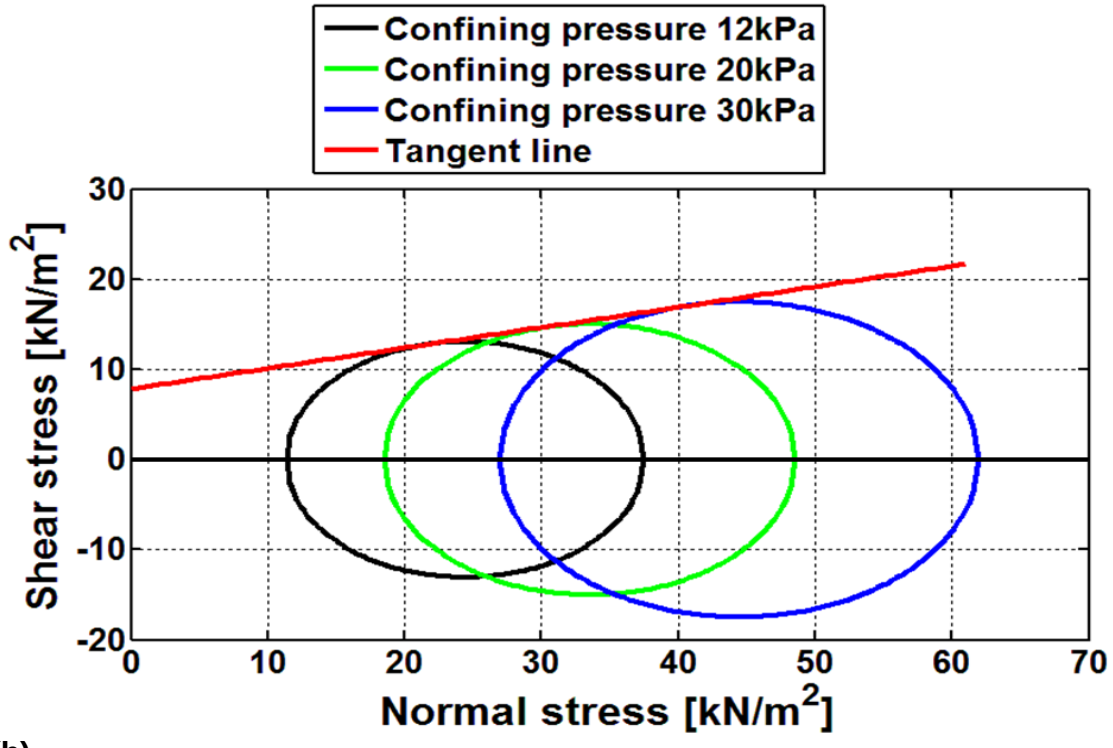

(b)

Figure 5.3: Mohr's circles for obtained from triaxial compression test for three confining pressures at a moisture content of 11.5 % and two bulk densities of **(a)** 1450 kg m^{-3} and **(b)** 1600 kg m^{-3}

The hydrostatic compression test was carried out, to understand the volumetric plastic strain behaviour of the soil, which was necessary to account for soil hardening in the Drucker-Prager soil material model. Figure 5.4 shows that the plastic deformation of a higher compacted soil specimen needs a higher confining pressure to reach the same strain rate as compared to the specimen with a lower bulk density. This can be explained by the different soil stiffness. The higher compaction of soil sample, the harder is soil, which leads to a higher resistance against deformation with the same confining pressure.

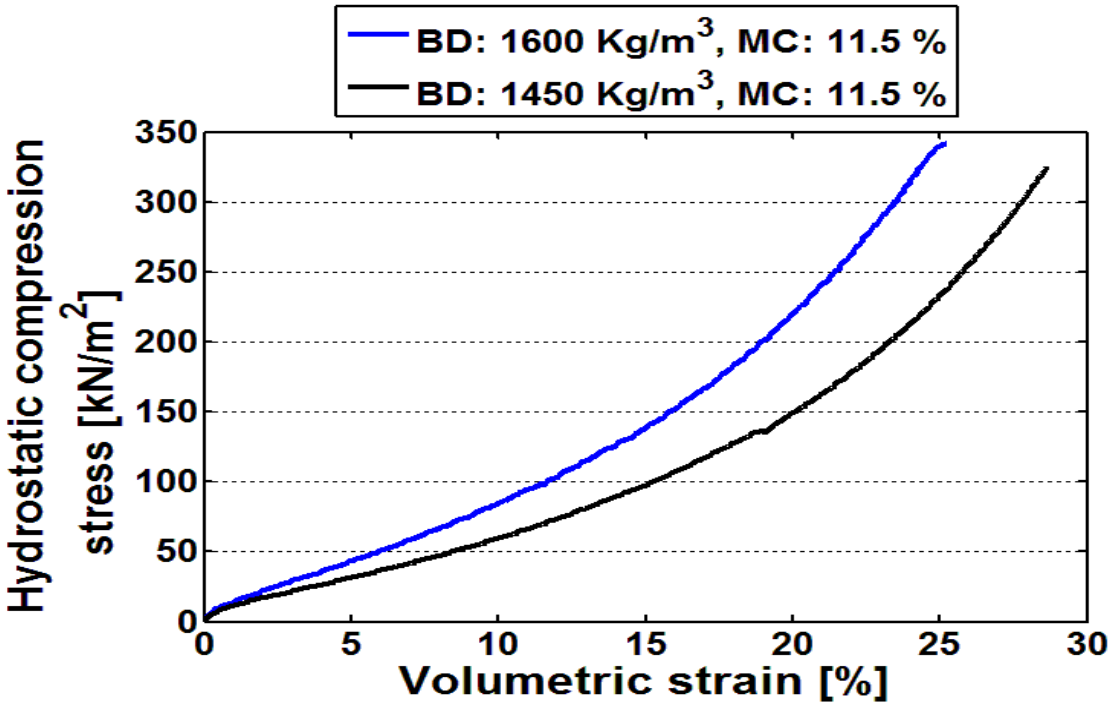

Figure 5.4: Hydrostatic compression test results obtained from triaxial compression test at a moisture content of 11.5 % with two bulk densities of 1450 kg m^{-3} and 1600 kg m^{-3}

The data from the hydrostatic compression test was also used to calculate the Drucker-Prager material parameter R, which determines the shape of the cap in the soil material model and has to be between 0.0001 and 1000. Due to the wide range of R values, it must be approximated carefully as it can influence the

simulation results significantly. This was done with the procedure explained in section 4.3.2.

5.2 Soil bin experiment and FEM simulation

The experimental data obtained from the soil bin test was mainly used to validate the FEM calculation of draught and upwards tine tip movement for the three selected tine geometry used during the FEM simulations. The calculated draught and vertical force were obtained by summing the forces at the cross-section of the loop nodes. The upward tine tip movement was obtained from a selected node on the tine leg, with equal position to the mounting position of the string potentiometer in the experiment. Furthermore, experimental data will be expanded for different tine geometries. Relations between the different parameters: tine geometry, draught, tine tip upward movement, rake angle, working depth, soil bulk density and soil failure length will be shown and discussed.

5.2.1 Validation of the FEM simulation with experimental data

Figure 5.5 shows an example of typical measured data from the soil bin experiment, namely draught, vertical force and tine tip upward movement. Due to the fact that the working speed during the soil bin experiments was slower (0.037 m s^{-1}) than the actual working speed (2 m s^{-1}) during mechanical weeding with flexible tines, in addition to the elimination of bigger clods or plants in the soil bin, no lateral tine tip movement could be observed and thus this was eliminated from this study. As mentioned in section 1.3, the purpose was to investigate the first contact between soil and tine until the first crack (soil failure) occurs. Measured parameters during this stage are compared with those predicted from FEM simulations for the same travel distance. In order to do so it was essential to identify the start point of crack propagation, as illustrated in Figure 5.5.

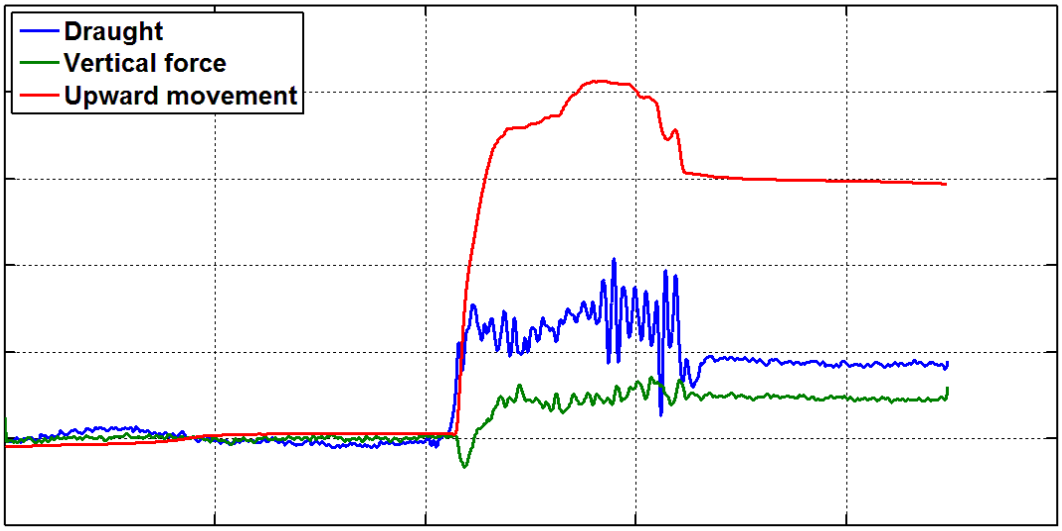

Figure 5.5: Schematic illustration of a typical variation of the three measured signals during the soil bin experiment

It can be observed that the draught increases immediately and sharply after the measurement starts, to arrive at a characteristic peak before the force significantly decreases for the first time, after which draught fluctuates around a plateau. For rake angles of 80° and 104°, the vertical force drops down first until it reaches a negative peak, which can be attributed to the tine being pushed downwards by the torsion spring while penetrating the soil. However, the vertical force rebounds back into the positive range, which can be interpreted by the fact that the tine is pushed upwards by soil resistance. For a rake angle of 56° the vertical force also shows a drop at the beginning, which means the tine is being pushed upwards until reaching a stable working depth where the vertical force increases, explaining that the tine is pushed downwards into the soil (see section 2.2.2). After reaching the positive range, the vertical force fluctuates around a plateau stage, similar to that of the draught, but with much lower magnitude. The upwards movement of the tine tip increases steeply and linearly at the start of the test until it reaches the required working depth where force fluctuated, as the tine is influenced by slightly inhomogeneous soil structure and the presence of small clods from the crack propagation.

Both peaks in draught and vertical force appear nearly at the same time, which can be interpreted by the initiation of cracks in the soil. Before crack occurrence, draught increases with the increase in soil resistance. The torsion of the tine spring is trying to react against soil resistance to ensure the tine penetrates into the soil. After crack occurrence, draught drops down immediately due to the sharp decrease in soil resistance. A similar effect can be observed with the vertical force, where upwards movement was observed before crack initiation in front of the tine. This upward movement was also recorded by a video that enables visualisation of soil cutting, which confirms the upward movement to start at the same time as crack initiation. Therefore, this peak in the vertical force was used as an indicator for choosing the right draught peak, at which crack propagation starts. In some cases the negative peak in the vertical force does not appear at all or was not clear enough to be identified, especially for the stiffest tine 15-228. In this case the first main peak in draught was used, which usually occurs within the first centimetres of tine displacement in the soil, as confirmed by the video and also obviously observed in the signal.

Figure 5.6a and b compares between measured and calculated draught and upward movement, respectively for the tine 15-129, selected as an example. The simulated data had to be filtered, because contact forces have been the most susceptible to noise. The non-filtered data (Figure 5.7a) contain numerous peaks that are completely unrealistic, as stated by Diehl et al. [11].

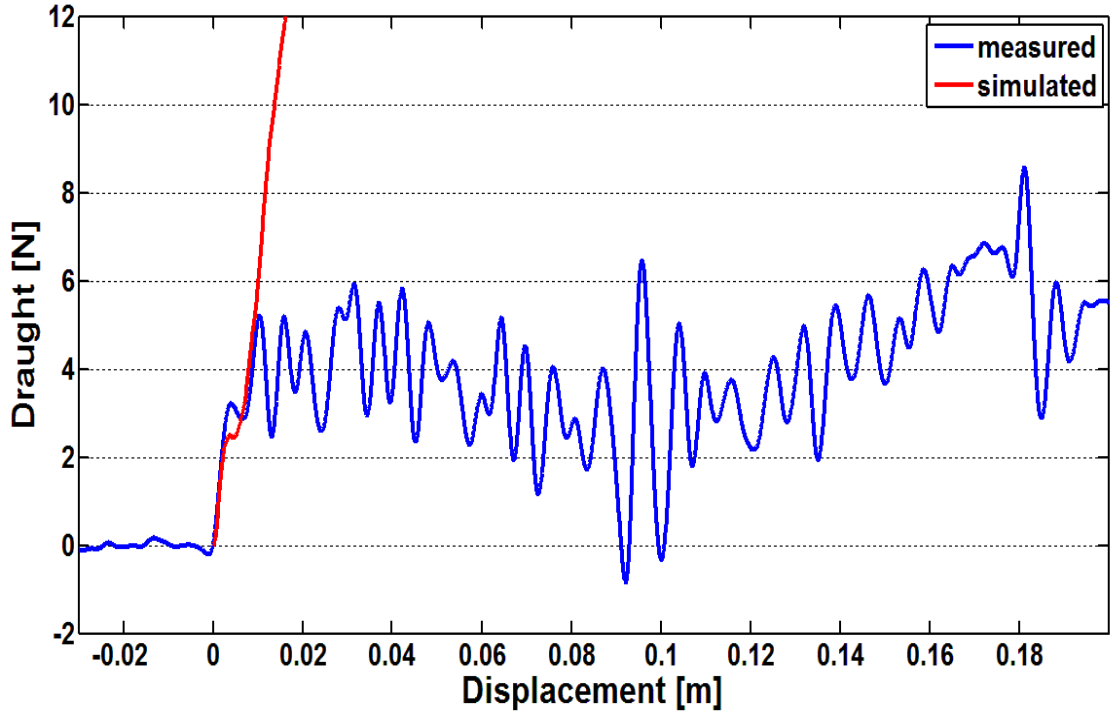

(a)

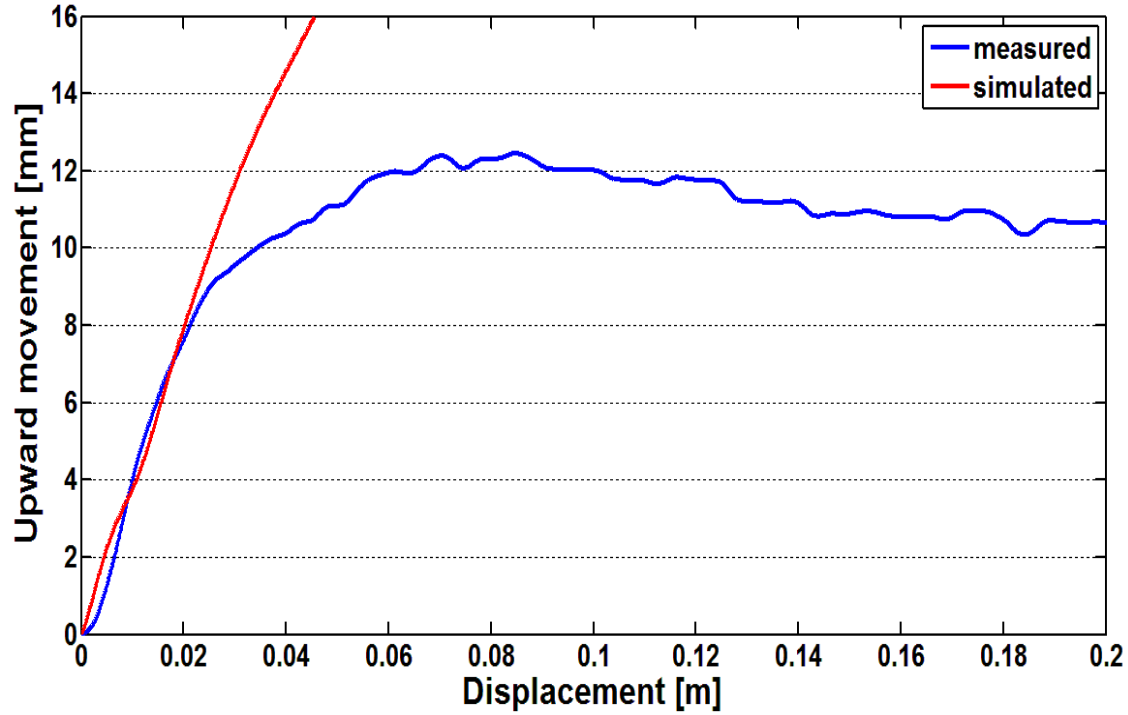

(b)

Figure 5.6: Comparison between measured and simulated tine draught (a) and upward movement (b) of the tine 15-129 at a bulk density of 1450 kg m^{-3}, working depth of 20 mm and rake angle of 80°

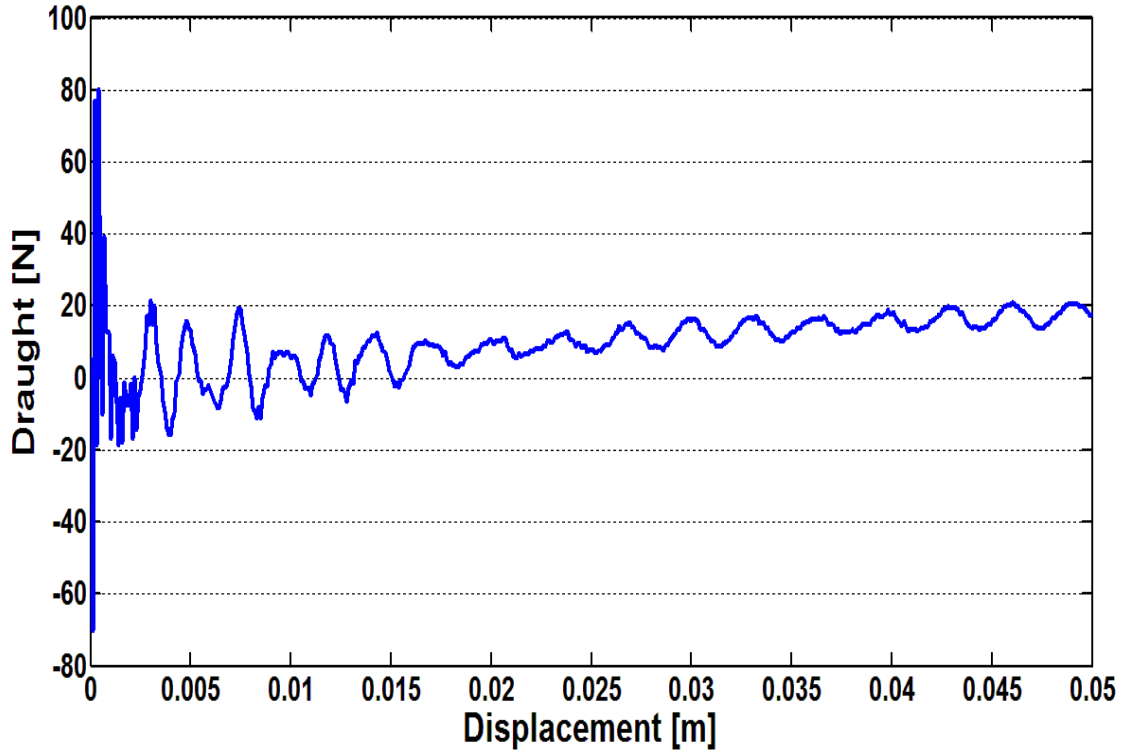

(a)

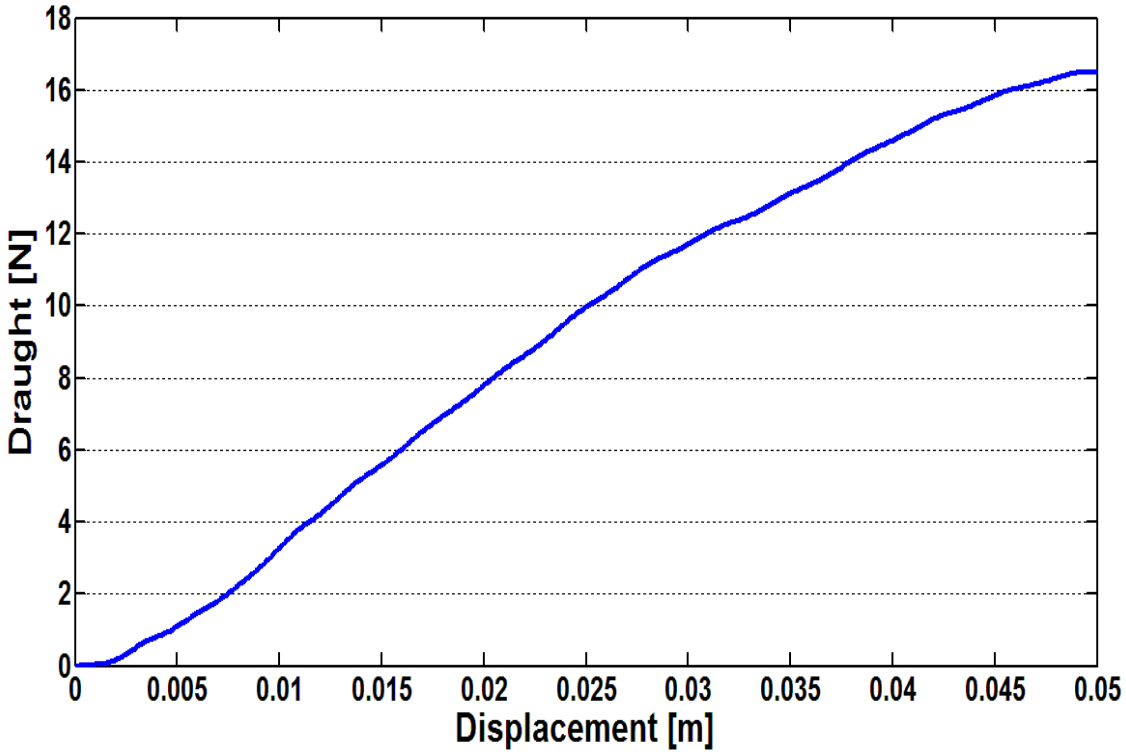

(b)

Figure 5.7: Draught data obtained from the FE simulation with **(a)** non-filtered data and **(b)** filtered data

An almost perfect match between the simulated and measured draught and upwards tine movement was observed (Figure 5.6). They both increase with tine displacement at the same rate until soil failure starts, indicating the initiation of a soil crack, after which the measured draught drops down, whereas the simulated draught further increases. The reason for this behaviour is that the soil in front of the tine tip in the FEM simulation does not crack due to the continuity assumed during FEM simulation. This means that the tine pushes the soil forward, upward and sideward, leading to the accumulation of soil material around the tine. The accumulation of soil leads to increase draught force calculated with FEM, which is in line with findings of other researchers working with FEM simulation of soil-tine interaction (Mouazen et al. [39, 40, 41], Jafari [26] and Abo-Elnor [1]). However, the increase in calculated draught reported in the literature was at smaller rates as compared with those calculated in this project. The reason of that might be the shallow working depth, the small cross-section of the tine and the hardening effect of the Drucker-Prager material model with cap introduced. Due to this FEM limitation, the maximum draught values (see Section 1.3) obtained in the soil bin test were considered. The tine displacement needed to reach these peaks was adopted to determine the maximum draught force calculated with the FEM, which was compared with measured draught to validate the FEM simulations. The same was considered for the upward movement of the tine tip. Figure 5.6b shows a very good match between FEM simulation and measurement until the first crack occurs. The measured tine upward movement reached a plateau stage after soil failure occurs, whereas the simulated movement increased further due to the same reason explained for draught. Therefore, only the maximum upward movement at the end of this linear part was used for further comparisons with corresponding measured values.

The results of the draught and upward movement are summarised for all tests and replications in the appendix A.5. An overview of the average measured and calculated values of draught, upward movement and the error[29] between simulated and measured data are presented, respectively, in Table 5.1, Table

[29] The deviation was calculated relative to one where one is equal 100% deviation.

5.2 and Table 5.3 for the three tines considered during FEM simulation. The error of the FEM calculated draught as compared to soil bin measurements was less than 15 % for the majority of calculation trials, which is in line with previous studies reported in the literature [39], [9], [26]. Only few simulations resulted in higher errors, especially for those of the tine 15-228 at a rake angle of 80°. The maximum error recorded is 64 % for the lower bulk density. Reasons were not obvious but might be due to an error occurring during the soil bin test, or during the FEM simulation. Soil bin measurements for that particular tine geometry were done in one day, where the values for the higher bulk density (small error) were collected in the morning and those of the lower bulk density (high error) were collected in the afternoon, which might led to a slight change in moisture content between the two tests during this time. For example, a change in moisture content could apparently influence the soil viscosity and yield stress, as reported by Karmakar et al. [30]. Due to the complexity of soil material, even small deviations between replicates are observed, as shown in Figure 5.8. Perhaps when all these sources of error come together, the high error recorded between measured and simulated values can be explained. Since the FEM simulation models were all created in the same way that provided good approximations for the higher bulk density, the larger error calculated for the lower bulk density might be due to experimental error as described above. Since the vertical force could not be simulated successfully with FEM (high errors), this was omitted from this study. However, the vertical force has no effect on understanding soil disturbance with flexible tines during mechanical weeding. Furthermore, it does not affect the energy consumption. Omitting this parameter does not affect the general and final output of this project.

Table 5.1: Summary of the FEM simulated and measured average values of tine draught and upward movement for the tine 15-129.

Tine 15-129																		
	Rake angle 56°						Rake angle 80°						Rake angle 104°					
	Draught [N]			Up move [mm]			Draught [N]			Up move [mm]			Draught [N]			Up move [mm]		
Attempt	Ex	Si	Er	Ex	Si	Er	Ex	Si	Er	Ex	Si	Er	Ex	Si	Er	Ex	Si	Er
1450_20	6.02	6.92	0.13	6.60	6.50	0.02	5.25	5.35	0.02	8.77	9.64	0.09	4.51	5.01	0.10	10.13	10.26	0.01
1450_30	8.00	12.71	0.37	10.60	8.66	0.18	4.33	6.14	0.30	14.86	15.88	0.06	6.20	6.16	0.01	17.30	17.18	0.01
1600_20	6.72	6.91	0.03	5.66	5.66	0.00	5.09	4.14	0.19	12.18	12.65	0.04	4.41	5.11	0.14	12.43	13.59	0.09
1600_30	6.39	6.70	0.05	7.70	8.07	0.05	4.23	4.02	0.05	20.36	21.17	0.04	10.73	11.02	0.03	22.94	22.77	0.01

Table 5.2: Summary of the FEM simulated and measured average values of tine draught and upward movement for the tine 15-228.

Tine 15-228																		
	Rake angle 56°						Rake angle 80°						Rake angle 104°					
	Draught [N]			Up move [mm]			Draught [N]			Up move [mm]			Draught [N]			Up move [mm]		
Attempt	Ex	Si	Er	Ex	Si	Er	Ex	Si	Er	Ex	Si	Er	Ex	Si	Er	Ex	Si	Er
1450_20	6.02	6.92	0.13	3.59	3.69	0.03	8.49	14.41	0.41	4.69	5.31	0.12	5.85	6.13	0.05	5.87	6.29	0.07
1450_30	8.00	12.71	0.37	5.34	5.23	0.02	7.57	20.94	0.64	8.15	7.37	0.10	5.71	6.25	0.09	11.54	12.01	0.04
1600_20	6.72	6.91	0.03	5.85	5.80	0.01	9.50	11.37	0.16	6.75	9.68	0.30	8.87	7.99	0.10	8.02	9.70	0.17
1600_30	6.39	6.70	0.05	8.30	8.42	0.01	6.76	8.25	0.18	6.99	7.39	0.05	9.01	10.31	0.13	13.64	14.45	0.06

Table 5.3: Summary of the FEM simulated and measured average values of tine draught and upward movement for the tine 15-054.

Tine 15-054																		
	Rake angle 56°						Rake angle 80°						Rake angle 104°					
	Draught [N]			Up move [mm]			Draught [N]			Up move [mm]			Draught [N]			Up move [mm]		
Attempt	Ex	Si	Er	Ex	Si	Er	Ex	Si	Er	Ex	Si	Er	Ex	Si	Er	Ex	Si	Er
1450_20	6.51	4.98	0.23	8.45	9.14	0.08	4.75	5.13	0.07	8.92	10.15	0.12	4.85	5.77	0.16	8.82	9.37	0.06
1450_30	7.66	6.23	0.19	12.64	10.97	0.13	5.04	4.99	0.01	14.82	15.10	0.02	6.89	7.88	0.12	12.53	12.30	0.02
1600_20	5.21	6.12	0.15	11.96	10.90	0.09	7.08	7.17	0.01	14.49	15.01	0.03	6.04	7.27	0.17	7.72	8.87	0.13
1600_30	4.11	4.81	0.15	13.88	12.04	0.13	5.31	5.30	0.00	23.33	23.94	0.03	8.77	9.18	0.05	18.85	20.12	0.06

The behaviour shown in Figure 5.6 was the common behaviour of the three different tines during the experiments. Furthermore, other behaviours were observed during the soil bin experiment, which will be discussed here.

Figure 5.8 illustrates three replications for the measurement of the tine 15-054. These replications were carried out directly and successively one after another without changing anything in the test set up. The determination of the draught and the upward movement was the same, as explained above. The upward movement in the Figure 5.8b, d and f is, in all cases, the same and does not differ significantly. But, in regard to the draught, changes between the three measurements can be seen. As shown in Figure 5.8a after the first draught peak, a higher second peak was recorded. Due to the advanced tine displacement, it is not possible that this second peak refers to the occurrence of the first crack. This second peak might indicate a second wave of soil failure. The same peak arrangement can also be observed in the second measurement repetition c, but with a significantly smaller difference between the two peaks. The draught in this case is more fluctuating during the plateau stage, as compared to that of Figure 5.8e, which even experienced a decrease after the occurrence of the main peak. This shows, on the one hand, that the first contact is of the most reliable value to be adopted to validate the FEM prediction, because this peak occurs in all three cases after almost the same displacement. On the other hand, this deviation in measured draught, for the same tine geometry, at the same soil conditions, indicates the complexity of the soil mechanical behaviour under external load of tines, even when the test was carried out under controlled conditions, like those adopted in the soil bin in this study. It also shows the influence of barely predictable differences such as crack propagation by tines with a small cross section working at shallow working depths.

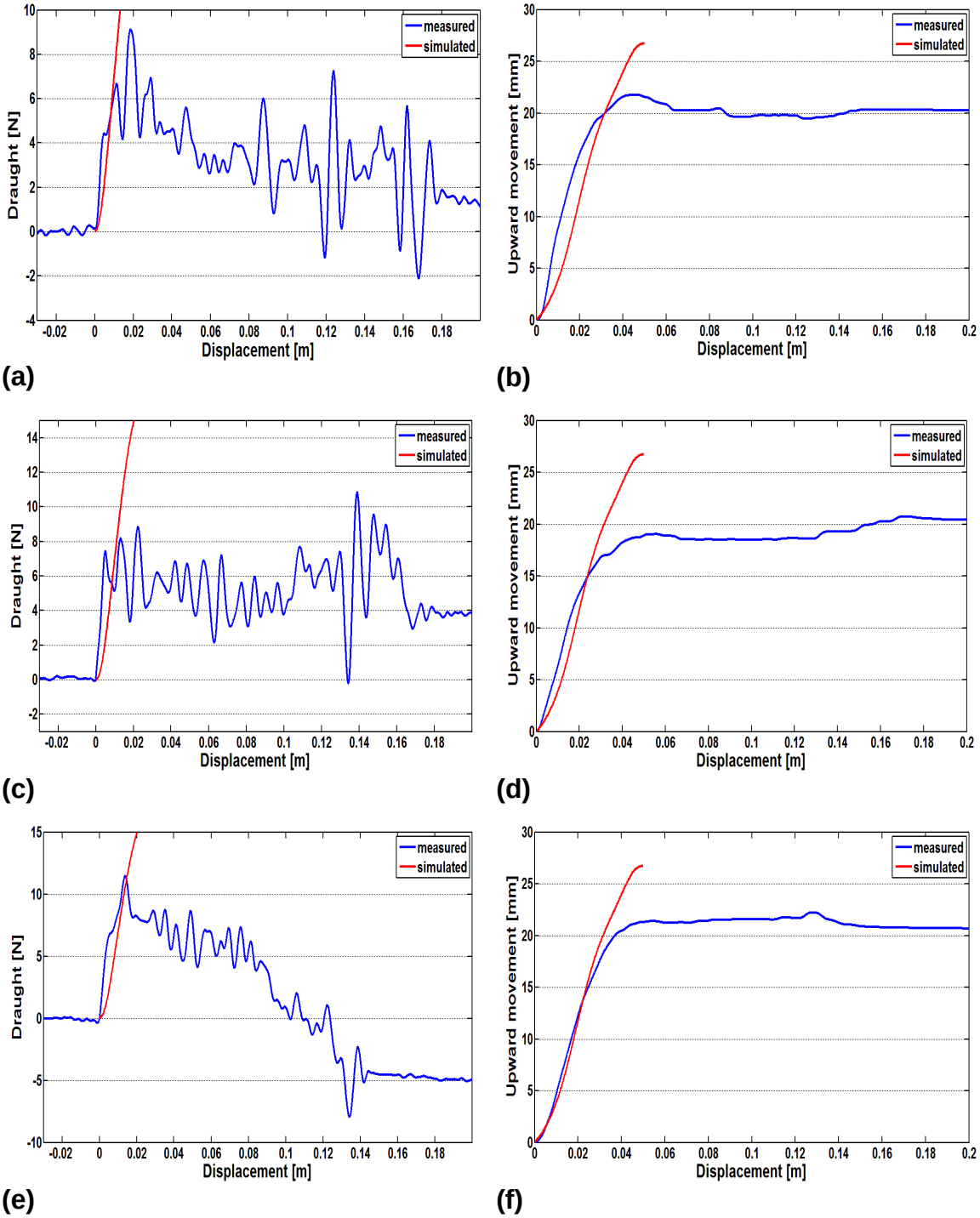

Figure 5.8: Comparison of three measured replications of draught (a, c, e) and tine upward movement (b, d, f) of the tine 15-054 at bulk density of 1600 kg m^{-3}, working depth of 30 mm and rake angle of 104°

Usually the first metal-soil contact results (on average) in the highest draught, since, shortly after this contact, soil failure occurs and the maximum magnitude of draught is reached. An example for an exception is shown in Figure 5.9, where the output of FEM simulation matches those with soil bin measurements regarding the slope of the draught, until the first peak occurs. After this peak the soil crack propagates, leading to draught decrease. Again draught starts to increase showing multiple draught peaks. This behaviour was recorded for the tine 15-228 in nearly every measurement and for the tines 15-129 and 15-054 at only a rake angle of 56°. This makes it impossible to reliably determine the maximum measured draught to be compared with those obtained from simulation. Due to the advanced tine displacement this peak indicates the first occurrence of soil failure. To compare all results under the same conditions, this assumption of the first peak was made for all tines.

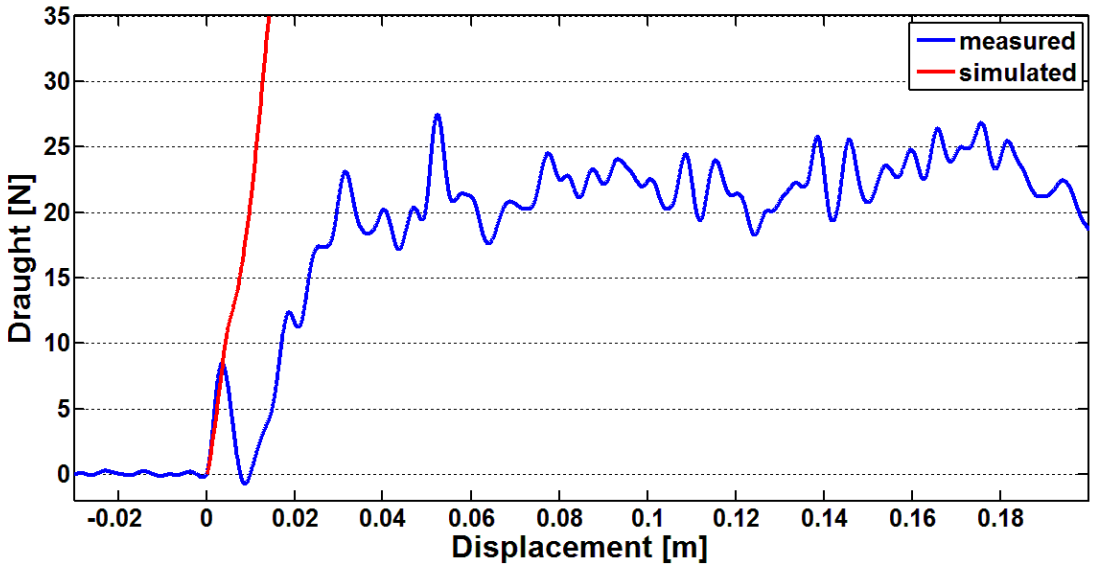

(a)

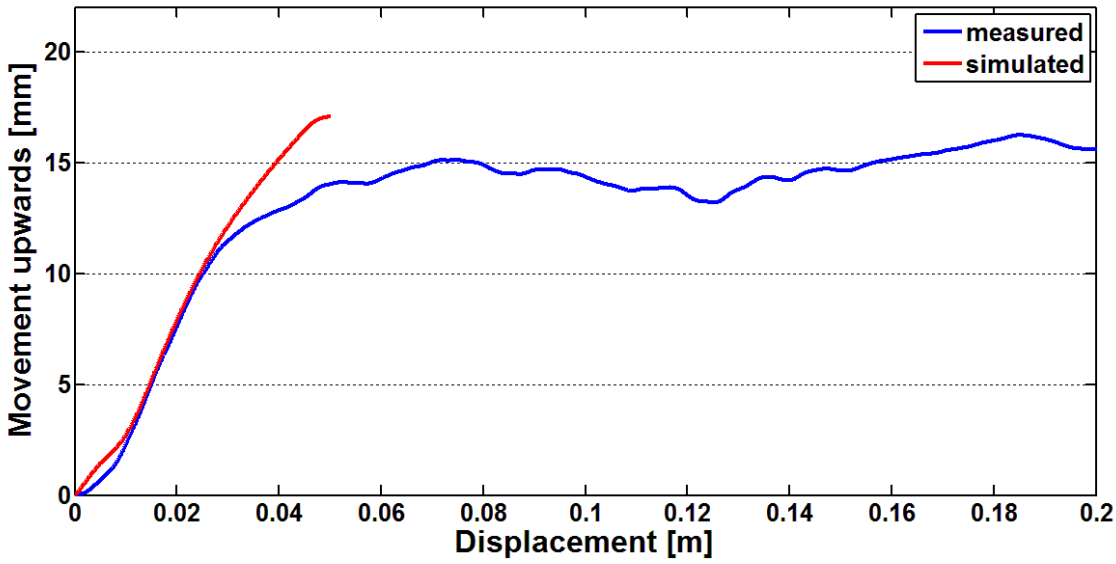

(b)

Figure 5.9: Comparison of measured versus predicted draught (a) and upward movement (b) of the tine 15-228 at a bulk density of 1600 kg m^{-3}, a working depth of 30 mm and a rake angle of 104°

5.2.2 Relationship between tine draught with rake angle, bulk density and working depth

The next three sections will investigate relationships between the first draught peaks, upward movement of the tine and forward soil failure length to explore correlations with tine rake angle, working depth and soil bulk density. Therefore, the data summarised in Table 5.1, Table 5.2 and Table 5.3 are used for the comparison.

5.2.2.1 Relationship between draught and tine rake angle

Figure 5.10 shows the variation in draught with rake angle for different working depths and bulk densities. In general, similar variations can be observed for both measured and simulated draught. This figure also shows almost similar behaviour for different tines at a working depth of 30 mm (Figure 5.10b and d) as those shown in Figure 5.10a and c for a 20 mm tine working depth.

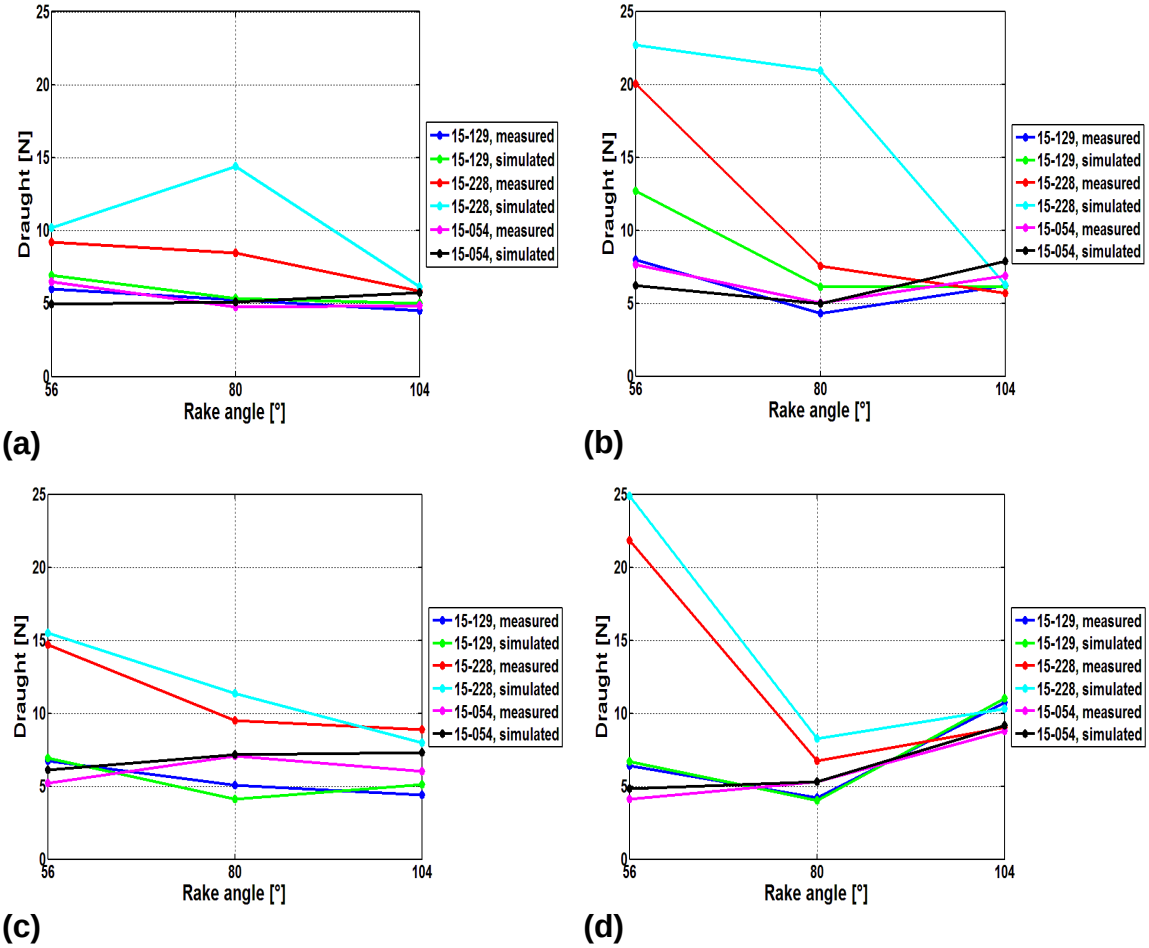

Figure 5.10: Variation of draught as a function of rake angle for different bulk densities (BD) and working depths (WD) with **(a)** BD = 1450 kg m^{-3} and WD = 20 mm; **(b)** BD = 1450 kg m^{-3} and WD = 30 mm; **(c)** BD = 1600 kg m^{-3} and WD = 20 mm; **(d)** BD = 1600 kg m^{-3} and WD = 30 mm

A similar variation in draught for tines 15-228 and 15-129 can be observed in Figure 5.10a, where draught decreases with the rake angle at 20 mm working depth and a bulk density of 1450 kg m^{-3}. This was true for both bulk densities and working depths for the former tines. The tine 15-054 shows a slight increase in draught with rake angle for both bulk densities. The tine 15-228 exhibits the same characteristic as the tine 15-129, but for a higher draught, especially for a rake angle of 56°, which might be attributed to the larger cross-section. However, at trailing positions with rake angles of 80° and 104° the geometric differences have no clear effect on draught. The largest decrease in

draught is between 56° and 80° rake angles, whereas the least is between 80° and 104°.

The draught is slightly higher for 56° than for 104° rake angle, which is also in line with results reported by Duerinckx et al. [12]. With increasing bulk density to 1600 kg m^{-3} the same variation in draught as a function of the rake angle is observed for the tines 15-228 and 15-129, as compared with draught at the lower bulk density shown in Figure 5.10a and b. A large increase in draught with rake angle is observed for both tines 15-129 and 15-054, as shown in Figure 5.10d. Draught variation of the tine 15-228 with rake angle is similar to those for other bulk density and tine working depths. However, in most cases the three tine geometries resulted in a similar draught at the largest rake angle of 104°. Furthermore, it can be observed that the simulated and measured draught is reasonably similar, as shown in Figure 5.10d. The reasons for the high deviation between measured and simulated values for tine 15-228 at the low bulk density of 1450 kg m^{-3} (Figure 5.10a and b) are as discussed in the previous section. It can be concluded that from an energy consumption point of view, a rake angle of 104° will result in the least energy consumption for the tine 15-228, whereas no big differences between different rake angles are expected for tines 15-129 and 15-054.

5.2.2.2 Relationship between draught and bulk density

Figure 5.11 shows variation between draught and bulk density for different tine working depths and rake angles. As in Figure 5.10, except for few cases, a similar tendency between measured and simulated values can be documented. There is no clear variation in draught with bulk density that can be observed for tines 15-129 and 15-054 at a rake angle of 56° (Figure 5.11a and b). The thicker tine 15-228 shows the expected clear increase in draught with bulk density (Figure 5.11a and b) at rake angles of 56° and 104°. Also, the tine 15-054 experiences increases in draught with bulk density for both rake angles of 80° and 104° (Figure 5.11c, d, e and f). This leads to the conclusion that the rake angle and the tine thickness both influence the draught considerably. The flexibility of the tines studied do not allow for clear conclusions to be made. All affecting parameters on draught definetely act interactively. However, at the largest depth and rake angle, almost all tines show clear increase of draught with bulk density (Figure 5.11e and f), which is in line with previous studies using tillage tools (Mouazen and Ramon [42], Khalilian et al. [31], Garner et al. [17], Stafford and Hendrick [53], Shinners et al. [49]).

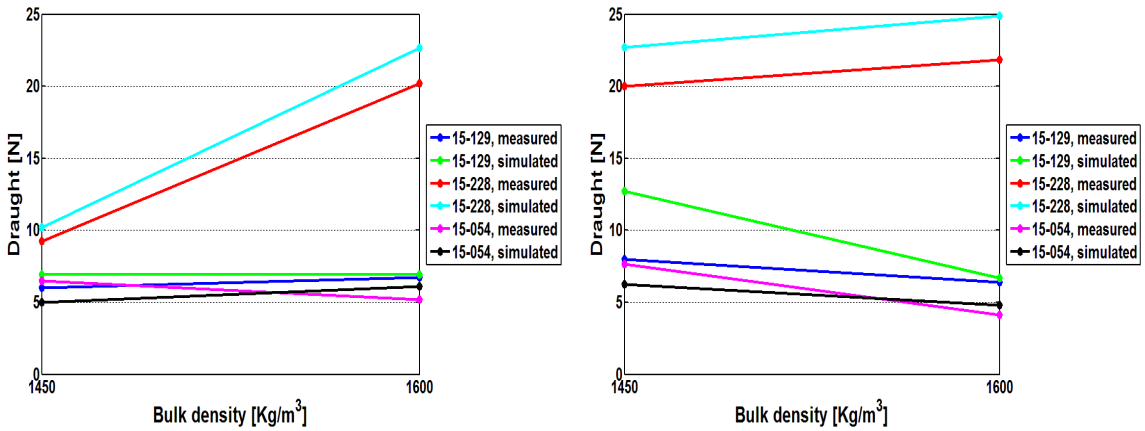

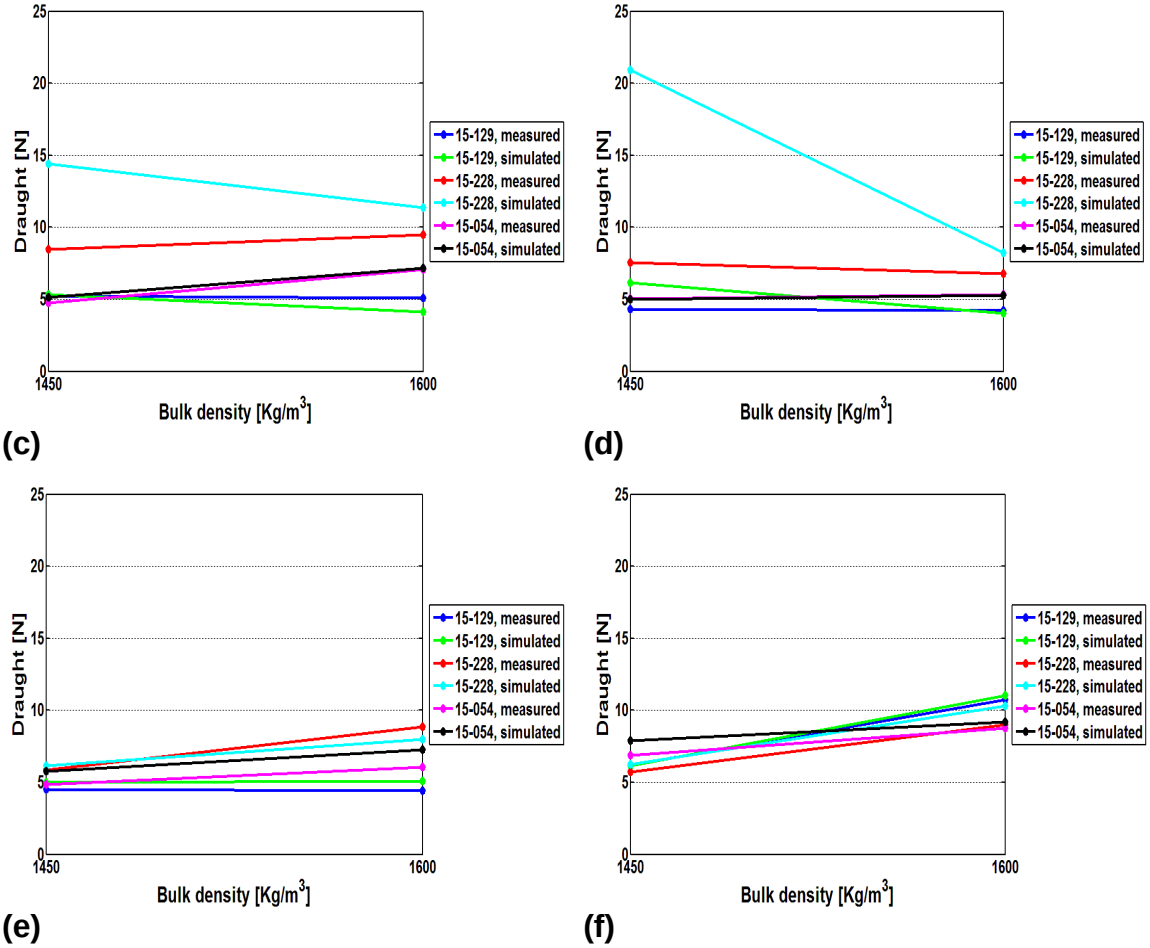

Figure 5.11: Variation of draught with bulk density for different rake angles (RA) and working depths (WD) with **(a)** RA = 56° and WD = 20 mm; **(b)** RA = 56° and WD = 30 mm; **(c)** RA = 80° and WD = 20 mm; **(d)** RA = 80° and WD = 30 mm; **(e)** RA = 104° and WD = 20 mm; **(f)** RA = 104° and WD = 30 mm

5.2.2.3 Relationship between draught and working depth

Figure 5.12a and b shows a minor effect of depth on draught for tines 15-129 and 15-054 at the smallest rake angle of 56°. When combining this observation with that shown in Figure 5.10a and b, it can be concluded that at the smallest rake angle of 56°, only a minor influence of bulk density and depth on draught has to be expected. To this point, it seems as the rake angle has the dominant effect for these two tines at this particular rake angle. At this rake angle, the draught increases with depth for the tine 15-228. The larger tine thickness of

15-228 might explain the increase in draught with depth, since the tine tip does not move so far upwards, as compared to the other two tines. Again, a completely different trend of draught variation can be observed at a rake angle of 80°, where draught decreases with depth for both bulk densities (Figure 5.12c and d). For a rake angle of 104°, draught decreases with depth. No explicit explanation for this behaviour could be found, except the complex interaction of all affecting parameters on tine draught. However, this is another clue that the rake angle might have the dominant effect of tine rake angle as compared to depth, bulk density and tine width.

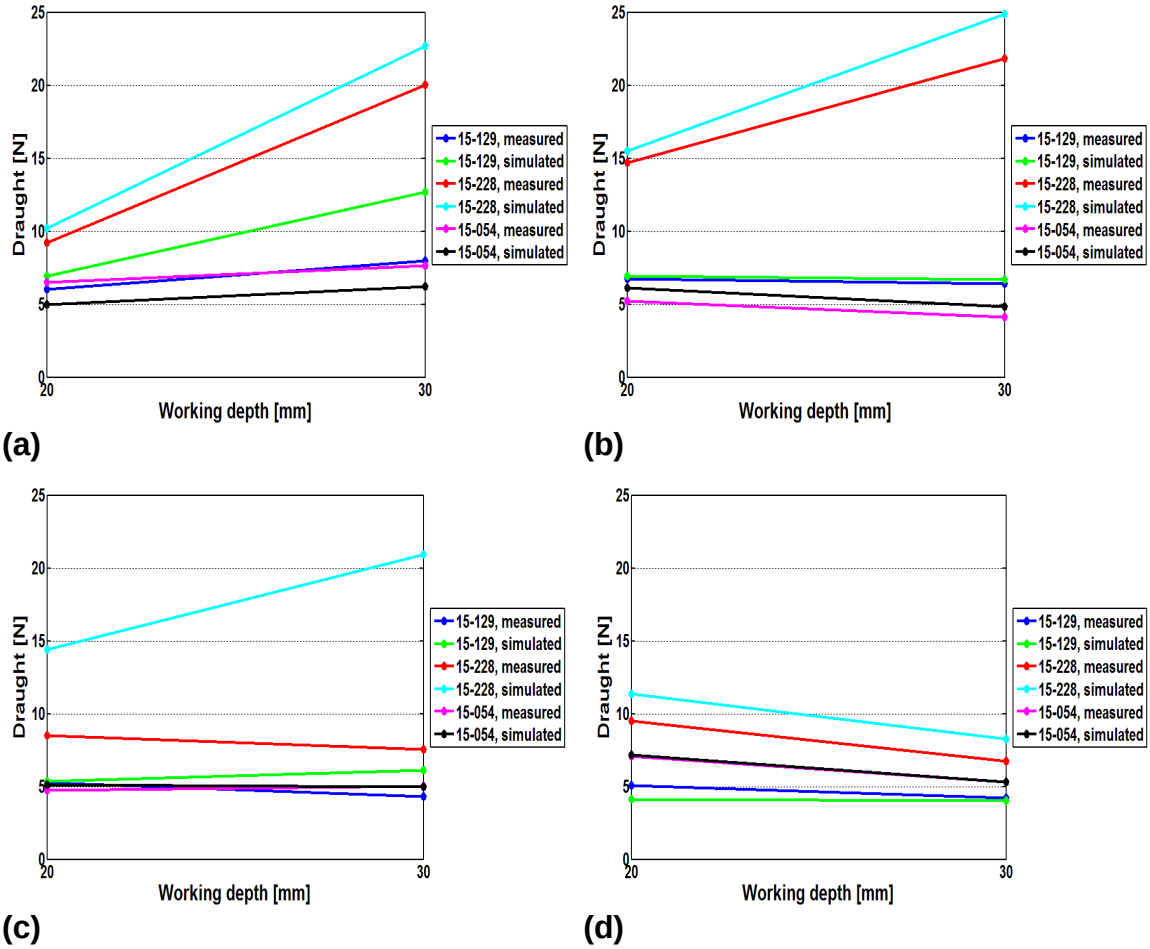

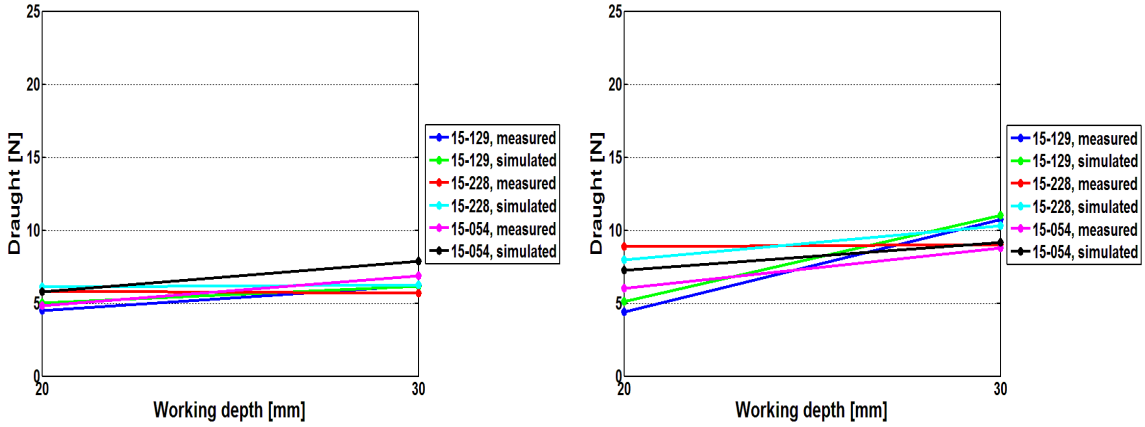

Figure 5.12: Variation in draught with working depth for different rake angles (RA) and bulk densities (BD) with **(a)** RA = 56° and BD = 1450 kg m^{-3}; **(b)** RA = 56° and BD = 1600 kg m^{-3}; **(c)** RA = 80° and BD = 1450 kg m^{-3}; **(d)** RA = 80° and BD = 1600 kg m^{-3}; **(e)** RA = 104° and BD = 1450 kg m^{-3}; **(f)** RA = 104° and BD = 1600 kg m^{-3})

5.2.3 Relationship between tine tip upward movement with tine rake angle, bulk density and working depth

5.2.3.1 Relationship between tine upwards movement and tine rake angle

Another important parameter is the tine tip movement, which affects soil disturbance and the resulted soil covering of weeds or even possibly weed cutting or uprooting. In general, a good match between FEM simulation and soil bin measured variations in the tine upwards movement is achieved. The variation of tine tip movement in the upwards direction with the tine rake angle is shown in Figure 5.13.

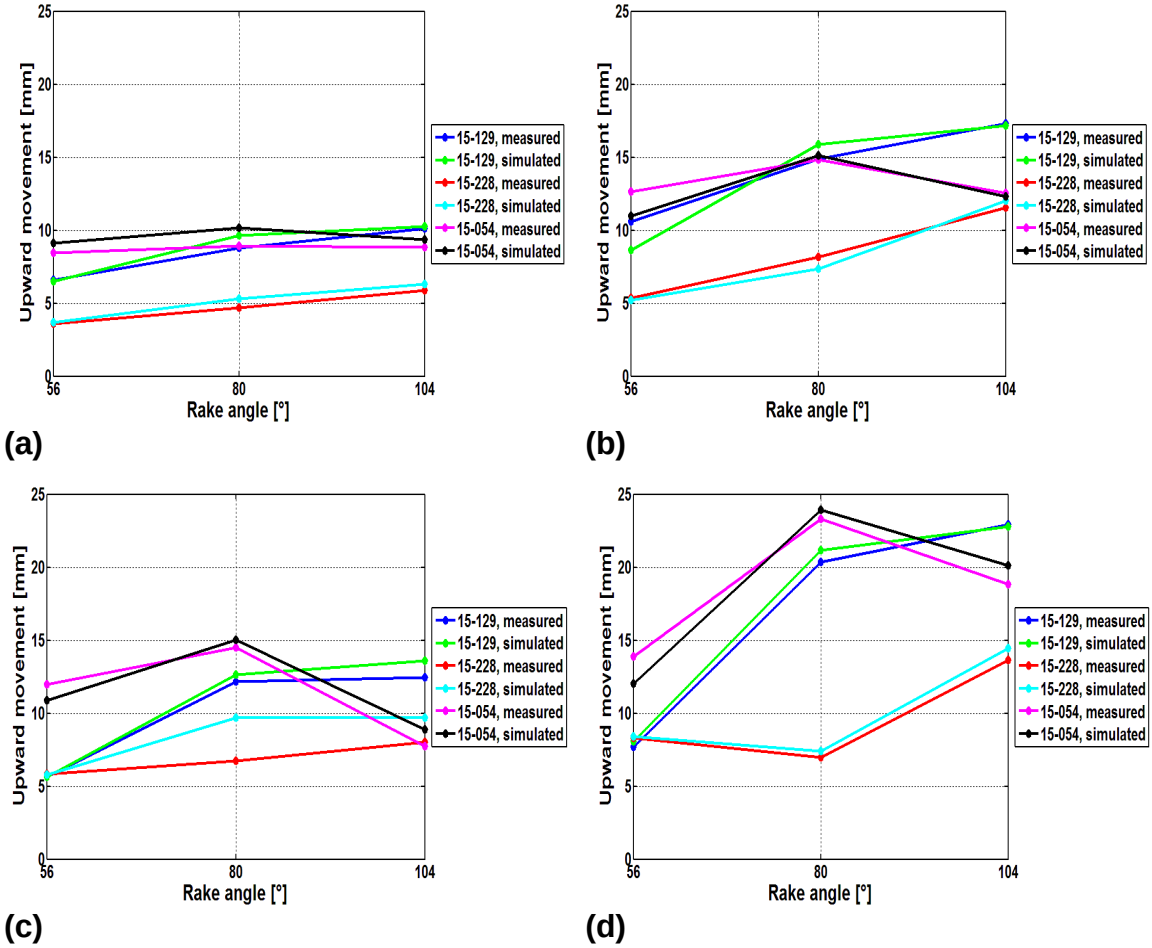

Figure 5.13: Variation of tine upward movement with rake angle for different bulk densities (BD) and working depths (WD) with **(a)** BD = 1450 Kg m^{-3} and WD = 20 mm; **(b)** BD = 1450 Kg m^{-3} and WD = 30 mm; **(c)** BD = 1600 kg m^{-3} and WD = 20 mm; **(d)** BD = 1600 kg m^{-3}) and WD = 30 mm

The general trend is that the upwards tine movement increases with rake angle, which is caused by the resulting force component acting on the tine tip. This means that tine penetration in the soil decreases with rake angle, which results in less soil disturbance. At a rake angle of 56°, the tip is pushed downwards by the vertical force component, whereby the upward movement becomes smaller, as compared with the trailing position at 80° and 104° where the vertical force component acts upwards. This relation is in line with observations reported by Duerinckx et al. [12]. At this relatively low rake angle, soil disturbance is expected to be the largest, for which weed uprooting might be greatest.

However, selectivity cannot be evaluated in this study as only minor tine lateral displacement was recorded due to the low speed considered during both FEM simulation and soil bin test. The tine 15-228 has smaller upward movement than the other two tines, which is caused by the higher stiffness due to a larger cross section of the tine and the higher torsion spring constant. The highest upward movement is recorded for the smallest cross-section tine 15-129, because of the smallest stiffness and the smallest torsion spring constant. This tine has the smallest resistance against the upward movement than the other two tines. Therefore, the tine 15-228 can be recommended for situations where aggressive weeding is required, whereas the tine 15-129 and possibly 15-054 can be recommended for gentle soil disturbance where crop plants are in a delicate growing stage and can be easily damaged. Again selectivity cannot be evaluated based on this data.

The upwards movement of the tine 15-054 varies differently between 80° and 104° rake angles. On the one hand, the tine upward movement at 80° rake angle is very high especially at the high bulk density of 1600 kg m^{-3} and deep working depth of 30 mm (Figure 5.13d). On the other hand, the upward movement of this tine at a rake angle of 104° is smaller than expected in comparison with the other tines (Figure 5.13). The reason could be the longer tine leg, which is easier to bend than the legs of the other two tines, making this tine more flexible.

5.2.3.2 Relationship between tine upwards movement and bulk density

The general trend is that the tine upward movement increases with bulk density, which can be explained by the larger soil resistance to penetration with a larger bulk density. The flexibility of the tines allows the upwards movement, so that the effect of larger bulk density on draught increase was only possible to record at particular combination of tine type and rake angles (Figure 5.10). Figure 5.14a and b shows the upwards movement of tines 15-054 and 15-228 to increase with bulk density at a rake angle of 56° for both working depths. Tine 15-129 shows only minor changes of tine upwards movement with bulk density. The majority of upwards movement for the other two rake angles of 80° and

104° increase with bulk density, which is due to the larger soil resistance that pushed the tine upwards (Figure 5.14c, d, e and f). Only few exceptions occur for the tine 15-228 (Figure 5.14d) and the tine 15-054 (Figure 5.14e), where the upwards movement decreases with bulk density. From the above results discussed it can be concluded that, when weeding is to be carried out in compacted soils with large bulk density, the tine 15-129 at a low rake angle of 56° is recommended.

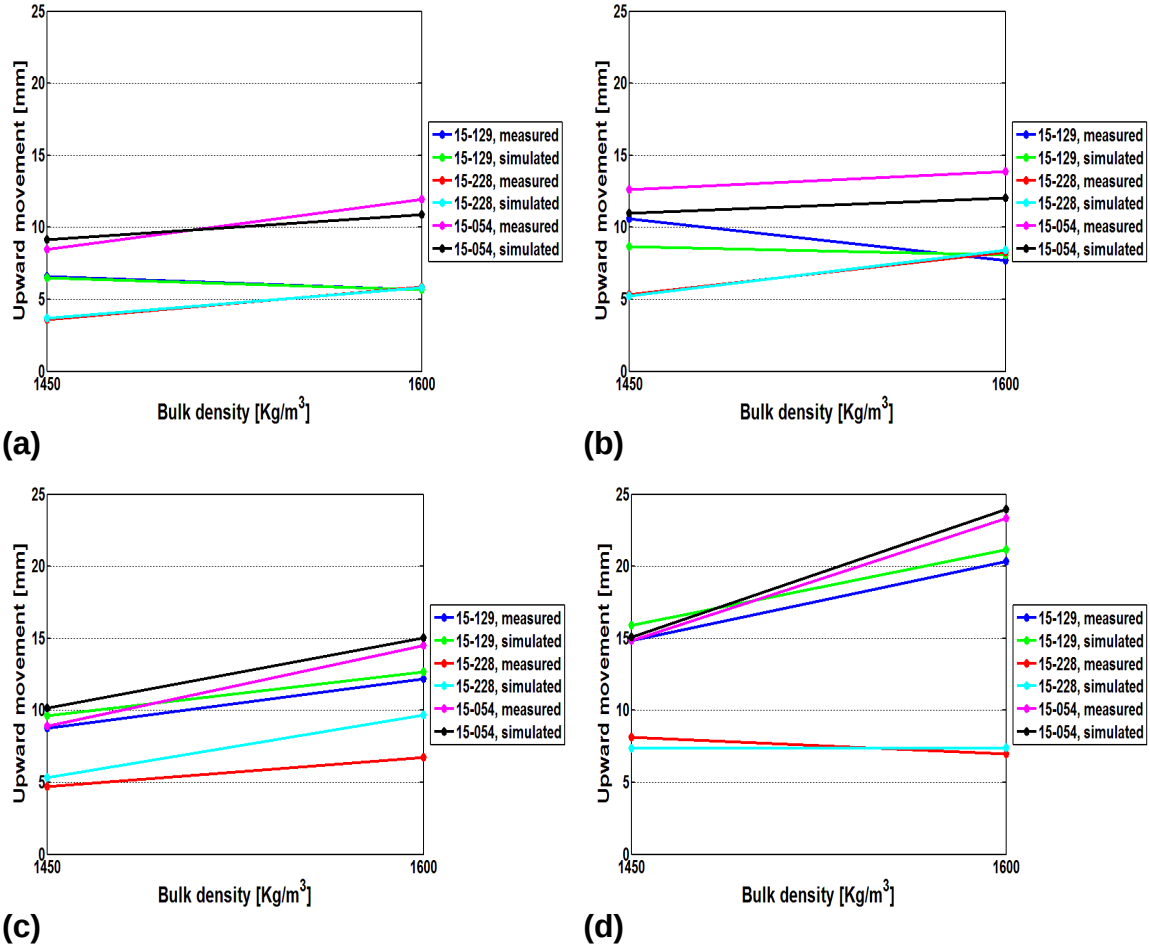

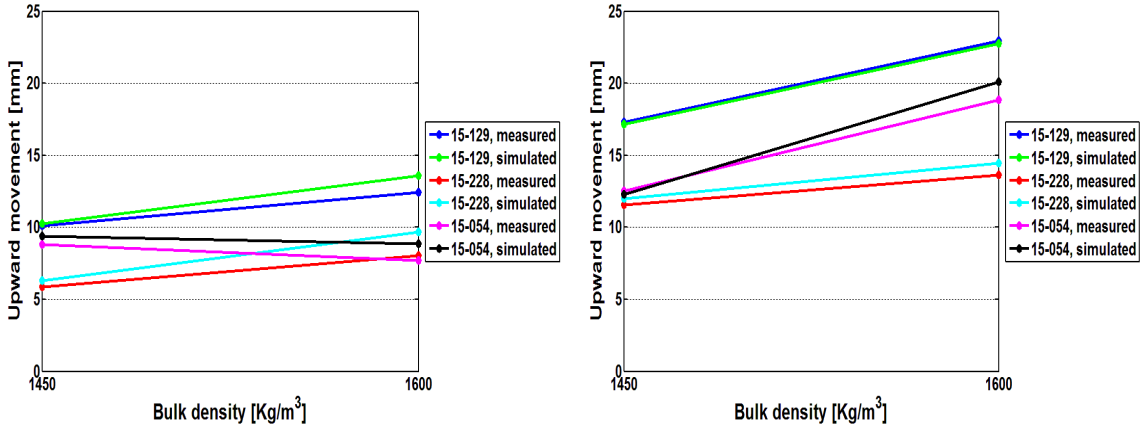

Figure 5.14: Variation of tine upwards movement with bulk density for different rake angles (RA) and working depths (WD) with **(a)** RA = 56° and WD = 20 mm; **(b)** RA = 56° and WD = 30 mm; **(c)** RA = 80° and WD = 20 mm; **(d)** RA = 80° and WD = 30 mm; **(e)** RA = 104° and WD = 20 mm; **(f)** RA = 104° and WD = 30 mm)

5.2.3.3 Relationship between tine upwards movement and working depth

The main trend of variation between tine upwards movement and working depth shown in Figure 5.15 is increasing in the upward movement with working depth. However, again the tine 15-228 experiences the smallest upwards movement in all cases, due to the highest stiffness and torsion spring constant. To ensure a relatively small variation in tine penetration depth, when a deeper (more aggressive) mechanical weeding is required, a stronger torsion spring or stiffer tine geometry is recommended.

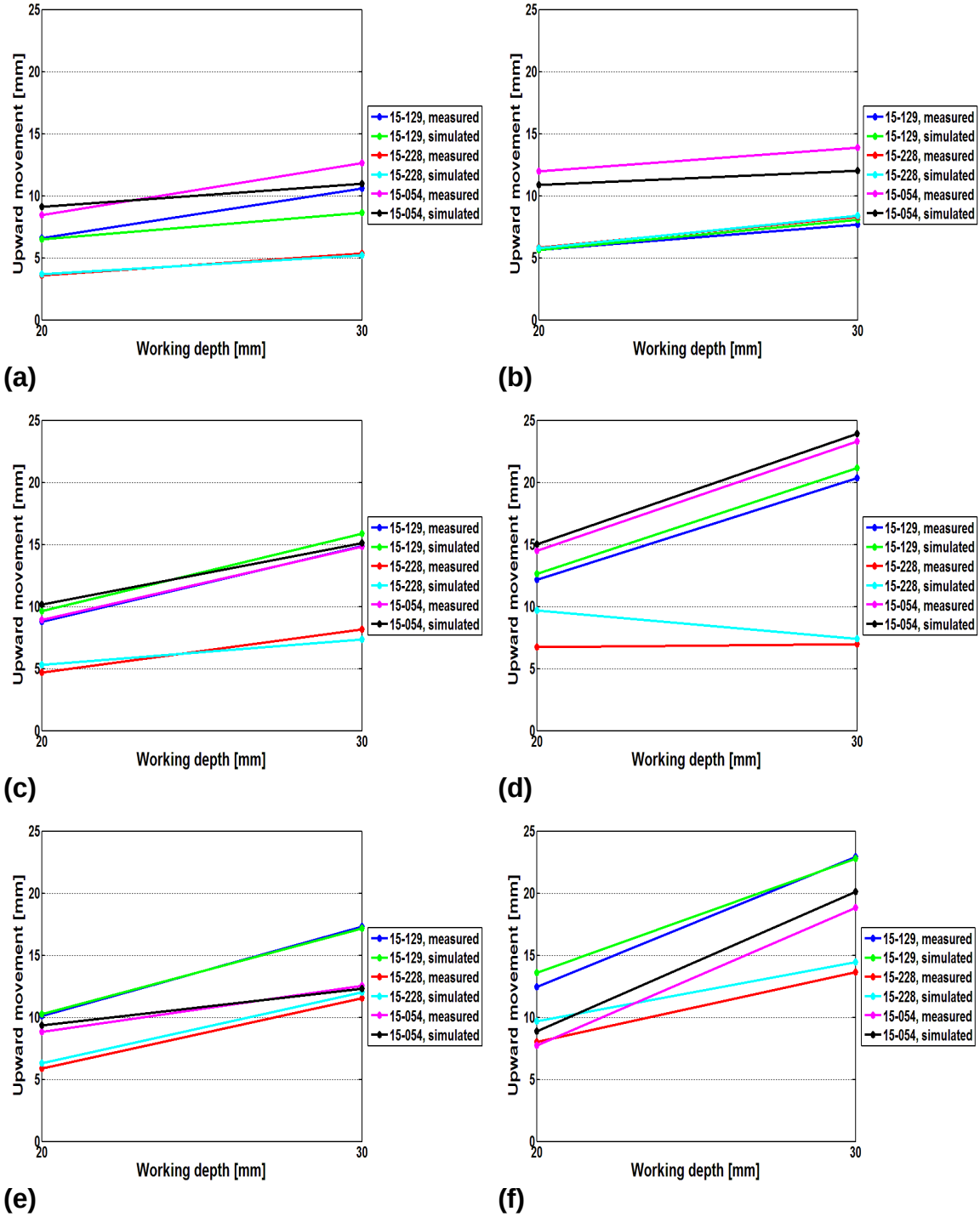

Figure 5.15: Variation of tine upward movement with working depth for different tine rake angles (RA) and bulk densities (BD) with **(a)** RA = 56° and BD = 1450 kg m^{-3}; **(b)** RA = 56° and BD = 1600 kg m^{-3}; **(c)** RA = 80° and BD = 1450 kg m^{-3}; **(d)** RA = 80° amd BD = 1600 kg m^{-3}; **(e)** RA = 104° and BD = 1450 kg m^{-3}; **(f)** RA = 104° and BD = 1600 kg m^{-3}

5.2.4 Relationship of forward soil failure length with tine rake angle, bulk density and working depth

This section presents the variation of calculated forward soil disturbance of the three tines as a function of the tine rake angle, bulk density and working depth. This parameter was not measured during the soil bin experiment. The analysis is focused on the forward soil failure only, since no lateral tine tip movement occurred during the FEM simulation due to the non dynamic interaction proposed with a low speed.

5.2.4.1 Relationship between forward soil movement and tine rake angle

Figure 5.17 shows variation in the forward soil failure length (Figure 5.16) with tine rake angle.

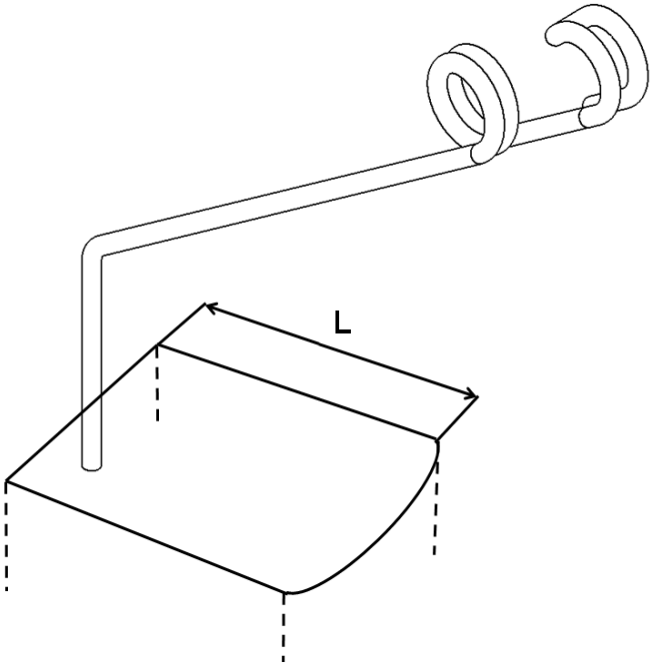

Figure 5.16: Soil failure distance in front of the flexible tine with forward soil failure length (L)

The forward soil displacement generally increases with the rake angle (Figure 5.17). This was also observed in the soil bin after each run. When the tine tip penetrates shallower and close to the soil surface with a smaller rake angle of 56°, a smaller soil volume will be moved in forwards and upwards directions. Furthermore soil disturbance with the biggest cross-section tine (15-228) is larger than those with the other two tines, which are nearly similar in cross-section but significantly smaller than the tine 15-228.

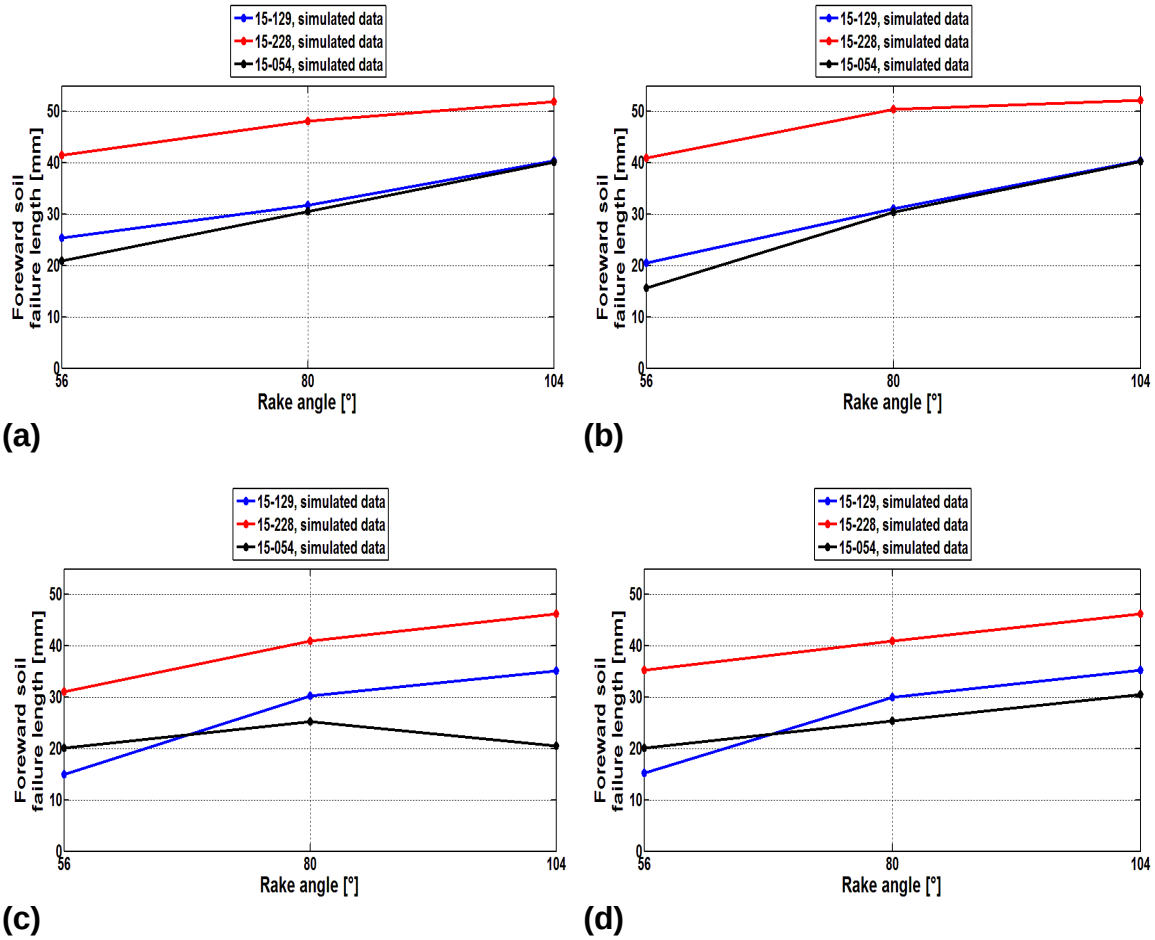

Figure 5.17: Variation in calculated forward soil failure length with rake angles for different bulk densities (BD) and working depths (WD) with **(a)** BD = 1450 kg m^{-3} and WD = 20 mm; **(b)** BD = 1450 kg m^{-3} and WD = 30 mm; **(c)** BD = 1600 kg m^{-3} and WD = 20 mm; **(d)** BD = 1600 kg m^{-3} and WD = 30 mm

5.2.4.2 Relationship between forward soil movement and tine working depth

No clear relationship could be established between forward soil movement and penetration depth (Figure 5.18). Furthermore, when differences in forward soil movement are calculated these were minor and cannot be utilised to draw useful conclusions for mechanical weeding considered in this project. Again the tine 15-228 has developed the largest forward soil movement, confirming the aggressive behaviour of this tine, explaining why this tine is only recommended for extreme weeding cases.

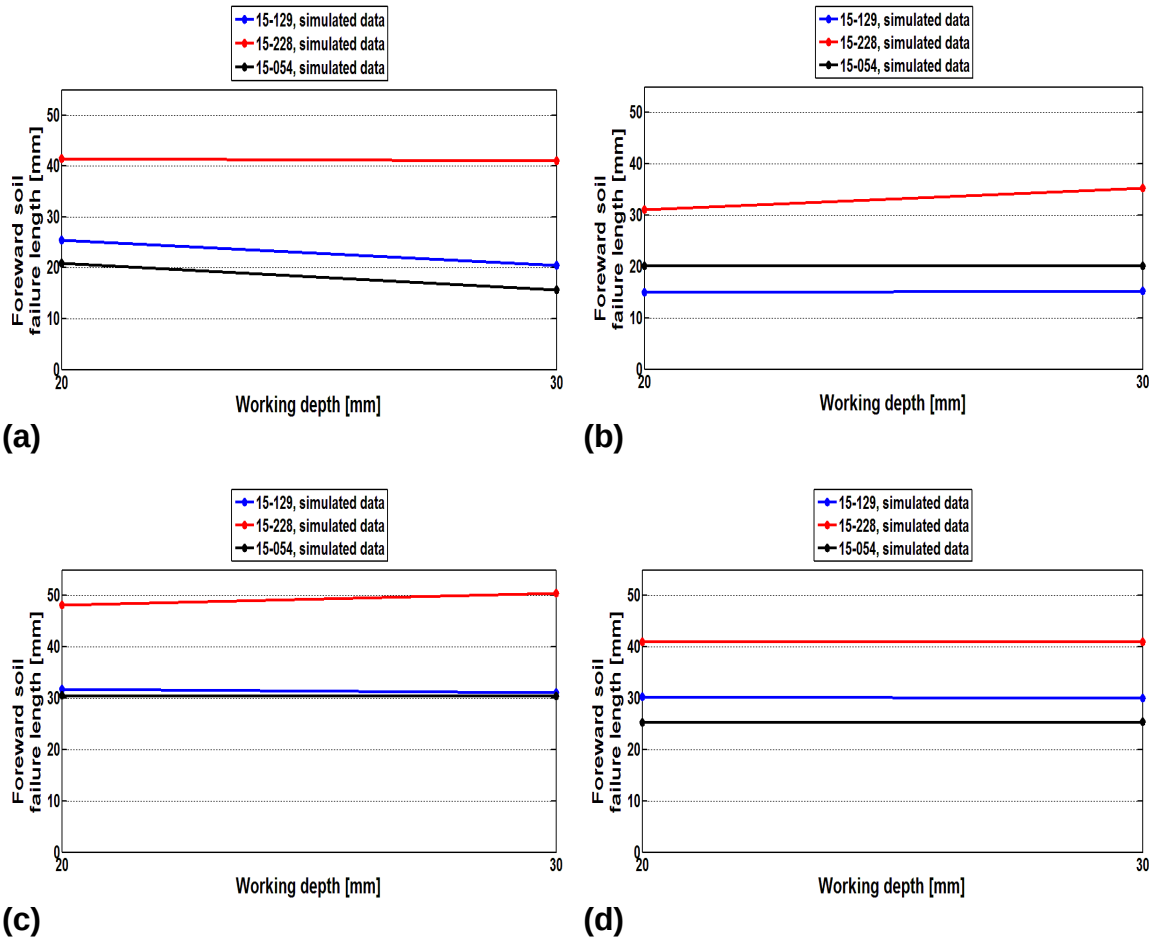

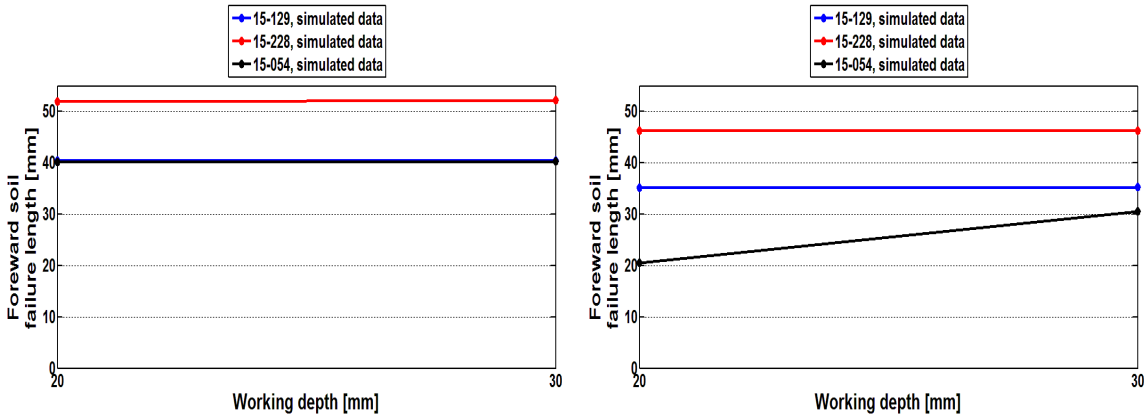

(e) **(f)**

Figure 5.18: Variation of forward soil failure length with tine working depth for different rake angles (RA) and bulk densities (BD) with **(a)** RA = 56° and BD = 1450 kg m^{-3}; **(b)** RA = 56° and BD = 1600 kg m^{-3}; **(c)** RA = 80° and BD = 1450 kg m^{-3}; **(d)** RA = 80° and BD = 1600 kg m^{-3}; **(e)** RA = 104° and BD = 1450 kg m^{-3}; **(f)** RA = 104° and BD = 1600 kg m^{-3}

6 Conclusions

The aim of this work was to implement the FEM to simulate the interaction between flexible tines and soil, aiming at finding optimal tine design parameters and operational conditions for optimal soil disturbance for mechanical weeding. Furthermore, the simulation of flexible tines' movement during the interaction with soil was studied, taking into account the tine design parameters (rake angle and tine geometry) and operational parameters (working depth and bulk density) and their influence on draught and soil disturbance. Overall, the aim of this work was achieved. Nevertheless, as this work represents the first step in the numerical simulation of the interaction between flexible tines, some limitations were found which require further research.

To validate the FEM simulated results of draught and tine upwards movement, a test bench was designed and implemented. Different commercially available tines, provided from the Austrian company Einböck were used. These tines were different in geometry and stiffness, which enabled the investigation of different tine geometric parameters, including three different commonly used rake angles (54°, 80° and 104°) and tines cross sections. Only three tines from those provided by Einböck two bulk densities (1450 kg m^{-3} and 1600 kg m^{-3}) and two penetrating depths (20 mm and 30 mm) were selected for FEM simulations. The soil and soil-metal interface parameters needed to run the FEM simulation were measured with a triaxial compression apparatus and modified direct shear box, respectively. The FEM model developed with an Abaqus 6.9 FEM software and validated with the soil bin tests allowed the following conclusions to be drawn:

1) The test bench designed and implemented to validate the calculated draught, vertical force and tine tip movement was successful in acquiring the required data. However, since no dynamic effect was accounted for in the FEM simulation, measurement was possible for constant low speed.

2) The FEM can be applied successfully to model the interaction between flexible tines and soil to understand the mechanical weeding process, and

optimise tine design parameters, operational conditions and soil conditions for optimal mechanical weeding performance. Most of the error for draught estimation with FEM models was smaller than 15 %. However, the validation of FEM simulation results with the soil bin experiment confirmed that there are limitations to be expected when FEM is utilised to model this complex interaction. Previous studies reported successful FEM simulation of the interaction between rigid tillage tools and soil, which can be attributed to the constant working depth and restricted tine movement in direction of travel only. The flexibility of tines used in this study resulted in a different interaction with the soil as compared to rigid tines, which led to a variable working depth and unconstrained tine tip movement in the upwards and forwards directions. This movement was strongly affected by soil failure and crack propagation.

3) The assumption to use the first peak values before the first crack occurrence in the soil to predict the draught and upward tine tip movement was a valid one for the tines 15-129 and 15-054 at rake angles of 80° as well as for the stiffer tine 15-228 at a rake angle of 56°.

4) The choice of the tine set-up depended on targeted soil conditions as well as how aggressive the process should be. In general, for compacted soil conditions at high bulk densities, it is necessary to select a stiff tine e.g. tines with larger cross section like the tine 15-228 to ensure a suitable working depth. When weeds intensively exist in a field, more aggressive mechanical weeding will be required, for which a less flexible tine is recommended. A tine with a larger torsion spring constant and larger cross section e.g. the tine 15-228 will be of less flexibility and hence recommended for situations with intensive weeds. However, selectivity was not evaluated in this project, as only minor tine lateral displacement was recorded due to the low speed considered during both FEM simulation and the soil bin test. The smaller stiffness and torsion spring constant of the two thinner tines of 15-129 and 15-054 resulted in unstable, highly fluctuated working depth. These tines will be more suitable for weeding at the beginning of the crop growing season, where plants are fragile due to damage by mechanical weeding tools.

5) Bulk density, tine working depth, rake angle and tine cross section all interactively affect draught. However, the rake angle might have the dominant effect on draught as compared to depth, bulk density and tine width. At the largest depth of 30 mm and a rake angle of 104°, almost all tines show clear increase of draught with bulk density. At a suitable bulk density, a thin tine like 15-129 is expected to require less draught and consume less energy than the other two tines due to the smaller cross-section of this tine. The rake angle of 104° will result in the least energy consumption for the tine 15-228, whereas no big differences between different rake angles are expected for tines 15-129 and 15-054. When working with the thinner cross section tine 15-129, it is recommended to adopt the largest rake angle of 104°, since this will lead to reduce variations in the upward movement and ensures a stable working depth, so that the weeds can properly be covered with soil

7 Future work

One of the biggest issues for the simulation of soil-tine interaction with the FEM is the crack propagation in the soil, which strongly influences the tine behaviour. Due to the time limitation of this MSc by Research project, it was not possible to account for crack propagation in the soil with the FEM model. Therefore, further work is needed to account for the crack propagation, which is not possible with the current version of Abaqus code. Ths includes the following possible solutions:

1) Another PHYTON programme code that can be incorporated in Abaqus as subroutine might be an alternative solution, as it provides the possibility to account for this important behaviour during mechanical weeding. This will be based on the concept that an element is deactivated when the maximum yield stress is reached, after which the contribution of this element to the overall soil stiffness equals zero.

2) The discrete element method (DEM) can be an alternative option to FEM, which allows for the simulation of crack propagation in the soil. With the DEM the continuity should not be ensured all the time. The elements are independent from each other and are connected with cohesion forces only, as it occurs between soil aggregates under real world conditions. The advantage is that, due to the tine being inserted into the soil body, these elements are separated so that cracks can occur. Furthermore, with DEM it will be possible to simulate the dynamic interaction.

3) Since the interaction between soil and tine during mechanical weeding involves crop plants and weed, it is suggested to include these components for future investigation. As clod affects the soil-tine interaction behaviour, clods need to be accounted for.

4) The interaction between neighbouring tines as they set on the harrow frame has to be accounted for, since no harrow with a single tine is sold in the market.

REFERENCES

[1] Abo-Elnor, M., Hamilton, R. and Boyle, J. T. (2004), "Simulation of soil-blade interaction for sandy soil using advanced 3D finite element analysis", *Soil and Tillage Research,* vol. 75, no. 1, pp. 61-73.

[2] Abo-Elnor, M., Hamilton, R. and Boyle, J. T. (2003), "3D Dynamic analysis of soil-tool interaction using the finite element method", *Journal of Terramechanics,* vol. 40, no. 1, pp. 51-62.

[3] Abu-Hamdeh, N. H. and Reeder, R. C. (2003), "A nonlinear 3D finite element analysis of the soil forces acting on a disk plow", *Soil and Tillage Research,* vol. 74, no. 2, pp. 115-124.

[4] Araya, K. and Gao, R. (1995), "A Non-linear Three-Dimensional Finite Element Analysis of Subsoiler Cutting with Pressurized Air Injection", *Journal of Agricultural Engineering Research,* vol. 61, no. 2, pp. 115-128.

[5] Asaf, Z., Rubinstein, D. and Shmulevich, I. (2007), "Determination of discrete element model parameters required for soil tillage", *Soil and Tillage Research,* vol. 92, no. 1-2, pp. 227-242.

[6] AutoDesk (2011)*, The Eight-Node Hexahedral "Brick" Element in Finite Element Analysis*, available at: http://www.algor.com/news_pub/tech_white_papers/eight_node/default.asp (accessed 09/2011).

[7] Becker, W. and Gross, D. (2002), *Mechanik elastischer Körper und Strukturen,* Springer, Berlin/ Heidelberg.

[8] Browman, G. (1997), *Steel in the Field, A Farmer's Guide to Weed Management Tools,* 2nd ed, Sustainable Agriculture Network, Beltsville, Maryland, USA.

[9] Chi, L. and Kushwaha, R. L. (1991), "Three-dimensional, finite element interaction between soil and simple tillage tool", *Transactions of the American Society of Agricultural Engineers,* vol. 34, no. 2, pp. 361-366.

[10] Chi, L. and Kushwaha, R. L. (1990), "A non-linear 3-D finite element analysis of soil failure with tillage tools", *Journal of Terramechanics,* vol. 27, no. 4, pp. 343-366.

[11] Diehl, T., Carroll, D. and Nagaraj, B. "Using Digital Signal Processing (DSP) to Significantly Improve the Interpretation of ABAQUS/ Explicit Results", *PROCEEDINGS-ABAQUS Users' Conference,* 25-28 May 1999, Chester, United Kingdom, .

[12] Duerinckx, K., Mouazen, A. M., Anthonis, J. and Ramon, H. (2005), "Effects of spring-tine settings and operational conditions on the mechanical performance of a weed harrow tine", *Biosystems Engineering,* vol. 91, no. 1, pp. 21-34.

[13] Economic and Social Commission for Asia and the Pacific (1983), *Testing, Evaluation and Modification of Weeders* , Publications, Series No. 11 ed, Regional Network for Agricultural Machinery.

[14] Fielke, J. M. (1999), "Finite element modelling of the interaction of the cutting edge of tillage implements with soil", *Journal of Agricultural Engineering Research,* vol. 74, no. 1, pp. 91-101.

[15] Formato, A., Faugno, S. and Paolillo, G. (2005), "Numerical simulation of soil-plough mouldboard interaction", *Biosystems Engineering,* vol. 92, no. 3, pp. 309-316.

[16] Fratta, D., Aguettant, J. and Roussel-Smith, L. (2007), *Introduction to SOIL MECHANICS LABORATORY TESTING,* CRC Press, Boca Raton, Florida, USA.

[17] Garner, T. H., Reynolds, W. R., Musen, H. L., Miles, G. E., Davis, J. W., Wolf, D. and Peiper, U. M. (1987), " Energy Requirement for Subsoiling Coastal Plain Soils", *American Society of Agricultural Engineers,* vol. 30, no. 2, pp. 343-349.

[18] Gee-Clough, D., Wang, J. and Kanok-Nukulchai, W. (1994), "Deformation and Failure in Wet Clay Soil: Part 3, Finite Element Analysis of Cutting of Wet Clay by Tines", *Journal of Agricultural Engineering Research,* vol. 58, no. 2-3, pp. 121-131.

[19] Godwin, R. J. (1975), "An extended octagonal ring transducer for use in tillage studies", *Journal of Agricultural Engineering Research,* vol. 20, no. 4, pp. 347-352.

[20] Godwin, R. J. and Spoor, G. (1977), "Soil failure with narrow tines", *Journal of Agricultural Engineering Research,* vol. 22, no. 3, pp. 213-228.

[21] Grote, K. H. and Feldhusen, J. (2005), *DUBBEL-TASCHENBUCH FÜR DEN MASCHINENBAU,* 21st ed, Springer, Berlin/ Heidelberg.

[22] Helmany, S. (2007), *Applied Soil Mechanics with ABAQUS Applications,* John Wiley & Sons, INC., Hoboken, New Jersey, USA.

[23] Hofer, D. and Kamlah, M. (2005), "Drucker-Prager-Cap creep modelling of pebble beds in fusion blankets", *Fusion Engineering and Design,* vol. 73, no. 2-4, pp. 105-117.

[24] Hofstetter, K. (2002), "Analytic method to predict the dynamic interaction of dozer blade with earthen material.", *Proceedings of the 14th International Conference of the ISTVS,* Vicksburg, MS, USA, .

[25] Hutton, D. (2004), *Fundamentals of Finite Element Analysis,* McGRAW-HILL Companies, Inc., New York, USA.

[26] Jafari, R., Tavakoli Hashjin, S., Minaee, S. and Raoufat, M. H. (2006), "Large deformation modeling in soil-tillage interaction using advanced 3D nonlinear finite element approach", in Madureira, A. M. (ed.), *Proceedings of the 6th WSEAS International Conference on Simulation, Modelling and Optimization,* September 22-24, 2006, Lisbon, Portugal, World Scientific and Engineering Academy and Society, pp. 246.

[27] Johnson, C. E. and Bailey, A. C. (2002), "Soil compaction", *In Advances in Soil Dynamics,* vol. 2, pp. 155-178.

[28] Karmakar, S. and Kushwaha, R. L. (2006), "Dynamic modeling of soil-tool interaction: An overview from a fluid flow perspective", *Journal of Terramechanics,* vol. 43, pp. 411-425.

[29] Karmakar, S. and Kushwaha, R. L. (2005), "CFD simulation of soil forces on a flat tillage tool", *2005 ASAE Annual International Meeting,* 17 July 2005 through 20 July 2005, Tampa, FL, .

[30] Karmakar, S., Ashrafizadeh, R. and Kushwaha, R. L. (2007), "Experimental validation of CFD modeling for narrow tillage tool draft", *2007 ASABE Annual International Meeting, Technical Papers,* Vol. 2 BOOK, 17 June 2007 through 20 June 2007, Minneapolis, MN, .

[31] Khalilian, A., Garner, T. H., Musen, H. L., Dodd, R. B. and Hale, S. A. (1988), "Energy for Conservation Tillage in Coastal Plain Soils", *Transactions of the ASAE,* vol. 31, no. 5, pp. 1333-1337.

[32] Koch, W. (1964), "Unkrautbekämpfung durch Eggen, Hacken und Meisseln in Getreide I. Wirkungsweise und Einsatzzeitpunkt von Egge, Hacke und Bodenmeissel", *Zeitschrift für Acker- und Pflanzenbau,* vol. 120, pp. 369-382.

[33] Kurstjens, D. A. G. and Perdok, U. D. (2000), "The selective soil covering mechanism of weed harrows on sandy soil", *Soil and Tillage Research,* vol. 55, no. 3-4, pp. 193-206.

[34] Kushwaha, R. L. and Shen, J. (1995), "FINITE ELEMENT ANALYSIS OF THE DYNAMIC INTERACTION BETWEEN SOIL AND TILLAGE TOOL", vol. 37, no. 5, pp. 1315-1319.

[35] Lesjöfors (2011), *List of materials for standard spring steels used in the spring industry*, available at: http://catalog.lesjoforsab.com/pdf/en/chapters/210-211_EN.pdf (accessed 09/2011).

[36] Lockner, D.A., and S.A. Stanchits (2002), "Undrained poroelastic response of sandstones to deviatoric stress change", *Journal of Geophysical Research,* vol. 107.

[37] McKyes, E. (1989), *Agricultural Engineering Soil Mechanics,* Elsevier Science Publishers B. V., Amsterdam, The Netherlands.

[38] Mouazen, A. M., Duerinckx, K., Ramon, H. and Anthonis, J. (2007), "Soil Influences on the Mechanical Actions of a Flexible Spring Tine during Selective Weed Harrowing", *Biosystems Engineering,* vol. 96, no. 1, pp. 7-18.

[39] Mouazen, A. M. and Neményi, M. (1999), "Tillage tool design by the finite element method: Part 1. Finite element modelling of soil plastic behaviour", *Journal of Agricultural Engineering Research,* vol. 72, no. 1, pp. 37-51.

[40] Mouazen, A. M. and Neményi, M. (1999), "Finite element analysis of subsoiler cutting in non-homogeneous sandy loam soil", *Soil and Tillage Research,* vol. 51, no. 1-2, pp. 1-15.

[41] Mouazen, A. M., Neményi, M., Schwanghart, H. and Rempfer, M. (1999), "Tillage tool design by the finite element method: Part 2. Experimental validation of the finite element results with soil bin test", *Journal of Agricultural Engineering Research,* vol. 72, no. 1, pp. 53-58.

[42] Mouazen, A. M. and Ramon, H. (2002), "A numerical-statistical hybrid modelling scheme for evaluation of draught requirements of a subsoiler cutting a sandy loam soil, as affected by moisture content, bulk density and depth", *Soil and Tillage Research,* vol. 63, no. 3-4, pp. 155-165.

[43] Nasdala, L. (2010), *FEM-Formelsammlung Statik und Dynamik, Hintergrundinformationen, Tipps und Tricks,* 1. ed, Vieweg+Teubner, Wiesbaden.

[44] Nordell, L. K. (1997), "Particle flow modelling: transfer chutes other applications.", *Chute design conference BELTCON,* Republic of South Afrika, .

[45] Plouffe, C., Richard, M. J., Tessier, S. and Laguë, C. (1999), "VALIDATIONS OF MOLDBOARD PLOW SIMULATIONS WITH FEM ON A CLAY SOIL", *Transactions of the ASAE,* vol. 6, no. VOL. 42, pp. 1523-1530.

[46] Rasmussen, J. (1992), "Testing harrows for mechanical control of annual weeds in agricultural crops", *Weed Research,* vol. 32, no. 4, pp. 267-274.

[47] Rosa, U. A. and Wulfsohn, D. (1999), "Constitutive model for high speed tillage using narrow tools", *Journal of Terramechanics,* vol. 36, no. 4, pp. 221-234.

[48] Rydberg, T. (1993), "Weed harrowing-driving speed at different stages of development.", *Swedish Journal of Agricultural Research,* , no. 34, pp. 107-113.

[49] Shinners, K. J., Alcock, R. and Wilkes, J. M. (1990), " COMBINING ACTIVE AND PASSIVE TILLAGE ELEMENTS TO REDUCE DRAFT REQUIREMENTS", *American Society of Agricultural Engineers,* vol. 33, no. 2, pp. 400-404.

[50] Shmulevich, I., Asaf, Z. and Rubinstein, D. (2007), "Interaction between soil and a wide cutting blade using the discrete element method", *Soil and Tillage Research,* vol. 97, no. 1, pp. 37-50.

[51] Simulia (2009)*, Abaqus 6.9 Online documentation*, available at: http://abaqus.civil.uwa.edu.au:2080/v6.9/index.html (accessed 09/2011).

[52] Søgaard, H. T. (1998), "Automatic control of a finger weeder with respect to the harrowing intensity at varying soil structures", *Journal of Agricultural Engineering Research,* vol. 70, no. 2, pp. 157-163.

[53] Stafford, J. V. and Hendrick, J. G. (1988), "Dynamic Sensing of Soil Pans", *American Society of Agricultural Engineers,* vol. 31, no. 1, pp. 9-13.

[54] Swick, W. C. and Perumpral, J. V. (1988), "A model for predicting soil-tool interaction", *Journal of Terramechanics,* vol. 25, no. 1, pp. 43-56.

[55] Tanaka, H., Oida, A., Daikoku, M., Inooku, K., Sumikawa, O., Nagasaki, Y. and Miyazaki, M. (November, 2007), "DEM Simulation of Soil Loosening Process Caused by a Vibrating Subsoiler", *Agricultural Engineering International: CIGR Ejournal,* , no. Vol. IX.

[56] Upadhyaya, S. K., Rosa, U. A. and Wulfsohn, D. (2002), "Application of the finite element method in agricultural soil mechanics", in *Advances in Soil Dynamics,* 2nd ed, ASAE, St. Joseph, Michigan, USA, pp. 117-153.

[57] Van der Weide, R. Y., Bleeker, P. O., Achten, V. T. J. M., Lotz, L. A. P., Fogelberg, F. and Melander, B. (2008), "Innovation in mechanical weed control in crop rows", *Weed Research,* vol. 3, no. 48, pp. 215-224.

[58] Warrick, A. W. (2002), *SOIL PHYSICS COMPANION,* CRC Press, Boca Raton, Florida, USA.

[59] Zhang, J. and Kushwaha, R. L. (1998), "Dynamic analysis of a tillage tool: Part I - Finite element method", vol. 40, no. 4, pp. 287-292.

[60] Zienkiewicz, O. C. and Taylor, R. L. (1989), *The Finite Element Method Volume 1 - Basic Formulations and Linear Problems,* 4th ed, McGRAW-HILL Book Company (UK) Limited, Maidenhead, Berkshire, England.

APPENDICES

Appendix A

A.1 Data of flexible tine geometery

The following tables provide the spring steel material data, the torsion spring constants and further geometry dimensions of the tines.

Table A.1.1: Material data and dimensions of all flexible tines, which were provided by Einböck

Young's modul [N/m^2]: 2,085E+11

Shear modul [N/m^2]: 8,04E+10

Poisson's ratio: 0,297

Density [Kg/m^3]: 7850

Tine	Wire diameter [mm]	Length [mm]	Inner coil diameter [mm]	Outer coil diameter [mm]	Mean coil diameter [mm]	Number of loops
15-129	6,5	490	36	49	42,5	2
15-002	7	490	36	50	43	2
15-054	7	600	36	50	43	2
15-099	8	490	36	52	44	2
99-Sonder	8	490	36	52	44	2
15-228	10	490	36	56	46	2

Table A.1.2: Torsion spring constants for the different tines.

Tine	Torsion spring constant [Nm]
15-129	68
15-002	91
15-054	91
15-099	152
99-Sonder	152
228	354

A.2 Technical drawings of the adapter

This section introduces the technical drawings of the different parts of the adapter. All parts were manufactured with mild steel.

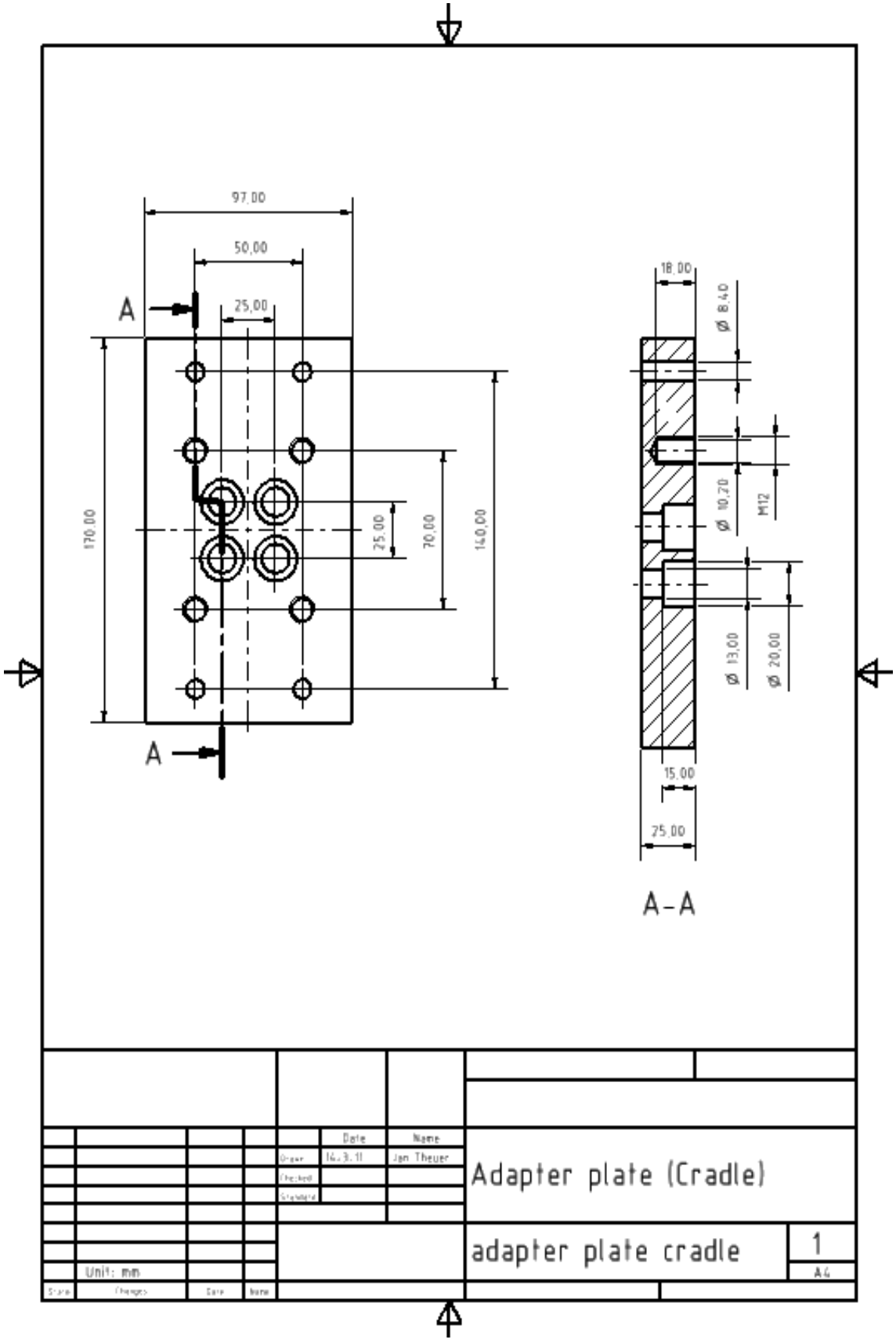

Figure A.2.1: Technical drawing of the adapter plate

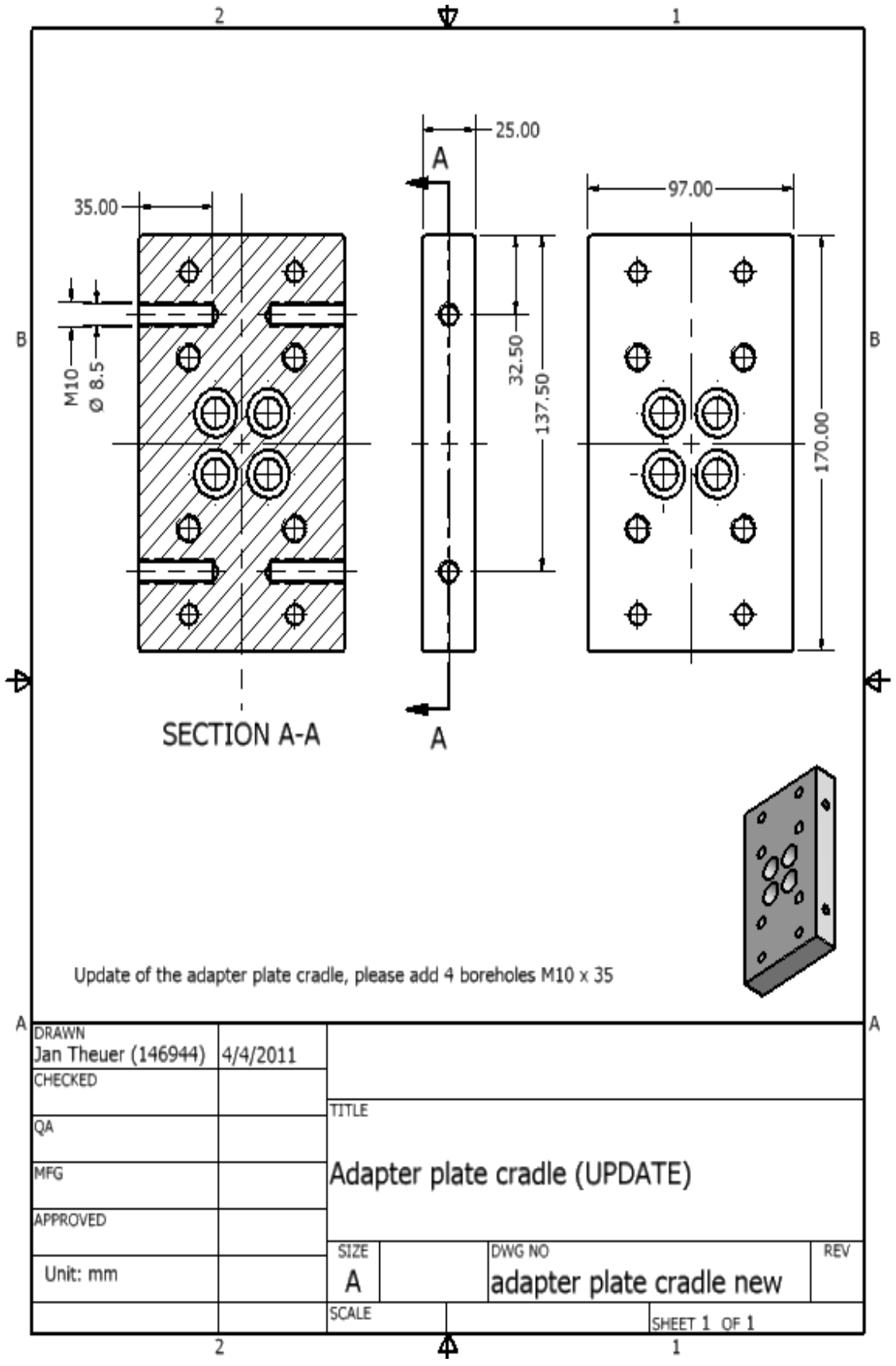

Figure A.2.2: Technical drawing of the adapter plate (update)

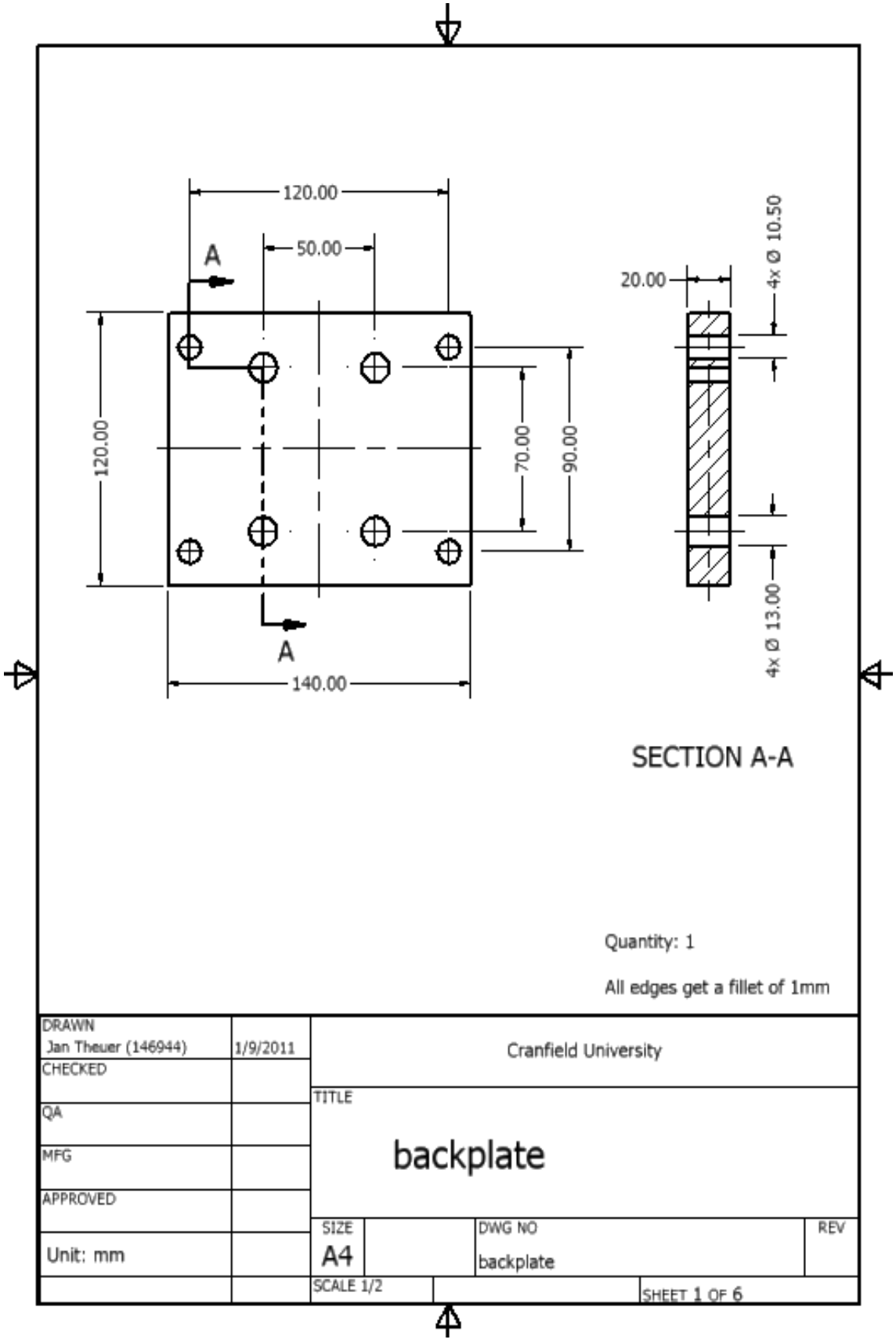

Figure A.2.3: Technical drawing of the backplate

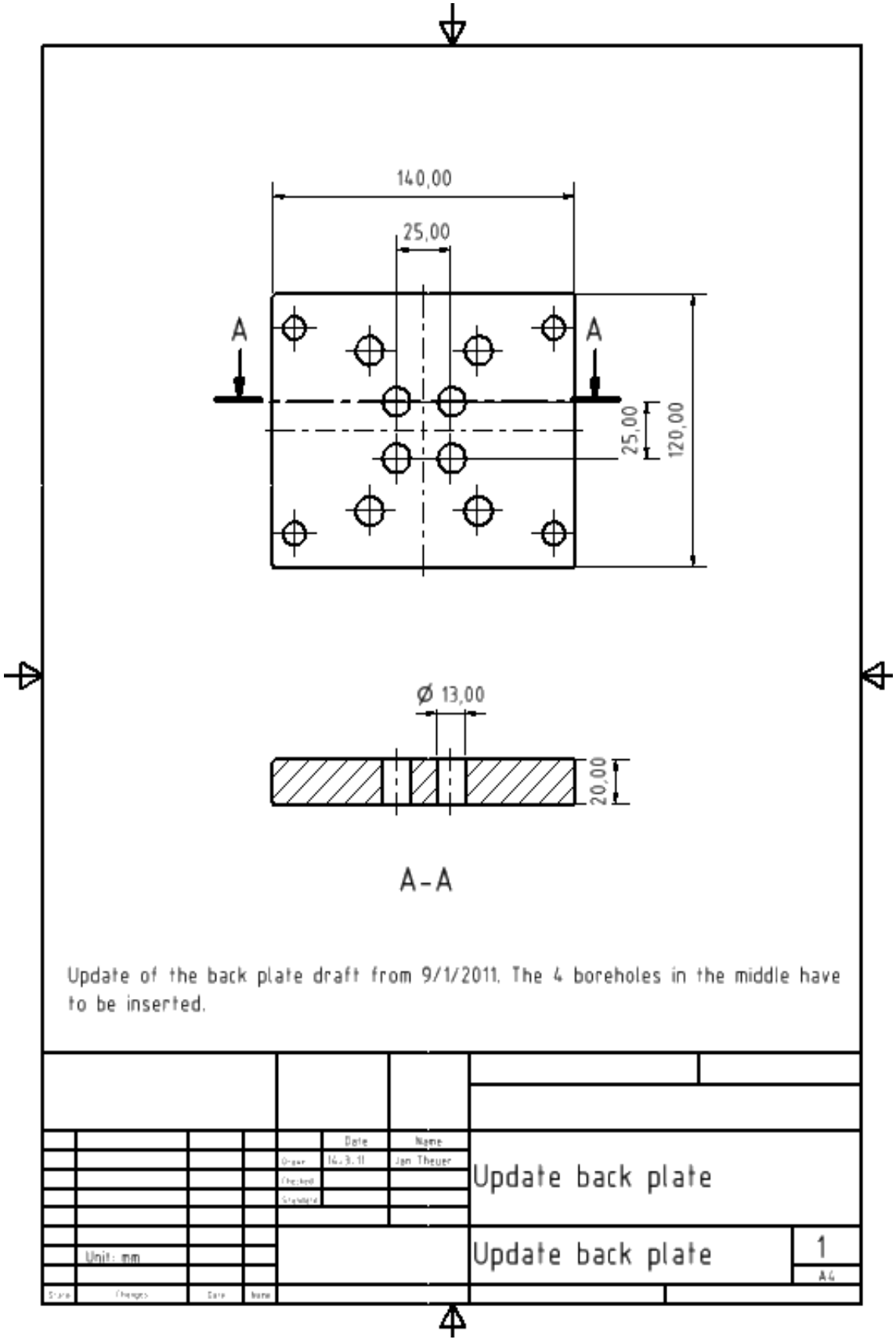

Figure A.2.4: Technical drawing of the backplate (update)

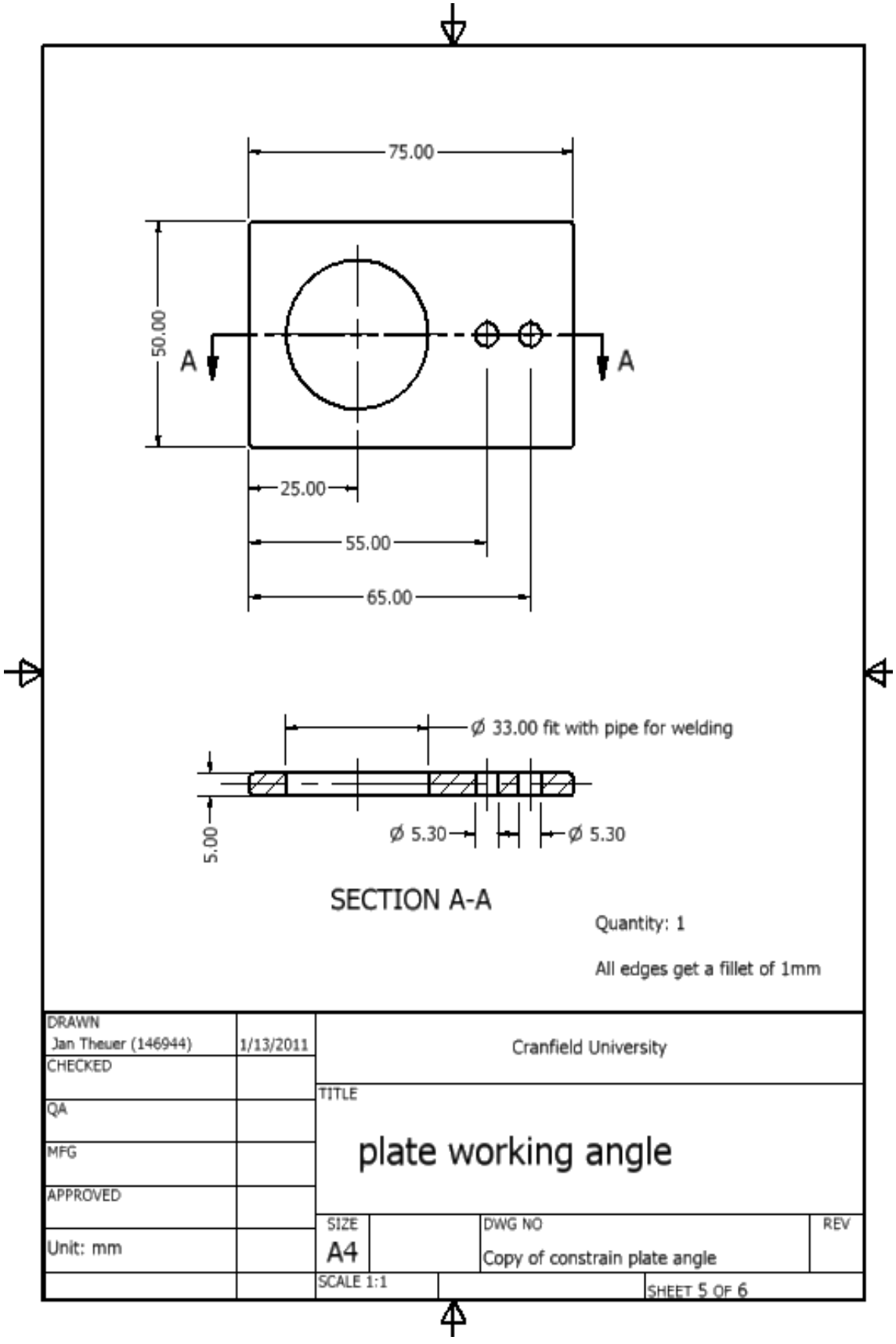

Figure A.2.5: Technical drawing of the plate working angle

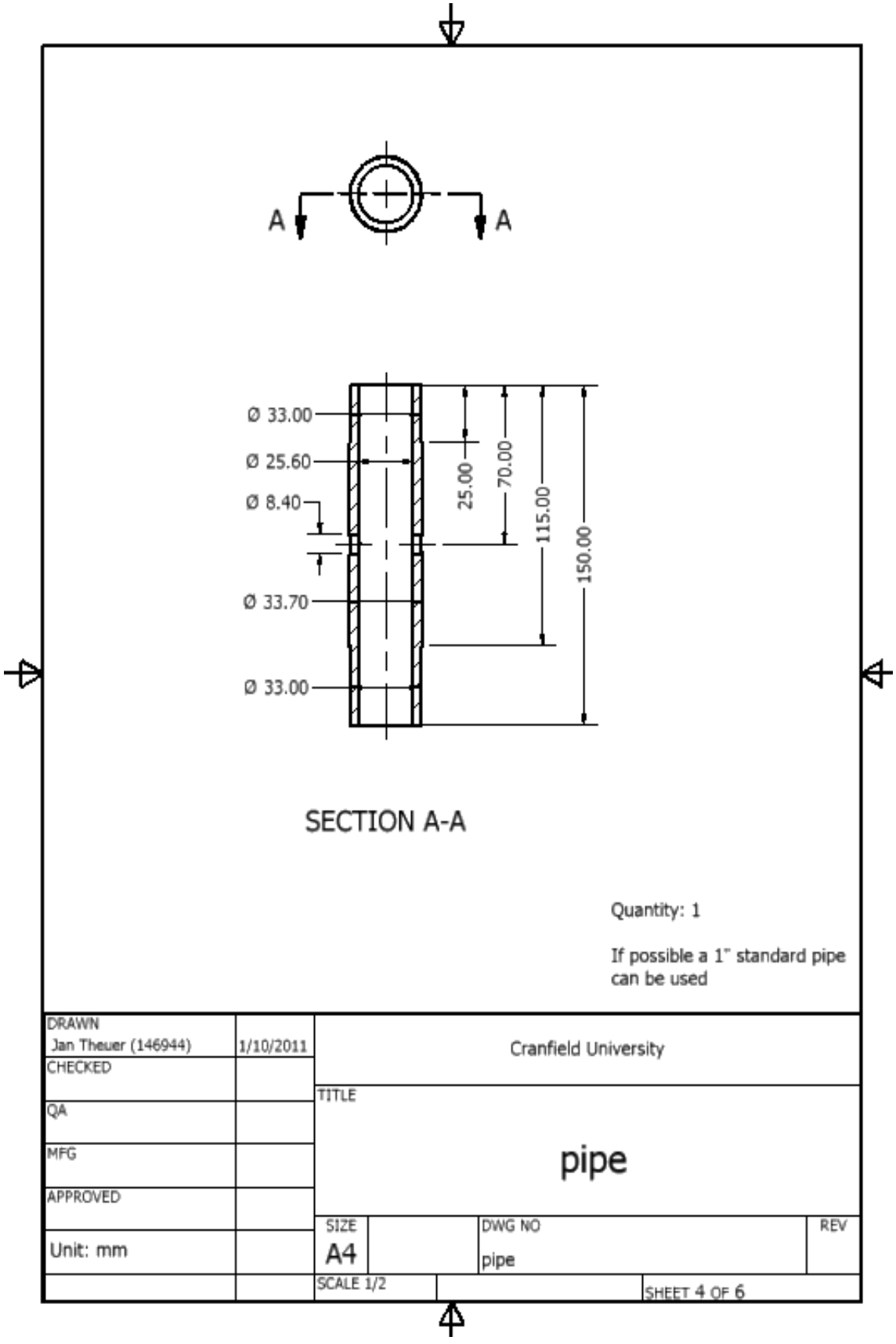

Figure A.2.6: Technical drawing of the pipe/ axis

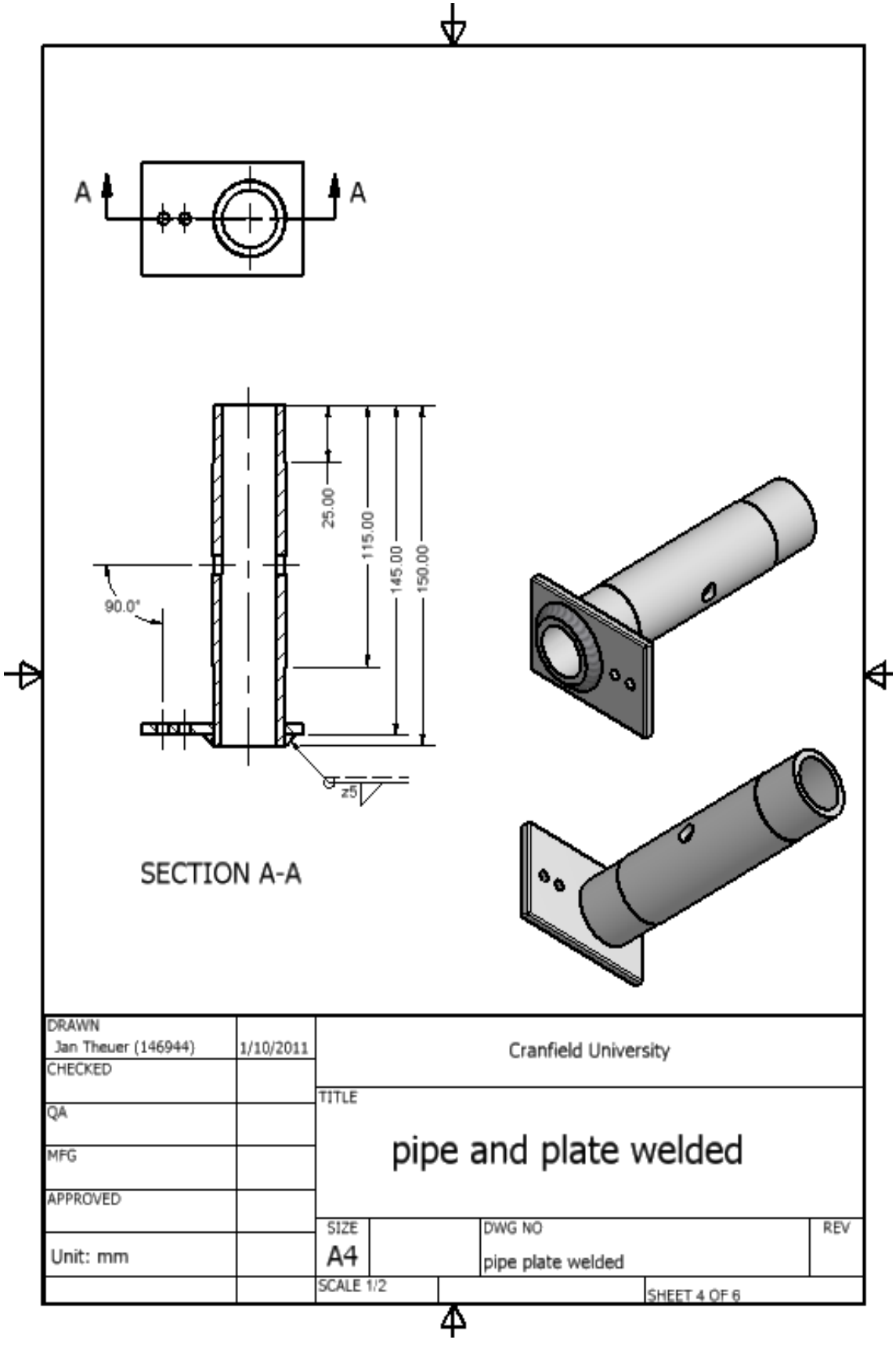

Figure A.2.7: Technical drawing of the pipe and plate working angle welded

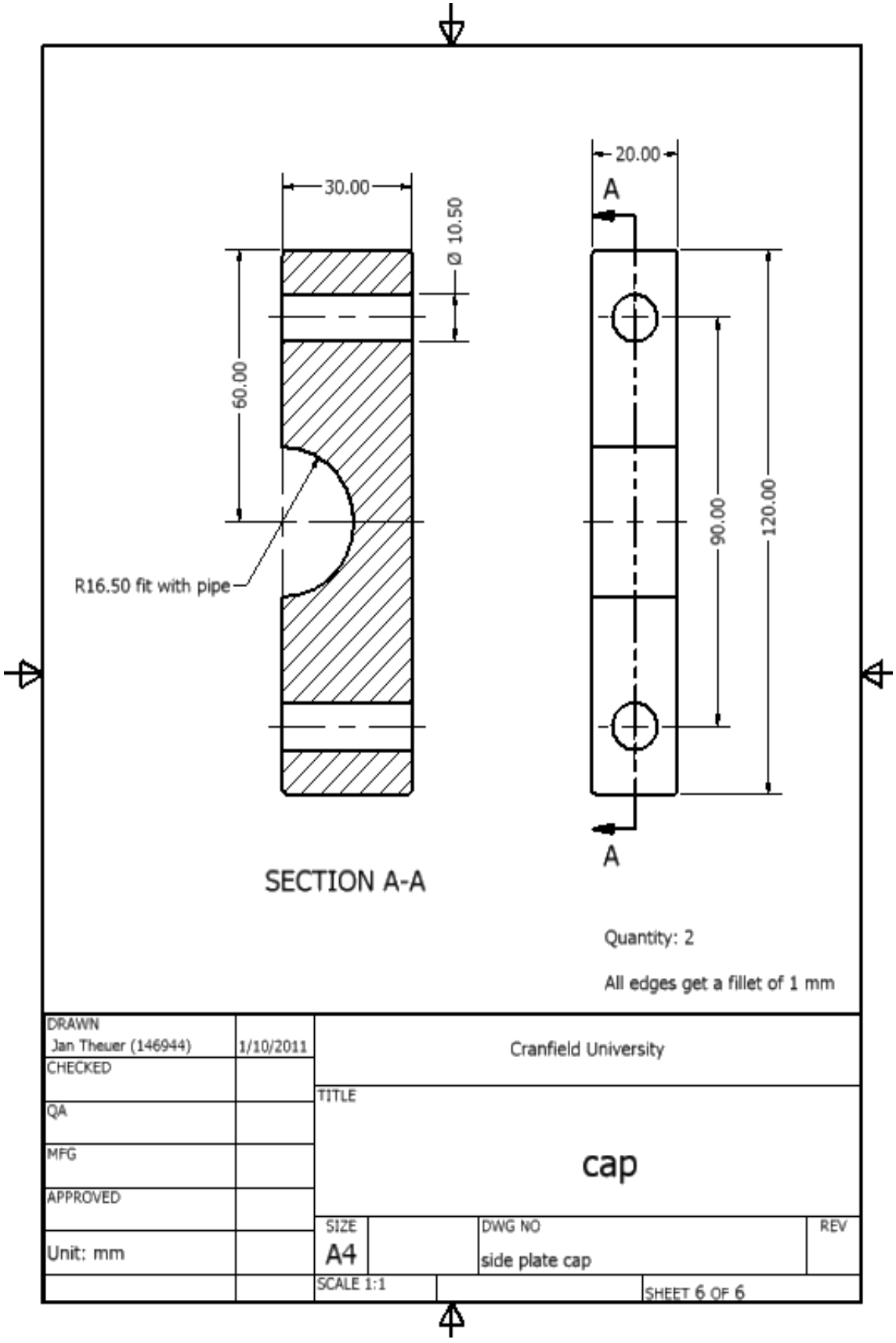

Figure A.2.8: Technical drawing of the cap

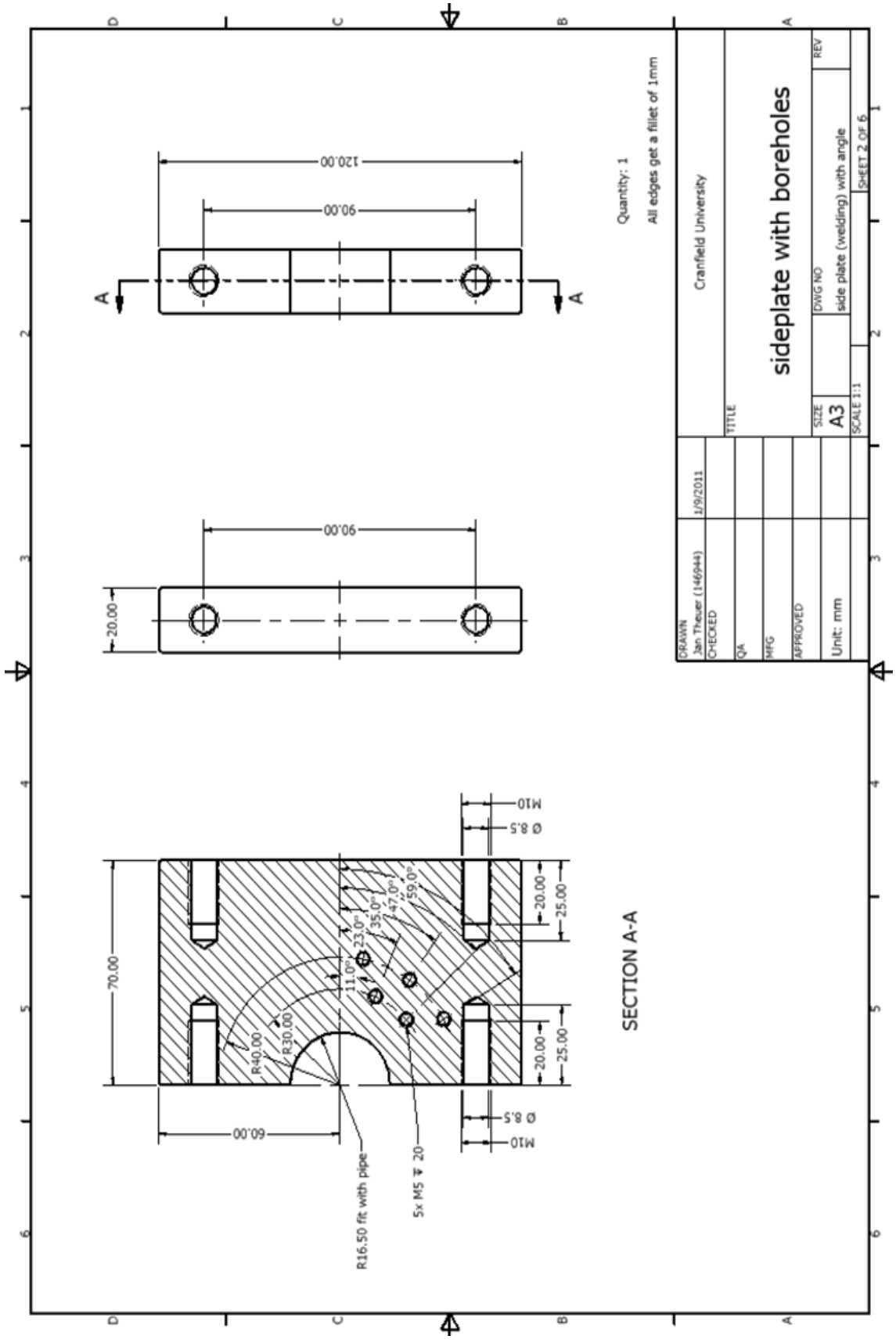

Figure A.2.9: Technical drawing of the side plate with boreholes

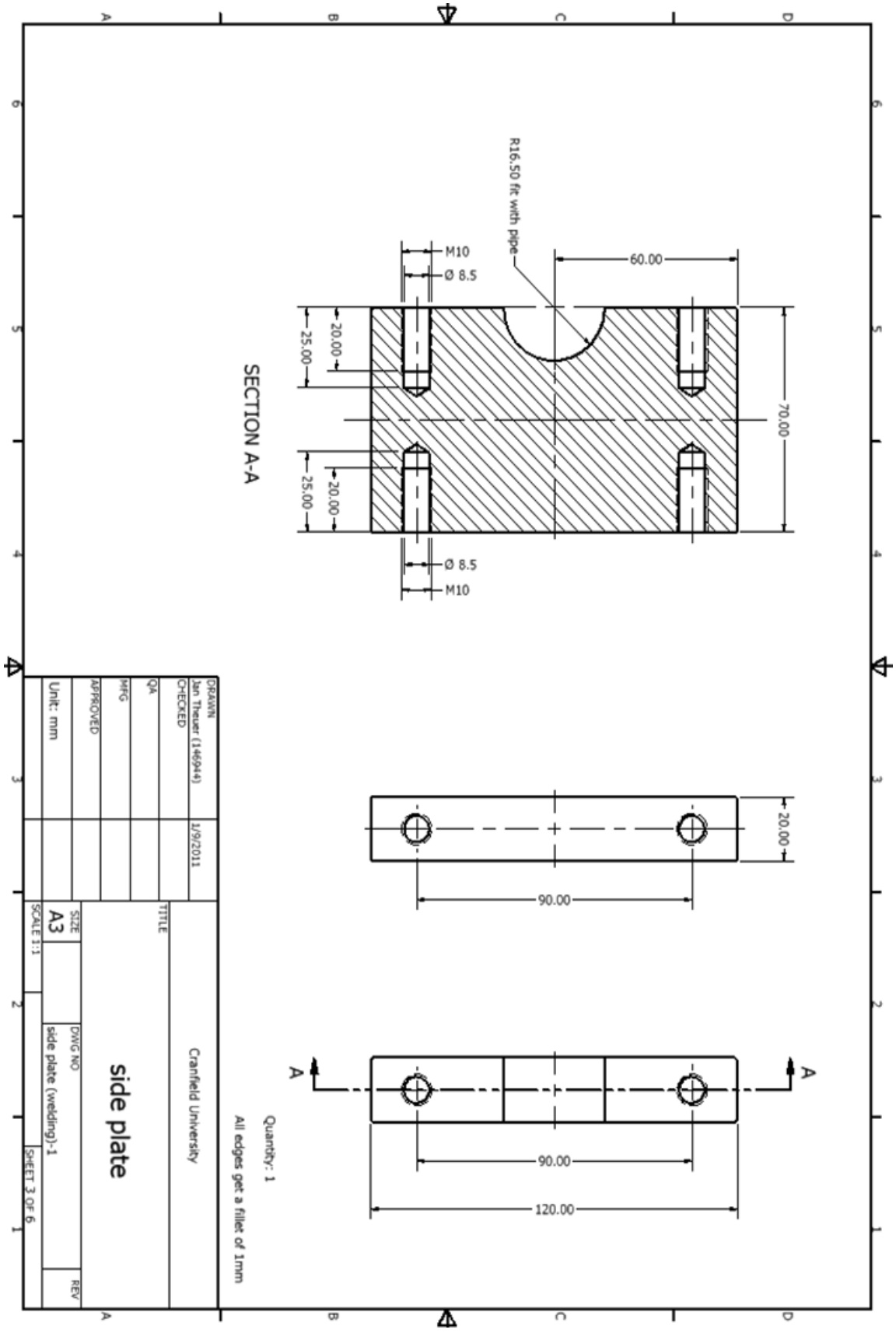

Figure A.2.10: Technical drawing of the side plate

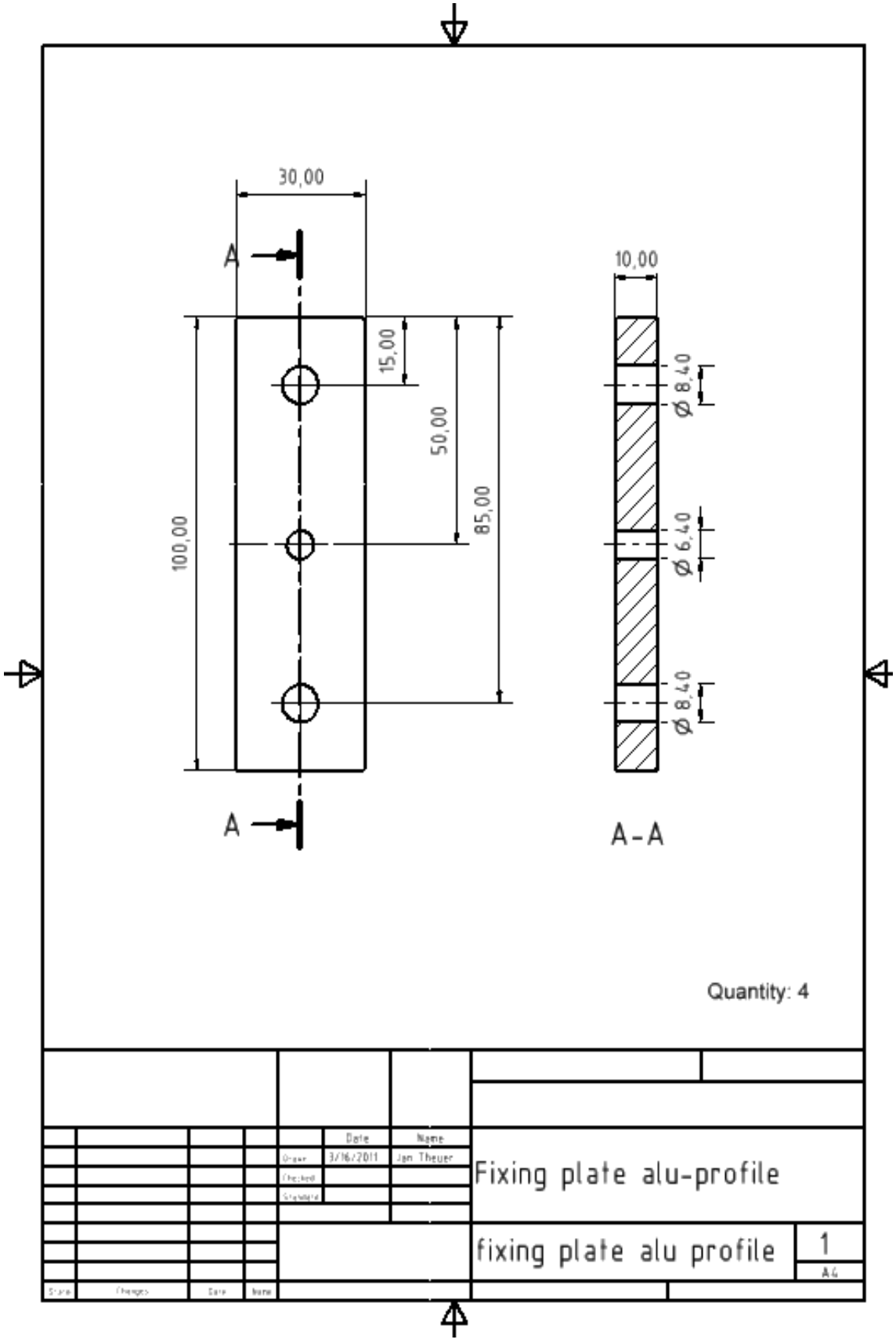

Figure A.2.11: Technical drawing of the fixing plate

A.3 Calibration for the different sensors

The calibration data was needed to transfer sensors output in voltage into equivalent physical units. In the next sections, different calibrations carried out for sensors adopted in this project are summarized.

A.3.1 Calibration data for the draught and vertical force

The calibration of the Extended Octagonal Ring Transducer[30] (EORT) was done on a frame. For the draught calibration the EORT was loaded in horizontal direction on the top flange. For the vertical force calibration, an angle was mounted to load the EORT in vertical direction. In the test setup arrangement, the draught was of positive values in travel direction and the vertical force was positive values in downward direction into the soil.

Table A.3.1: Calibration data draught

Weight [Kg]	Force [N]	Voltage [V]	Voltage [V]	Average voltage [V]
0.00	0.00	-0.0004	-0.0004	-0.0004
5.00	49.05	0.0127	0.0126	0.0127
10.13	99.40	0.0267	0.0266	0.0267
15.13	148.45	0.0400	0.0399	0.0400
20.00	196.19	0.0521	0.0520	0.0521
25.00	245.24	0.0654	0.0653	0.0654
30.13	295.59	0.0784	0.0787	0.0786

[30] It is possible to measure the resulting moment of the two force components with the EORT [10] but this function was not used in this work.

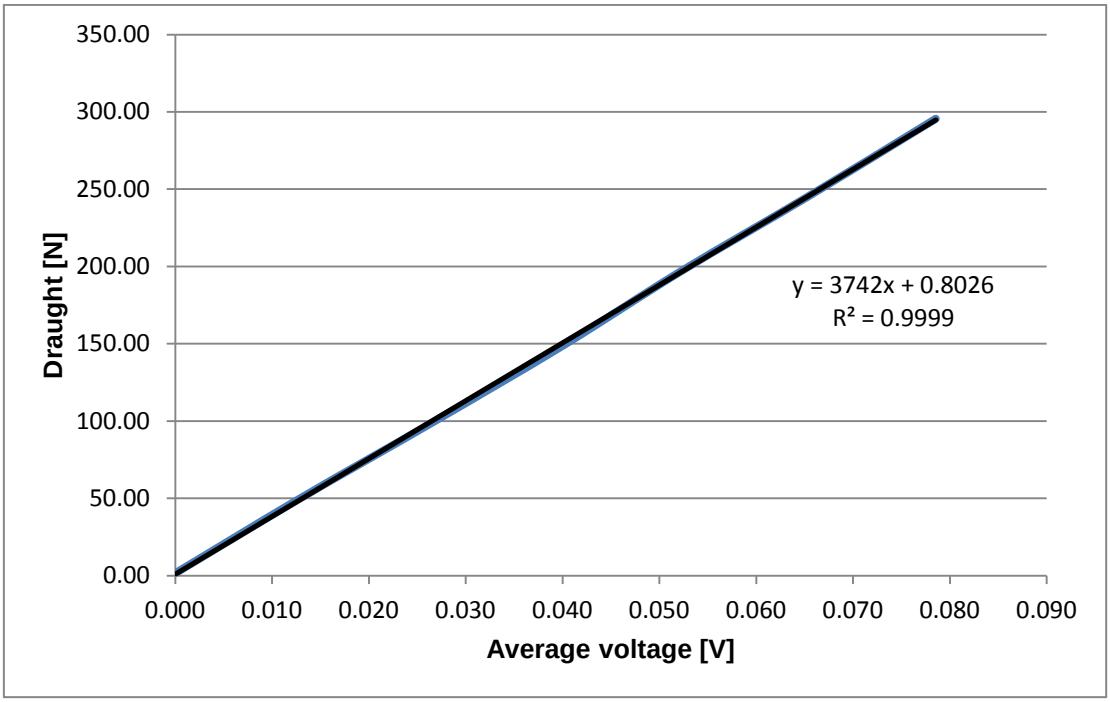

Figure A.3.1: Calibration lineare line for draught

Table A.3.2: Calibration data for the vertical force

Weight [g]	Weight [Kg]	Force [N]	Voltage [V]	Voltage [V]	Average voltage [V]
0.00	0.00	0.00	0.0002	-0.0001	0.0001
1115.50	1.12	10.94	-0.0029	-0.0031	-0.0030
6615.68	6.62	64.90	-0.0180	-0.0181	-0.0181
11748.50	11.75	115.25	-0.0321	-0.0322	-0.0322
16748.28	16.75	164.30	-0.0458	-0.0459	-0.0459
21614.90	21.61	212.04	-0.0591	-0.0592	-0.0592
26614.68	26.61	261.09	-0.0725	-0.0726	-0.0726
31747.50	31.75	311.44	-0.0866	-0.0866	-0.0866

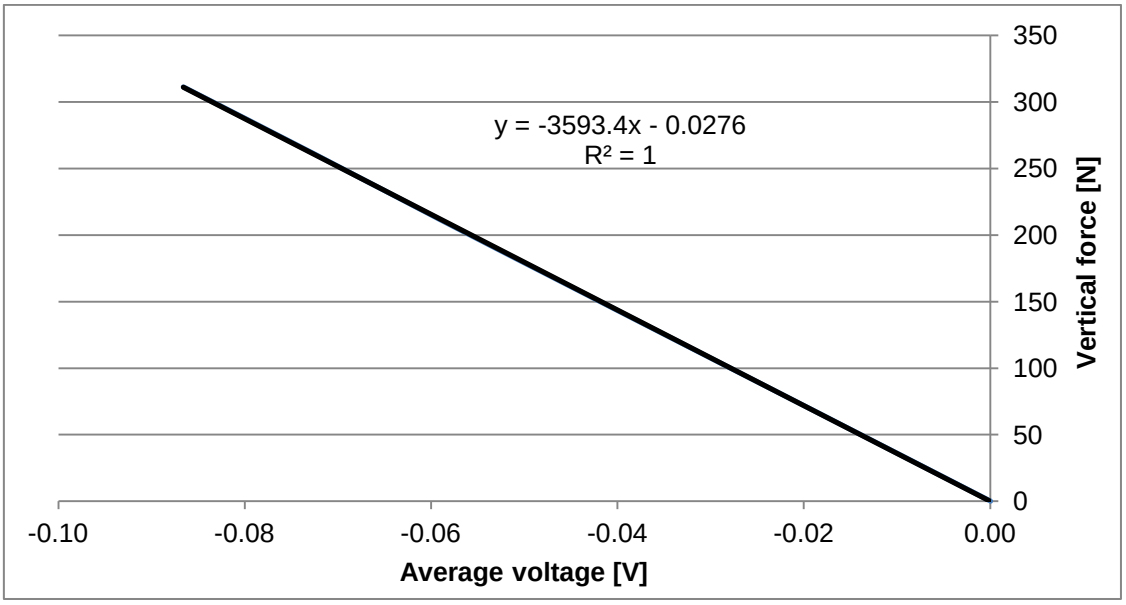

Figure A.3.2: Calibration linear line for the vertical force

A.3.2 Calibration data for both string potentiometer

The string potentiometers were calibrated on an x-table (table which is movable in one direction) with a dial indicator. The wire of the fixed string potentiometer was linked with the table. The table were displaced in x-direction and this displacement was measured with the dial indicator. The respective voltage value for each displacement could be seen on the laptop screen in DasyLab.

Table A.3.3: Calibration data for string potentiometer of the upward movement

Distance [mm]	Voltage [V]	Voltage [V]	Average voltage [V]
0	0.000	0.001	0.001
10	0.084	0.088	0.086
20	0.165	0.169	0.167
30	0.250	0.251	0.251
40	0.331	0.334	0.333
50	0.413	0.418	0.416

60	0.495	0.500	0.498
70	0.580	0.584	0.582
80	0.658	0.667	0.663
90	0.741	0.747	0.744
100	0.821	0.827	0.824
110	0.905	0.912	0.909
120	0.988	0.993	0.991
130	1.067	1.078	1.073
140	1.152	1.161	1.157
150	1.234	1.242	1.238
160	1.316	1.323	1.320
170	1.397	1.404	1.401
180	1.480	1.485	1.483
190	1.563	1.569	1.566
200	1.648	1.652	1.650
210	1.728	1.733	1.731
220	1.812	1.816	1.814
230	1.894	1.898	1.896
240	1.977	1.979	1.978
250	2.058	2.061	2.060
260	2.139	2.144	2.142
270	2.225	2.225	2.225
280	2.308	2.308	2.308
290	2.388	2.390	2.389
300	2.476	2.475	2.476

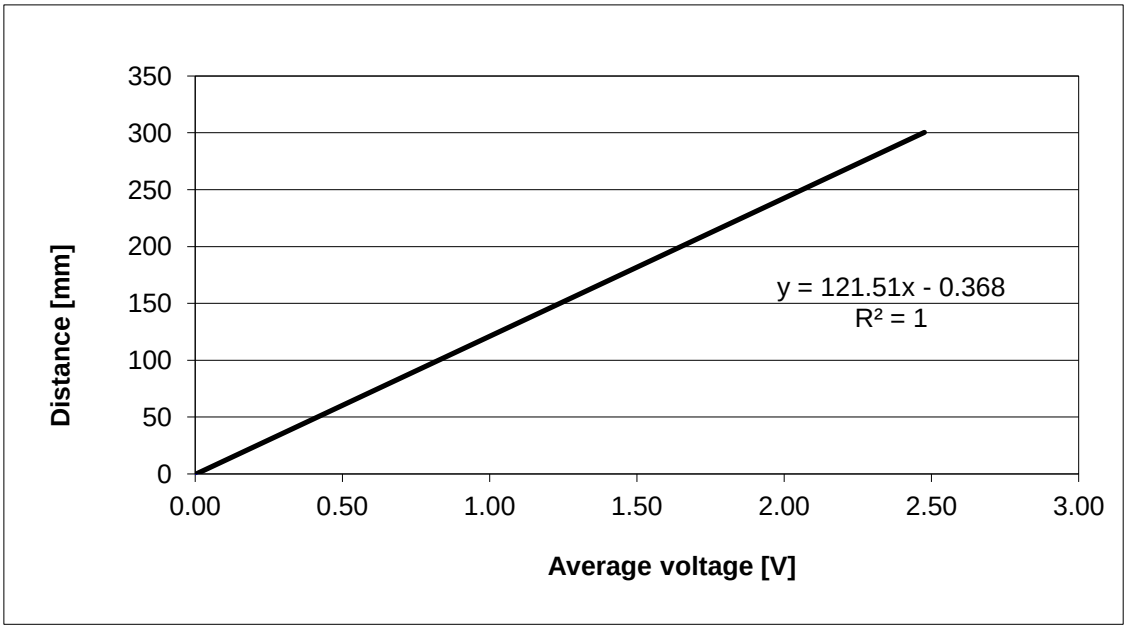

Figure A.3.3: Calibration linear line for the string potentiometer of the upward movement

Table A.3.4: Calibration data for the string potentiometer of the sideward movement

Distance [mm]	Voltage [V]	Voltage [V]	Average voltage [V]
0	0.041	0.041	0.041
10	0.127	0.125	0.126
20	0.209	0.209	0.209
30	0.291	0.293	0.292
40	0.374	0.374	0.374
50	0.458	0.456	0.457
60	0.537	0.539	0.538
70	0.620	0.620	0.620
80	0.701	0.701	0.701
90	0.785	0.783	0.784
100	0.866	0.866	0.866
110	0.948	0.949	0.949

120	1.033	1.030	1.032
130	1.113	1.112	1.113
140	1.197	1.197	1.197
150	1.278	1.279	1.279
160	1.359	1.358	1.359
170	1.440	1.438	1.439
180	1.522	1.523	1.523
190	1.609	1.606	1.608
200	1.692	1.689	1.691
210	1.775	1.772	1.774
220	1.857	1.854	1.856
230	1.938	1.939	1.939
240	2.018	2.018	2.018
250	2.101	2.102	2.102
260	2.185	2.186	2.186
270	2.270	2.272	2.271
280	2.354	2.354	2.354
290	2.437	2.437	2.437
300	2.521	2.521	2.521

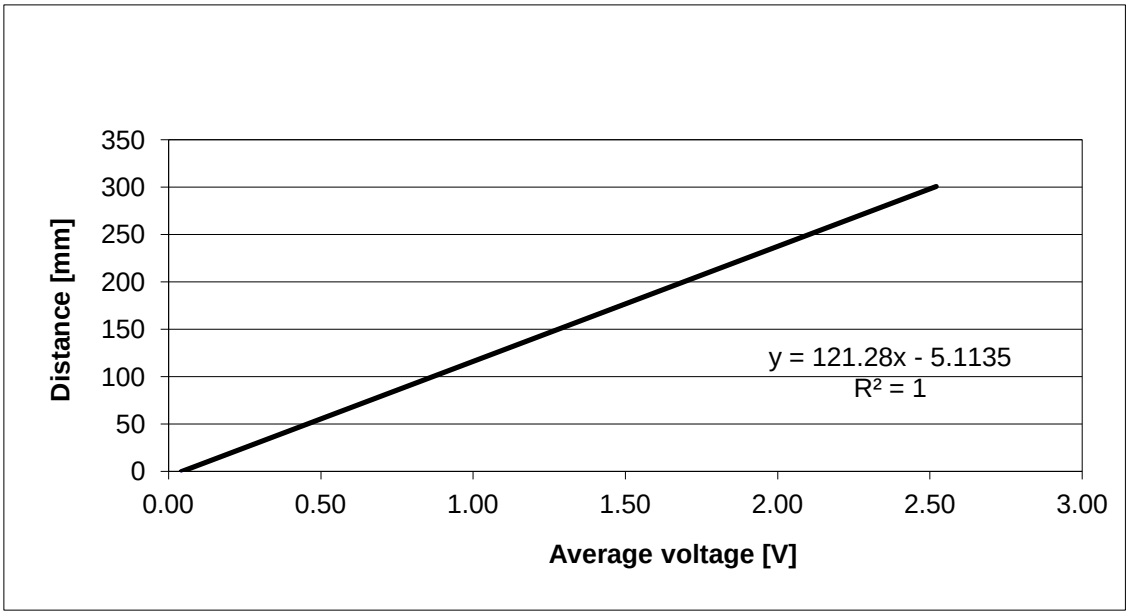

Figure A.3.4: Calibration linear line for the string potentiometer of the sideward movement

A.4 Hydrostatic compression data for the soil material model

The hydrostatic compression test obtained from the triaxial compression apparatus was investigated to obtain the material behaviour for the Drucker-Prager soil material model. Table A.4.1 summarizes the measured data from this test. These data points were inserted in Abaqus to model the hardening behaviour of the soil.

Table A.4.1: Hydrostatic compression test data obtained from triaxial compression apparatus needed for soil cap hardening behaviour in the Drucker-Prager material model

Hydrostatic compression soil data		
	Soil I (BD: 1450 Kg m^{-3})	**Soil II (BD: 1600 Kg m^{-3})**
Yield stress [Pa]	**Volumetric plastic strain [-]**	**Volumetric plastic strain [-]**
9000	0	0

20000	0.02738585	0.017561925
30000	0.04792255	0.031333699
40000	0.067459295	0.046037331
50000	0.085160999	0.059343177
60000	0.10120866	0.072114998
70000	0.11574921	0.083637771
80000	0.12906939	0.094542292
90000	0.12906939	0.10577655
100000	0.14096491	0.11636926
110000	0.15287655	0.12512513
120000	0.17304051	0.13406021
130000	0.18255262	0.14317628
140000	0.1935575	0.15067594
150000	0.20108941	0.15824728
170000	0.21502785	0.17316239
190000	0.22744843	0.18426402
210000	0.23846406	0.19482805
230000	0.24857829	0.20497813
250000	0.25757251	0.2142519
270000	0.26629971	0.22224257
290000	0.27407534	0.23077265
310000	0.28127752	0.23807519

A.5 Summary of the experimental and simulation data

The following tables compare between experimental and FEM simulated draught and upward movement with error values. The data represent the maximum values before the first crack occurred in the soil.

Table A.5.1: Comparison between experimental and simulated data for tine 15-129 at 56°

	Draught [N]			Upward movement [mm]		
Attempt	**Experiment**	**Simulation**	**Error**	**Experiment**	**Simulation**	**Error**
1450_20_1	5.25	8.25		7.36	7.36	
1450_20_2	6.06	7.03		7.36	7.36	
1450_20_3	5.97	6.80		5.09	4.77	
Mean 1450_20	6.02	6.92	0.13	6.60	6.50	0.02
1450_30_1	6.78	12.33		9.56	8.80	
1450_30_2	7.06	14.64		11.63	8.51	
1450_30_3	9.21	13.08		11.95	7.84	
Mean 1450_30	8.00	12.71	0.37	10.60	8.66	0.18
1600_20_1	7.37	7.37		6.04	6.04	
1600_20_2	5.61	6.74		6.10	6.10	
1600_20_3	7.17	6.62		4.84	4.84	
Mean 1600_20	6.72	6.91	0.03	5.66	5.66	0.00
1600_30_1	6.93	6.93		7.11	6.62	
1600_30_2	5.37	6.67		8.01	7.95	
1600_30_3	6.87	6.51		7.98	9.65	
Mean 1600_30	6.39	6.70	0.05	7.70	8.07	0.05

Table A.5.2: Comparison between experimental and simulated data for tine 15-129 at 80°

	Draught [N]			Upward movement [mm]		
Attempt	**Experiment**	**Simulation**	**Error**	**Experiment**	**Simulation**	**Error**
1450_20_1	5.21	5.52		8.84	9.38	
1450_20_2	3.77	3.77		8.10	9.77	
1450_20_3	6.75	6.75		9.38	9.77	
Mean 1450_20	5.24	5.35	0.02	8.77	9.64	0.09
1450_30_1	2.98	11.38		12.49	13.71	
1450_30_2	4.11	3.95		14.56	17.23	
1450_30_3	4.54	8.33		17.22	18.04	
Mean 1450_30	4.33	6.14	0.30	14.86	15.88	0.06
1600_20_1	5.65	5.78		10.46	10.46	
1600_20_2	1.45	2.01		12.73	16.29	
1600_20_3	8.17	4.64		13.90	14.84	
Mean 1600_20	5.09	4.14	0.19	12.18	12.65	0.04
1600_30_1	3.60	2.20		13.77	20.31	
1600_30_2	4.85	5.83		18.82	20.45	
1600_30_3	7.46	10.90		21.89	21.89	
Mean 1600_30	4.23	4.02	0.05	20.36	21.17	0.04

Table A.5.3: Comparison between experimental and simulated data for tine 15-129 at 104°

	Draught [N]			Upward movement [mm]		
Attempt	**Experiment**	**Simulation**	**Error**	**Experiment**	**Simulation**	**Error**
1450_20_1	4.87	4.85		10.70	8.73	
1450_20_2	2.77	4.14		10.16	10.16	
1450_20_3	4.14	5.17		9.54	11.89	
Mean 1450_20	4.51	5.01	0.10	10.13	10.26	0.01
1450_30_1	5.54	5.74		16.98	16.98	
1450_30_2	6.86	6.57		16.93	16.58	
1450_30_3	not used	not used		17.99	17.99	
Mean 1450_30	6.20	6.16	0.01	17.30	17.18	0.01
1600_20_1	2.10	2.81		11.96	16.00	
1600_20_2	6.70	7.51		12.16	13.19	
1600_20_3	4.42	5.02		12.69	13.99	
Mean 1600_20	4.41	5.11	0.14	12.43	13.59	0.09
1600_30_1	12.77	13.05		21.03	21.03	
1600_30_2	8.20	10.07		22.88	22.88	
1600_30_3	8.68	8.99		24.90	24.41	
Mean 1600_30	10.73	11.02	0.03	22.94	22.77	0.01

Table A.5.4: Comparison between experimental and simulated data for tine 15-228 at 56°

	Draught [N]			Upward movement [mm]		
Attempt	**Experiment**	**Simulation**	**Error**	**Experiment**	**Simulation**	**Error**
1450_20_1	10.79	19.94		3.43	3.43	
1450_20_2	10.81	10.81		3.42	3.71	
1450_20_3	7.62	9.63		3.92	3.92	
Mean 1450_20	9.22	10.22	0.10	3.59	3.69	0.03
1450_30_1	16.19	20.12		5.54	5.54	
1450_30_2	23.84	25.25		6.50	6.34	
1450_30_3	17.22	30.90		3.98	3.81	
Mean 1450_30	20.02	22.69	0.12	5.34	5.23	0.02
1600_20_1	16.27	17.83		6.00	5.85	
1600_20_2	13.13	13.13		5.47	5.47	
1600_20_3	16.01	22.54		6.08	6.08	
Mean 1600_20	14.70	15.48	0.05	5.85	5.80	0.01
1600_30_1	20.20	22.68		7.55	8.02	
1600_30_2	23.43	27.04		8.99	8.62	
1600_30_3	not used	not used		8.37	8.61	
Mean 1600_30	21.82	24.86	0.12	8.30	8.42	0.01

Table A.5.5: Comparison between experimental and simulated data for tine 15-228 at 80°

	Draught [N]			Upward movement [mm]		
Attempt	**Experiment**	**Simulation**	**Error**	**Experiment**	**Simulation**	**Error**
1450_20_1	6.65	21.64		4.41	4.41	
1450_20_2	7.21	13.88		4.72	5.90	
1450_20_3	9.77	14.94		4.94	5.62	
Mean 1450_20	8.49	14.41	0.41	4.69	5.31	0.12
1450_30_1	6.26	21.56		4.99	6.78	
1450_30_2	7.87	22.41		7.81	7.81	
1450_30_3	8.58	18.85		8.49	7.52	
Mean 1450_30	7.57	20.94	0.64	8.15	7.37	0.10
1600_20_1	6.35	18.14		6.58	9.96	
1600_20_2	9.72	12.27		7.00	10.77	
1600_20_3	9.27	10.47		6.67	8.31	
Mean 1600_20	9.50	11.37	0.16	6.75	9.68	0.30
1600_30_1	not used	not used		6.20	11.44	
1600_30_2	6.20	8.70		7.37	7.37	
1600_30_3	7.31	7.79		6.61	7.41	
Mean 1600_30	6.76	8.25	0.18	6.99	7.39	0.05

Table A.5.6: Comparison between experimental and simulated data for tine 15-228 at 104°

	Draught [N]			Upward movement [mm]		
Attempt	**Experiment**	**Simulation**	**Error**	**Experiment**	**Simulation**	**Error**
1450_20_1	6.04	12.37		7.60	7.60	
1450_20_2	6.52	7.08		4.27	5.12	
1450_20_3	5.17	5.17		5.73	6.16	
Mean 1450_20	5.85	6.13	0.05	5.87	6.29	0.07
1450_30_1	2.95	4.57		11.23	12.36	
1450_30_2	5.95	5.95		11.04	11.30	
1450_30_3	8.23	8.23		12.36	12.36	
Mean 1450_30	5.71	6.25	0.09	11.54	12.01	0.04
1600_20_1	2.77	11.15		6.93	9.56	
1600_20_2	7.33	7.07		8.27	9.71	
1600_20_3	10.40	8.91		7.76	9.69	
Mean 1600_20	8.87	7.99	0.10	8.02	9.70	0.17
1600_30_1	9.17	11.15		12.60	12.60	
1600_30_2	8.48	8.48		13.96	16.91	
1600_30_3	9.37	11.30		14.68	16.29	
Mean 1600_30	9.01	10.31	0.13	13.64	14.45	0.06

Table A.5.7: Comparison between experimental and simulated data for tine 15-054 at 56°

	Draught [N]			Upward movement [mm]		
Attempt	**Experiment**	**Simulation**	**Error**	**Experiment**	**Simulation**	**Error**
1450_20_1	4.39	3.11		8.04	8.04	
1450_20_2	6.33	9.49		7.64	9.40	
1450_20_3	8.82	2.35		9.68	9.98	
Mean 1450_20	6.51	4.98	0.23	8.45	9.14	0.08
1450_30_1	10.11	8.97		13.62	10.82	
1450_30_2	8.45	5.60		12.24	11.05	
1450_30_3	4.43	4.11		12.07	11.04	
Mean 1450_30	7.66	6.23	0.19	12.64	10.97	0.13
1600_20_1	4.52	4.99		9.29	9.29	
1600_20_2	6.64	8.01		13.34	11.68	
1600_20_3	4.47	5.37		13.24	11.72	
Mean 1600_20	5.21	6.12	0.15	11.96	10.90	0.09
1600_30_1	3.81	4.12		14.45	12.05	
1600_30_2	3.36	2.94		13.67	12.03	
1600_30_3	5.16	7.37		13.51	12.04	
Mean 1600_30	4.11	4.81	0.15	13.88	12.04	0.13

Table A.5.8: Comparison between experimental and simulated data for tine 15-054 at 80°

	Draught [N]			Upward movement [mm]		
Attempt	**Experiment**	**Simulation**	**Error**	**Experiment**	**Simulation**	**Error**
1450_20_1	4.46	3.88		9.29	11.01	
1450_20_2	3.98	3.61		10.03	11.01	
1450_20_3	5.82	7.90		7.44	8.43	
Mean 1450_20	4.75	5.13	0.07	8.92	10.15	0.12
1450_30_1	5.72	9.38		13.73	14.57	
1450_30_2	4.16	4.16		14.42	14.42	
1450_30_3	5.23	5.81		16.30	16.30	
Mean 1450_30	5.04	4.99	0.01	14.82	15.10	0.02
1600_20_1	7.30	7.30		13.21	14.75	
1600_20_2	8.90	7.59		13.47	13.47	
1600_20_3	5.03	6.61		16.80	16.80	
Mean 1600_20	7.08	7.17	0.01	14.49	15.01	0.03
1600_30_1	3.82	2.84		23.03	23.94	
1600_30_2	4.49	5.02		23.50	23.94	
1600_30_3	7.62	8.04		23.47	23.94	
Mean 1600_30	5.31	5.30	0.00	23.33	23.94	0.03

Table A.5.9: Comparison between experimental and simulated data for tine 15-054 at 104°

	Draught [N]			Upward movement [mm]		
Attempt	**Experiment**	**Simulation**	**Error**	**Experiment**	**Simulation**	**Error**
1450_20_1	4.53	7.03		7.72	7.72	
1450_20_2	not used	not used		8.89	10.55	
1450_20_3	5.18	4.51		9.85	9.85	
Mean 1450_20	4.85	5.77	0.16	8.82	9.37	0.06
1450_30_1	6.89	5.69		15.20	15.63	
1450_30_2	6.55	8.71		12.27	11.17	
1450_30_3	7.24	9.23		10.11	10.11	
Mean 1450_30	6.89	7.88	0.12	12.53	12.30	0.02
1600_20_1	5.99	6.94		7.11	8.77	
1600_20_2	5.70	7.92		7.00	8.77	
1600_20_3	6.42	6.94		9.06	9.06	
Mean 1600_20	6.04	7.27	0.17	7.72	8.87	0.13
1600_30_1	6.67	7.23		19.47	18.88	
1600_30_2	8.17	9.63		16.83	18.70	
1600_30_3	11.46	10.69		20.25	22.77	
Mean 1600_30	8.77	9.18	0.05	18.85	20.12	0.06